Department of Chemical Engineering

Fundamental Study of Simple Gas Adsorption and Adsorption-Induced Deformation in Carbonaceous Materials

Rui Diao

This thesis is presented for the Degree of
Doctor of Philosophy
of
Curtin University

June 2017

Declaration by Author

To the best of my knowledge and belief this thesis contains no material previously published by any other person except where due acknowledgment has been made.

This thesis contains no material which has been accepted for the award of any other degree or diploma in any university.

Signature: Rui Diao .....

Date: 09/06/2017 .....

Abstract

Adsorption is widely used in industries for gas separation, purification, catalysis and energy storage. Due to the introduction of adsorbents, the adsorbate can exhibit different phase behaviours compared to its bulk phase. At the same time, the adsorbate can induce adsorbent deformation due to the forces exerted by adsorbate molecules on the surface of the adsorbent. The understanding of the abundant adsorption and phase behaviours during gas adsorption on solid surfaces and in porous solids as well as the adsorption-induced solid deformation is not only of fundamental scientific interests, but also important for the application and optimization of industrial adsorption processes.

Molecular simulations, particularly Monte Carlo simulations, have shown great potential for adsorption studies. With molecular simulation, the microscopic mechanisms of the adsorption phenomena can be obtained, which are hardly accessible to experimental studies. In this thesis, we report Monte Carlo simulation studies of simple gas adsorption on graphite surfaces and in graphitic slit porous solids, with the aim of providing fundamental understanding of gas adsorption and adsorption-induced deformation in carbonaceous solids.

We first studied the adsorption and desorption of krypton on graphite at temperatures in the range of 60-88 K, with a particular emphasis on the gas-solid, gas-liquid and liquid-solid two-dimensional (*2D*) phase transitions. We find that for temperatures below the bulk triple point, the transition from a *2D* liquid-like monolayer to a *2D* solid-like state is manifested as a sub-step in the isotherm. A further increase in the chemical potential leads to another rearrangement of the *2D* solid-like state from a disordered structure to an ordered structure that is signalled by another sub-step in the monolayer region and a spike in the plot of isosteric heat versus density at loadings close to the dense monolayer coverage concentration. Whenever a *2D* transition occurs in a grand canonical isotherm it is always associated with a hysteresis, a feature that is not widely recognised in the literature. We studied in details this hysteresis with the analysis of the equilibrium transition obtained with the Mid-Density Scheme and found that the equilibrium transition coincides exactly with the vertical segment of the Canonical kinetic Monte Carlo isotherm, indicating the

co-existence of two-phases at equilibrium. The *2D* co-existence is also observed for higher layers, provided that the temperature is well below the triple point.

We further investigated the adsorption of argon in homogeneous graphitic slit pores with two open ends in the micropore range, particularly looking into the order-disorder transitions and the restructuring hysteresis loops. The formation of solid-like phases in the pore is observed at temperatures above the triple point and this is affected significantly by the pore width, as no ordering transition occurs when there is incommensurate molecular packing in the pore. The ordering transition is first order with a Type H1 hysteresis loop when the pore is infinitely long, while the transition is second order in finite length pores and the hysteresis is entirely resulted from the adsorbate restructuring. When the ordering transition occurs after a first order capillary condensation/evaporation, the hysteresis loop is induced by both mechanisms.

When adsorption occurs in porous solids, the adsorbate can exert forces to the pore walls and induce adsorbent deformation. In order to shed light on the underlying mechanisms of adsorption-induced deformation, we studied argon adsorption in deformable graphitic slit pores at sub- and supercritical temperatures. We find that solvation pressure is the driving force for the deformation. This is analysed by studying its spatial distribution across the pore in order to understand the effects of adsorbate location on the deformation. The pore width affects the packing of the adsorbate molecules and zero solvation pressure at saturation pressure could be used to distinguish between commensurate and incommensurate pores. Thermal fluctuation increases with temperature meaning that molecular excursions are closer to the pore walls at high temperatures, resulting in greater repulsion compared to that at lower temperatures. Consequently, the pore deformation depends on an intricate interplay between packing and thermal fluctuation.

Publications

Peer-reviewed journal papers

1. Diao, R.; Fan, C.; Do, D. D.; Nicholson, D. On the 2D-transition, hysteresis and thermodynamic equilibrium of Kr adsorption on a graphite surface. *J. Colloid Interface Sci.* **2015**, *460*, 281-289.

2. Diao, R.; Fan, C.; Do, D. D.; Nicholson, D. On the adsorbate restructuring induced hysteresis of simple gas adsorption in slit micropores. *Chem. Eng. J.* **2016**, *290*, 381-390.

3. Diao, R.; Fan, C.; Do, D. D.; Nicholson, D. Monte Carlo simulation of adsorption-induced deformation in finite graphitic slit pores. *J. Phys. Chem. C* **2016**, *120*, 29272-29282.

4. Diao, R.; Fan, C.; Do, D. D.; Nicholson, D. Adsorption induced deformation in graphitic slit mesopores: A Monte Carlo simulation study. *Chem. Eng. J.* **2017**, *328*, 280-292.

Conference abstracts

1. Fan, C.; Diao, R.; Do, D. D. On the hysteresis induced by adsorbate restructuring examples of simple gas adsorption on surface and in pores. PBAST-7, 24-27 Sep. 2015, Xiamen, China.

2. Diao, R.; Fan, C.; Do, D. D.; Nicholson, D. Monte Carlo simulation of adsorption-induced deformation in graphitic slit pores. Chemeca, 25-28 Sep. 2016, Adelaide.

Acknowledgements

I would like to express my most sincere thanks to my supervisors, Professor Vishnu Pareek and Dr. Chunyan Fan, for providing financial support to my PhD in the form of the Curtin International Postgraduate Research Scholarship (CIPRS). I sincerely appreciate Professor Vishnu Pareek for his continuous supports and guidance throughout my PhD and many thanks to him for providing me the opportunities and supports which broaden my horizons. The enormous assistance, patience and continuous supports that I received from Dr. Chunyan Fan are gratefully appreciated. Thanks to her for leading me into the fascinating world of molecular simulation and I would not have completed my PhD without the discussions and hands-on guidance from her. Her optimistic character towards life and research has been encouraging me to deal with any difficulties. Also I would like to show my deep gratitude to my co-supervisor Professor Duong D. Do in the University of Queensland for providing me with valuable guidance and suggestions. This thesis would not be completed without the enormous efforts and assistance from him. The endless enthusiasm and serious attitude about research of my supervisors have always been inspiring me to do my research with motivation and energy.

I would like to thank my thesis committee chairperson, Professor Shaomin Liu, for his assistance and advices throughout my PhD. The valuable suggestions to the publications received from Professor David Nicholson in the University of Queensland are much appreciated. The help received from Dr. Sui Boon Liaw is also acknowledged.

Thanks to the friendly staff in the Department of Chemical Engineering for their kind help in many ways. The technical support received from the friendly staff in the Pawsey Supercomputing Centre is also appreciated.

I would like to show my thanks to all my friends in Australia and China for their supports and encouragements.

Finally, special thanks to my husband for his endless love and supports. He is my life tutor and makes me a better me. I also would like to express my deep gratefulness to my parents and parents-in-law for their unconditional love, supports and patience.

Table of Contents

List of Figures

List of Tables

Nomenclature

BJH	Barrett-Joyner Halenda
CMC	Canonical Monte Carlo
C-kMC	Canonical kinetic Monte Carlo
DA	Dubinin-Astakhov
DR	Dubinin-Radushkevich
EOS	Equation of State
fcc	Face Centred Cubic
FF	Fluid-Fluid
GCMC	Grand Canonical Monte Carlo
MD	Molecular Dynamics
MDS	Mid-Density Scheme
IUPAC	International Union of Pure and Applied Chemistry
kMC	kinetic Monte Carlo
LJ	Lennard-Jones
SF	Solid-Fluid
SS	Solid-Solid

Chapter 1. Introduction

1.1. Background

Adsorption is widely present in many natural systems and also plays an important role in industrial applications such as separation, purification, catalysis and energy storage [1]. Academic interest in the adsorption phenomena is commensurate with their industrial importance and adsorption is accepted as one of the standard methods for the characterization of the surface area and pore size distributions of solid materials [2-4]. A fundamental study of the adsorption mechanisms at the molecular level is essential for designing and optimizing industrial adsorption processes as well as the solid materials used for adsorption.

In 1918, Langmuir proposed the first theoretical model in molecular scale for the adsorption process, which describes the adsorption of a fluid on a homogeneous surface up to monolayer coverage [5]. Later in 1938, Brunauer, Emmett and Teller derived the famous BET equation for multilayer adsorption, which is now commonly used for surface area determination [6]. Thereafter, many modified equations have been developed with extra fitting parameters to be descriptive of certain adsorption systems. The drawback of these classical theories is assumptions had to be made to simplify the deduction process. And this can be overcome with the newly developed techniques, such as molecular simulations, that directly take into account the underlying properties of the system.

With the fast development of computer science, molecular simulation has become a powerful tool for the study of the adsorption phenomena. In principle if the interaction potentials of all the components in the adsorption system are known, all the thermodynamic properties can be obtained by molecular simulation. More importantly, one can probe into the microscopic properties of the system and apply conditions that are hardly accessible to experimental studies. The two principal approaches of molecular simulation are Molecular Dynamics (*MD*) and Monte Carlo (*MC*) Simulations [7-9]. In *MD* simulations, the equations of motion of molecules are solved and the properties of the system are calculated as a time average. *MC* simulations use importance sampling to sample the configurational space of the system with the properties calculated as an ensemble average and are preferred for the equilibrium study of the adsorption system.

In practical industry, a large sub-group of materials are those derived from carbon and these carbonaceous materials are widely used as adsorbents for various purposes. Production of carbon materials for industry and the relevant research is an ongoing area of investigation. Amongst the carbon materials, the graphitized carbon black is a very ideal substrate for fundamental studies of the adsorption phenomena because of its structure simplicity and relative homogeneity of the surface [10]. A successful description of the adsorption behaviour of a fluid on graphitized carbon black is a stepping stone towards the simulation of adsorption in more complicated porous solids, which exhibits many interesting adsorption phenomena due to the confinement and the enhanced solid-fluid interactions, such as the freezing/melting transitions [11] and the high pressure effects in the pore [12] which can lead to the deformation of the solid.

Although much work has been done for the study of the adsorption behaviours in carbonaceous solids, there are still many unresolved issues. For example, the hysteresis phenomenon during adsorption on graphitized carbon black and in microporous solid has rarely been studied. Another aspect that needs further investigation is the adsorption-induced solid deformation, as the solid is considered as a rigid body in most studies, however, in reality the adsorbate can induce deformation of the solid which cannot be neglected in certain circumstances.

The first aim of this thesis is to gain a fundamental understanding of adsorption on graphitized carbon black and in graphitic microporous solid, with a particular emphasis on the exhibition of hysteresis and its underlying mechanisms. Another aim of this thesis is to investigate the adsorption-induced deformation in porous solids, which involves the development of a new deformable solid model and a systematic study of the deformation behaviours of graphitic micro- and mesoporous solids.

1.2. Literature Review

Adsorption of gases on solid surfaces and in porous materials exhibit quite different behaviours with the variation of pore size, temperature and solid affinity, which are featured in their adsorption isotherms. In the new IUPAC classification, physisorption isotherms, as shown in Figure 1.1, were grouped into six types [4]. The Type I isotherm is given by microporous solids, such as activated carbon and

molecular sieve zeolites, with a steep uptake at low pressures and a limiting amount adsorbed at the saturation vapour pressure. The Type I(a) isotherm is usually associated with microporous materials having mainly narrow micropores and the Type I(b) isotherm is found in materials having a broader pore size distribution with wider micropores and possibly narrow mesopores. The Type II isotherm and the Type III isotherm are found in nonporous or macroporous solids with the difference that those solids with relatively weak adsorbate-adsorbent interactions present Type III isotherms. The Type IV isotherm is given by mesoporous solids and the Type V isotherm is found in microporous and mesoporous solids with relatively weak adsorbate-adsorbent interactions. The stepwise Type VI isotherm is representative of the layering adsorption on a highly uniform nonporous surface such as graphite and graphitized thermal carbon black. An overview of the characteristics of adsorption on surfaces and in microporous and mesoporous solids is divided into the following three sections, followed by a review of the adsorption-induced solid deformation.

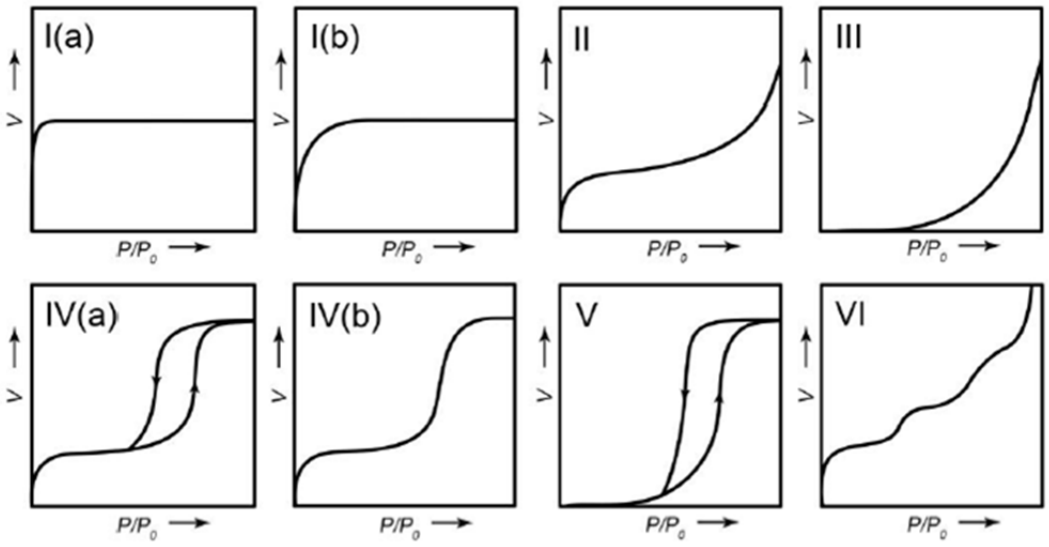

Figure 1.1 Classification of physisorption isotherms according to IUPAC (2015).

1.2.1. Adsorption on Surfaces

The understanding of adsorption on an open surface in a molecular scale was first credited to Langmuir with his equation for the adsorption of fluid on a homogenous surface up to monolayer coverage [5]. In this theory adsorption was described as the equilibrium between molecules being adsorbed onto the surface and those being

desorbed away from the surface. With the assumptions of a homogeneous surface, localized adsorption and negligible interaction among adsorbed molecules, the famous Langmuir equation was derived as:

$$\theta = \frac{bP}{1+bP}; b = b_0 \exp\left(Q / R_g T\right) \tag{1.1}$$

where θ is the fraction of the surface covered by adsorbate molecules at pressure P and temperature T, Q is the heat of adsorption and is equal to the activation energy for desorption, R_g is the gas constant and the parameter b is called the affinity constant or Langmuir constant which describes how strong an adsorbate can adsorb onto the surface. From this point, many empirical equations have been proposed based on the Langmuir equation to fit the experimental isotherms better, such as the Freundlich equation, Sips equation, Toth equation and Unilan equation [13]. For multilayer adsorption on a flat surface, Brunauer, Emmett and Teller are the first to develop a theory with the same assumptions as those in the Langmuir theory and the famous BET equation was derived as [6]:

$$\frac{V}{V_m} = \frac{CP}{\left(P_0 - P\right)\left[1+\left(C-1\right)\left(P/P_0\right)\right]} \tag{1.2}$$

where V is the amount adsorbed at pressure P, V_m is the amount of gas required to form a monolayer, C is called the BET constant and P_0 is the saturation vapour pressure.

Experimentally, adsorption of gases on surfaces such as graphite and graphitized thermal carbon black has been extensively studied [10, 14-76]. Graphitized thermal carbon black is a good experimental subject to represent graphene layers, as it is synthesized by thermal decomposition of a carbonaceous precursor and graphitized at high temperatures (greater than 2700 °C) to produce highly homogeneous basal planes. The investigation of gas adsorption on adsorbents with a homogeneous surface is of great importance for the development of adsorption theories and the study of their intrinsic interactions. Kiselev and co-workers conducted a series of experimental work to study the adsorption isotherms and the heats of adsorption for various gases and vapours on graphitized carbon black, from noble gases,

hydrocarbons to associating fluids [10]. A number of other interesting phenomena, like the step-wise isotherm, sub-steps in the isotherm and the heat spike in the heat curve observed experimentally, were also investigated extensively by many researchers [43-48, 50, 51, 54, 57, 61, 62, 64, 69, 77].

At sufficiently low temperatures, adsorption on highly graphitized carbon black occurs by a layering mechanism and the step-wise isotherm is associated with the two-dimensional (*2D*) phase transitions in each adsorbed layer [50]. The sub-steps usually found in the first layer represent the ordering of the adsorbed molecules. Studies over a wide range of temperatures have shed light on the phase transitions in the adsorbed layers. At temperatures below the *2D*-triple point, the step is resulted from a *2D* gas-solid transition. Between the *2D*-triple point and the *2D*-critical point, *2D* vapour-liquid transition occurs followed by a *2D* liquid-solid transition, corresponding respectively to the step and the sub-step in the isotherm. Above the *2D*-critical temperature, the adsorbate is like a *2D* supercritical fluid and a *2D* supercritical fluid-solid transition can occur depending on temperature, exhibited as a small step in the isotherm. As pressure is increased the *2D* solid could be further rearranged to form a crystalline solid.

Early experimental work on heat of adsorption did not detect any spike in the plot of isosteric heat versus loading, i.e. the heat curve [54, 57]. In 1977 Rouquerol and co-workers observed for the first time the cusp-like dip followed by a sharp peak in the heat curve for nitrogen and argon [69]. Following this, Morrison and co-workers also found sharp peaks in the heat curves for methane, carbon monoxide and nitrogen at loadings close to the monolayer completion [61, 62, 64, 77]. And this sharp peak only appears in certain temperature range.

Another interesting phenomenon that has been paid little attention to is the hysteresis associated with the *2D* transitions, which has been observed experimentally in Kr/graphite, CH_4/graphite and NH_3/graphitized carbon black systems [58, 64, 78]. Inaba and co-workers suggested in their study of CH_4/graphite system that this type of hysteresis is possibly induced by the irreversible restructuring and compression of the lower layers when adsorption occurs in higher layers [64].

Motivated by the experimental observations, molecular simulations have been increasingly used to confirm and shed deeper insights into these phenomena, such as

the *2D* transitions and the heat spike [79-84]. Do and co-workers successfully reproduced the heat spike by Grand Canonical Monte Carlo and proposed a mechanism that it is induced by the increase in both the adsorbate-adsorbate energy and the adsorbate-adsorbent energy, as when adsorption begins to occur in the second layer there are extra molecules squeezed into the first layer and caused a rearrangement of molecules in it [83].

1.2.2. Adsorption in Microporous Solids

In microporous solids, pore walls are in proximity to each other, providing an enhanced adsorption potential. Theories for adsorption in microporous solids include that of Polanyi and particularly that of Dubinin, who coined the term micropore filling. The micropore filling is an important adsorption mechanism only applicable for microporous solids and the Dubinin theory forms the basis for many equations used for the description of equilibrium in microporous solids [85]. One of those well-known equations is the Dubinin-Radushkevich (*DR*) equation:

$$\frac{V}{V_0} = \exp\left[-\left(\frac{A}{\beta E_0}\right)^2\right] \tag{1.3}$$

where V is the amount adsorbed within the micropore at temperature T and relative pressure P/P_0 and V_0 is the maximum volume that the adsorbate can occupy. The quantity $A = R_g T \ln\left(P_0 / P\right)$ is the thermodynamic adsorption potential required to bring one mole of adsorptive to the state of bulk liquid at temperature T. E_0 is the characteristic energy of the reference vapour (benzene for activated carbon) and β is the coefficient of similarity taken as the ratio of the liquid molar volume to that of the reference vapour.

The *DR* equation describes fairly well many carbonaceous solids with a low degree of burn-off, but fails for those with a high degree of burn-off during activation, as the degree of heterogeneity increases with a wider pore size distribution. To this end the Dubinin-Astakhov (*DA*) equation was proposed with a more general form of eq. (1.3) in which the exponent is replaced by a parameter n describing the surface heterogeneity.

During adsorption in microporous solids, fluids could undergo different phase transitions with the formation of new phases compared with the bulk phase behaviour, due to the effects of confinement, enhanced solid potential and reduced dimensionality [86-93]. One of the most noteworthy phenomena is the freezing and melting in the confinement of microporous solids, which has been studied experimentally since the early part of the 20^{th} century and presents a complicated picture [11, 94-96]. The complication lies in the variation of the freezing temperature compared to the bulk fluid and both depression and elevation of the freezing temperature are observed according to the relative adsorbate-adsorbate and adsorbate-adsorbent interactions. In general, the freezing temperature in confinement is lower than the bulk value for weakly attractive walls, while enhanced for strongly attractive walls. When the adsorbate-adsorbate interaction is similar to the adsorbate-adsorbent interaction, and the adsorbate density is similar to that of the adsorbent, there is little or no variation of the freezing temperature for the confined fluid. Many experimental studies have also reported that the contact adsorbed layers adjacent to the pore walls have different structures from that of the inner layers [97]. For strongly attractive walls, the contact layers usually freeze before the inner adsorbed molecules, while the reverse is true for repulsive or weakly attractive walls. Another interesting phenomenon for freezing in confinement is the observation of new phases, such as the existence of a hexatic phase between the fluid and the crystalline phases [97].

Molecular simulations have been carried out by many researchers to study the freezing and melting phenomenon in confinement [80, 97-101]. The results agree qualitatively well with the experimental measurements in terms of the change of the freezing temperature and the phase transitions within the adsorbed layers. One particular interesting study is that done by Vishnyakov and Neimark on the freezing of a Lennard-Jones fluid in confinement by *GCMC* and *MD* simulations [97]. Hexagonal and orthorhombic frozen phases were observed for the adsorbed layers and the freezing temperature was found to be nonmonotonous of the pore width. There also exists a quadratic phase as an intermediate structure during the freezing of a liquid-like phase into a quasi-crystal.

1.2.3. Adsorption in Mesoporous Solids

When the pore is sufficiently large (usually referred to as mesopore) and the temperature is low enough (below the critical temperature of the adsorptive), capillary condensation takes place in the pore which is usually accompanied by hysteresis. The phenomena of capillary condensation and hysteresis in mesoporous solids have been studied in hundreds of papers over more than a century and of immense interest to both scientists and engineers [102-157]. From the beginning of the 20th century, many classical theories have been developed for capillary condensation within slit-like and cylindrical pores (e.g. Kelvin, Cohan theory) [158], as well as for pore structures with connectivity (McBain theory) [159]. The surge in both material synthesis and molecular simulation from the end of the 20th century has led the adsorption science to a higher level in which the phenomena of capillary condensation and hysteresis are better understood.

The first proposed theory for capillary condensation is the famous Kelvin equation, which is widely used to predict the pore condensation pressure based on the similarity of the fluid adsorbed in a pore and the liquid condensed in a capillary tube. Due to the capillary force in small pores, the vapour pressure of the liquid inside such pores is less than that on a flat surface. The Kelvin equation provides a relationship between the pore condensation pressure and the pore radius as well as the temperature and predicts that pore condensation occurs at a higher relative pressure with increased pore radius and temperature:

$$\ln\left(\frac{P}{P_0}\right) = -\frac{2\gamma\cos\theta V_M}{R_g T}\frac{1}{r} \tag{1.4}$$

where P is the pore condensation pressure, P_0 is the saturation vapour pressure of the bulk phase, γ is the surface tension, V_M is the molar volume of the liquid adsorptive, R_g is the gas constant, θ is the contact angle, r is the radius of the pore.

The Kelvin equation was then modified in different ways to be applicable to mesoporous materials, such as the Barrett-Joyner Halenda (*BJH*) method and the approach of Cranston and Inkley (*CI*) [13]. Unlike the Kelvin equation that was established based on the desorption branch, later in 1938, Cohan proposed the

capillary condensation equation for adsorption based on the suggestion of Foster that the hysteresis in adsorption is due to the delay in forming a meniscus in the capillary [158]. This so called Cohan-Kelvin theory provides a classical explanation for pore-filling/emptying and hysteresis in a cylindrical pore in which both adsorption and desorption follow equilibrium paths and the hysteresis depends solely on the difference in the curvature of the meniscus separating the adsorbed phase and the gas-like region. However, similar to the other theories for adsorption on surfaces and in microporous solids, most of the theories for capillary condensation and hysteresis in mesoporous solids are based on many unjustified assumptions and the parameters in these equations are not easily determined a-priori.

Experimental studies have shown that the presence of a hysteresis loop and its shape, size and position depend on the porous structure, pore size and temperature. The existence of hysteresis is associated with a demarcation between smaller and larger pore widths relative to the adsorbate molecule size and the hysteresis can only be observed at temperatures below the critical hysteresis temperature (T_{ch}) [102, 103]. Attempts have been made to classify the different shapes of the hysteresis loops from the extensive experimental measurements of adsorption of various gases in disordered as well as ordered solids. Several classifications have been established and evolved over the past decades as a consequence of the advances in the synthesis of ordered mesoporous materials and the usage of high resolution apparatus for experimental measurement. Recently a new classification, as shown in Figure 1.2, has been proposed by IUPAC [4], which encompasses both the earlier IUPAC classification (1985) [3] and the original classification made by de Boer (1972) [160]. Types H1, H2(a), H3 and H4 were identified in the original IUPAC classification of 1985 and is now extended to six characteristic types, each of which is related to particular features of the pore structure and the underlying adsorption mechanism. For example, the Type H1 loop is usually found in materials with a narrow range of uniform mesopores such as MCM-41, MCM-48, SBA-15, some controlled pore glasses and ordered mesoporous carbons. The Type H2 loop is often observed in solids with more complex pore structures with network coming into play.

Molecular simulation studies have played very important roles in assisting to unravel the underlying mechanisms of capillary condensation/evaporation and hysteresis. There is great flexibility in varying pore shape as well as pore structure from

independent pore to pore network with different types of connectivity, such as slit, cylindrical, spherical and ink-bottle pores as well as disordered pore structures [161]. The equilibrium transition in pores can be determined by different simulation methods such as the Gauge Cell method by Neimark and Vishnyakov [162], and the Mid-Density Scheme by Do and co-workers [163, 164].

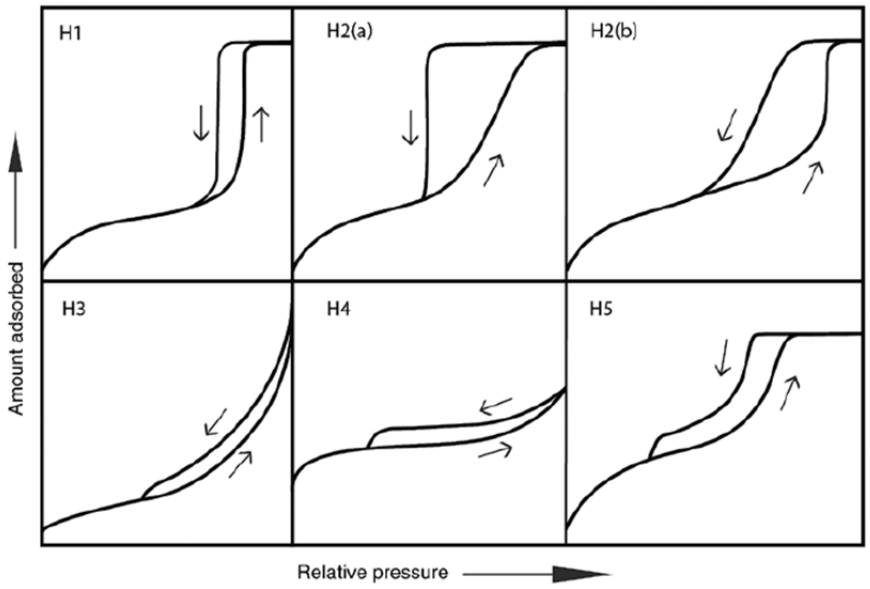

Figure 1.2 Classification of hysteresis loop according to IUPAC (2015).

1.2.4. Adsorption-Induced Solid Deformation

During gas adsorption in porous materials, it could induce deformation of the solid due to the forces exerted by adsorbate molecules on the solid surfaces. This phenomenon of adsorption-induced deformation is ubiquitous and has been studied extensively [165-186] since 1927 when Meehan first observed the expansion of charcoal upon adsorption of carbon dioxide [187]. Later Bangham and co-workers [188-192] published a series of experimental studies on the expansion of charcoal upon exposure to water vapour, ammonia, alcohols and other gases, and put forward the first theory of adsorption-induced solid deformation which states that the solid expansion is proportional to the change of the surface free energy of the solid due to adsorption, that is called the Bangham effect or Bangham's law as given by eq. (1.5):

$$\varepsilon = -k\Delta\gamma \tag{1.5}$$

where ε is the solid strain, k is the elastic constant, $\Delta\gamma = \gamma(\mu) - \gamma_0$ is the change of the surface free energy in which $\gamma(\mu)$ is the surface free energy of the solid covered with adsorbate at chemical potential μ and γ_0 is the reference value of the dry solid. According to the Gibbs adsorption equation, $d\gamma = -\Gamma d\mu$ on the assumption that the surface free energy γ is independent of the surface area A. Therefore, $\Delta\gamma = -\int_{-\infty}^{\mu} \Gamma(\mu') d\mu'$ is negative as the surface excess Γ is positive and the decrease of the surface free energy would always lead to solid expansion at any non-zero loading according to eq. (1.5).

Experimental evidence first contradicting the Bangham's law is the observation of microporous carbon contraction at low pressures made by Haines and McIntosh in the 1940s [193]. This effect was further confirmed by Flood and co-workers in the 50s and 60s in their study of the deformation of carbon rods and it was suggested that the contraction might result from the bridging of adsorbing molecules on opposite pore walls within the micropore [194-196]. Adsorption-induced deformation was also investigated in various microporous and mesoporous materials other than carbon [197-201]. A number of deformation behaviours were found, and both contraction and expansion were recorded. Many microporous solids usually show monotonic expansion/contraction or initial contraction followed by expansion, such as activated carbon and zeolites. The deformation of mesoporous materials, such as porous silicon and porous glass, may exhibit alternative stages of expansion and contraction, and a significant hysteresis could be observed in the course of desorption accompanied with the adsorption-desorption hysteresis. Several attempts have been made to describe adsorption-induced deformation and explain the experimental observations by thermodynamic models, density functional theory and molecular simulation after the thermodynamic studies of Bangham and co-workers [202-215].

Amberg and McIntosh suggested a qualitative theory that the Bangham and capillary effects might compete over a given pressure range in their study of water adsorption in a porous glass rod [202]. Eriksson proposed a thermodynamic theory of the dimensional changes of porous solids during gas adsorption and pointed out that the solid deformation is related with the surface stress but not the surface energy [203]. Ash, Everett, Radke suggested another thermodynamic analysis of the expansion and

contraction of porous bodies caused by adsorption, which considered different contributions to the deformation including the expansion due to the Bangham effect and the expansion/contraction due to the modification of forces of the system [204]. Dolino and co-workers gave a review of the thermodynamic theories of adsorption-induced deformation and applied these theories to explain their experimental observations of pentane adsorption strains in porous silicon [199]. Gor and Neimark used the Derjaguin–Broekhoff–de Boer theory of capillary condensation to describe the deformation of mesoporous solids and suggested a thermodynamic model to calculate the adsorption stress according to the adsorption isotherm [207]. The solvation pressure is the difference between the adsorption stress and the external pressure, which directly determines the magnitude of the elastic deformation of the solids by assuming it follows the Hooke's law. The adsorption stress could also be calculated from the density functional theory, which has been applied by Neimark and co-workers to study the deformation of microporous and mesoporous solids [205, 206, 208, 216, 217]. Recently, Gor and Bernstein compared different approaches of studying solid deformation, i.e. the Bangham's effect, the solvation pressure approach and the method based on the change of the surface stress, and pointed out that the deformation due to adsorption is generally governed by the change of the surface stress [211].

Grand Canonical Monte Carlo was applied by Do and co-workers to investigate the adsorption-induced deformation of infinitely long graphitic slit pores [218, 219]. Their studies show that deformation is a complex function of pore width, temperature, pressure, the species of adsorbate, etc., and the solvation pressure has a direct relationship to the deformation.

1.3. Thesis Objectives

The aim of this thesis is to improve the fundamental understanding of the mechanisms of simple gas adsorption on graphite surfaces and in porous carbon solids as well as the mechanisms of the adsorption-induced solid deformation. To achieve these objectives, a systematic and comprehensive study is conducted by Monte Carlo simulations. The specific objectives of this thesis include:

1. To investigate the adsorption and phase behaviours of simple gas on graphite surface and to reveal the microscopic reasons for hysteresis.

2. To study the adsorption and phase behaviours of simple gas in graphitic slit microporous solid and to reveal the mechanisms of hysteresis.
3. To develop a deformable slit pore model and provide insights into the deformation mechanisms of slit microporous solid at the molecular level.
4. To further investigate the deformation mechanisms of slit mesoporous solid.

1.4. Thesis Development

Chapter 1 presents the background of this thesis, followed by a critical review of the literatures related to this work, and finally the scope and outline of the thesis.

In Chapter 2 the relevant concepts and details of the Monte Carlo simulations are elaborated, which include the different Monte Carlo methods, the potential models used in this study and the equations applied for the calculation of the thermodynamic properties.

Chapter 3 illustrates the investigation of adsorption of simple gas on graphite surface with both the Grand Canonical Monte Carlo and the Canonical kinetic Monte Carlo methods. Chapter 4 presents the simulation results of simple gas adsorption in graphitic slit micropores to show the mechanisms of the hysteresis.

In Chapter 5 a deformable slit pore model is proposed and the microscopic mechanism of the deformation of graphitic slit micropores is studied. Chapter 6 further presents the mechanisms of deformation of graphitic slit mesopores.

Finally, Chapter 7 presents the conclusions of this thesis and some recommendations for future work.

Chapter 2. Aspects of Monte Carlo Simulation

2.1. Introduction

The Monte Carlo method was first introduced by Metropolis *et al.* in 1953 to study the fluid systems with their seminal paper "Equation of State Calculations by Fast Computing Machines" [220, 221]. In the Metropolis algorithm, configurations are chosen with a probability of their occurrence and then weighted evenly, which is termed as importance sampling and relies on the principle of Boltzmann weighting. Later the Metropolis Monte Carlo method was successfully used in many studies to investigate the equilibrium of the adsorption system, which is reached by generating a Markov chain with a sequence of configurations and the thermodynamic properties of the system are calculated as ensemble averages. In addition to the Monte Carlo method with the Metropolis algorithm, also called the conventional Monte Carlo, the kinetic Monte Carlo has been developed over the past few decades, which is initially aimed to analyse systems dynamically and also demonstrates potential in studying equilibrium systems [79, 99, 222]. In Monte Carlo simulations, there are a number of ensembles that are commonly used, i.e. canonical (constant *NVT*), grand canonical (constant μVT), isobaric-isothermal (constant *NPT*), isotension-isothermal (constant *NST*) ensembles [8]. The descriptions of the Monte Carlo methods in different ensembles used in this thesis will be presented in Section 2.2.

2.2. Monte Carlo Simulation

2.2.1. Canonical Monte Carlo (CMC)

The canonical ensemble describes an isolated system with constant number of adsorbate molecules (*N*), system volume (*V*) and temperature (*T*). The brief procedure of the conventional Monte Carlo simulation in the canonical ensemble is as below:

1. Set up the simulation box, which is usually rectangular, and put *N* particles randomly in it.
2. Calculate the configuration energy of the system, *U*, and then choose a particle at random.
3. The chosen particle is moved randomly from its initial position *(x, y, z)* to a new position *(x', y', z')*. This movement is called the displacement.

4. Calculate the energy of the new configuration of the system, *U'*.
5. The new configuration of the system is either accepted or rejected according to the following probability

$$P^{acc} = \min\left(1, \exp\left\{-\beta\left(U' - U\right)\right\}\right) \tag{2.1}$$

where $\beta = 1/k_B T$ is the reciprocal temperature, with $k_B = 1.38066 \times 10^{-23} J/K$ being the Boltzmann's constant.

6. If the trial displacement is accepted, the positions of the particles and the energy of the system will be updated to the new configuration. Otherwise, the old configuration is recounted.
7. Sum up the properties of the system. After *N* steps, the sum of the property *X* is $\sum_{i=1}^{N} X_i$, where X_i is the property at the i^{th} configuration.
8. The trials should be repeated for a sufficient number of configurations to ensure the system reach equilibrium with a long enough Markov chain. The ensemble average for a thermodynamic property X is

$$\langle X \rangle = \frac{\sum_{i=1}^{N} X_i}{N} \tag{2.2}$$

Above is the main procedure for the *CMC* simulation. For rigid molecules with multi-site, the rotation of the molecules should be considered in addition to the displacement.

2.2.2. Grand Canonical Monte Carlo (GCMC)

The Grand Canonical Monte Carlo (*GCMC*) was first introduced by Norman and Filinov [223] and has become the most commonly used Monte Carlo method in adsorption studies. It is conducted under the conditions of fixed chemical potential (μ), temperature (T) and volume (V). The number of adsorbate molecules is allowed to fluctuate as the system is in a sense connected to the bulk reservoir with the same chemical potential and temperature, which mimics the same conditions that are usually used in adsorption experiments.

Apart from the displacement of a particle as conducted in *CMC*, there are two additional moves involved in *GCMC*: insertion and deletion of a particle. For the insertion of a particle, a particle is inserted into a randomly chosen position inside the simulation box. A random rotation of the inserted particle is carried out simultaneously for a multi-site rigid molecule. The probability of accepting the insertion is given by:

$$P^{acc} = \min\left(1, \frac{V}{\Lambda^3 (N+1)} \exp\left\{\beta\left(\mu - U' + U\right)\right\}\right) \tag{2.3}$$

where N is the number of particles in the simulation box, Λ is the thermal de Broglie wavelength, U and U' are the energies of the system before and after the insertion, respectively.

The deletion is conducted by removing a randomly selected particle from the N particles in the simulation box and the probability of acceptance is given by:

$$P^{acc} = \min\left(1, \frac{\Lambda^3 N}{V} \exp\left\{-\beta\left(\mu + U' - U\right)\right\}\right) \tag{2.4}$$

where U and U' are the energies of the system before and after the deletion, respectively.

Similar as the displacement of a particle, if the trial insertion or deletion is accepted, the new configuration of the system will be updated to the Markov chain, otherwise the old configuration will be recounted. In order to maintain the microscopic reversibility, the system must have equal probabilities for insertion and deletion in the grand canonical ensemble.

2.2.3. Canonical kinetic Monte Carlo (C-kMC)

The main difference between this *C-kMC* and *CMC* is the way of conducting the particle displacement, which are detailed as below:

1. The choice of a particle to be displaced depends on the current state of the system, i.e. the mobility of the system which will be described later in this section.

2. The particle is displaced to a random position in the simulation box which is chosen uniformly.
3. This displacement is always accepted, irrespective of whether the displaced particle has highly repulsive interaction energy with other molecules in the system.

In a canonical ensemble with N molecules in the simulation box at constant volume V and temperature T, the molecular interaction energy for a molecule i, which interacts with surrounding molecules and any external solid surfaces, is:

$$u_i = \sum_{\substack{j=1 \\ j \neq i}}^{N} \varphi_{i,j} + \varphi_{i,S} \tag{2.5}$$

where $\varphi_{i,j}$ is the pairwise interaction energy between molecule i and molecule j, $\varphi_{i,S}$ is the interaction energy between molecule i and the solid. The molecular mobility of the molecule i is defined as

$$v_i = \exp\left(\frac{u_i}{k_B T}\right) \tag{2.6}$$

The total mobility of all the molecules in the system is given by:

$$R = \sum_{i=1}^{N} v_i \tag{2.7}$$

The time that the system spends in a given configuration is inversely proportional to the total mobility of the system and is expressed by:

$$\Delta t = \frac{1}{R} \ln\left(\frac{1}{p}\right) \tag{2.8}$$

where p is a random number ($0 < p < 1$).

A particle (the *k-th* particle) is selected to move according to the Rosenbluth algorithm when the following criterion is satisfied:

$$R_{k-1} \leq pR < R_k \tag{2.9}$$

where $R_0 = 0$, $R = R_N$, N is the number of molecules in the system, $R_k = \sum_{i=1}^{k} v_i$, which is the partial sum of the reduced molecular rates. This ensures that a molecule with higher energy will have a greater chance of being selected for displacement. As the *kMC* is a rejection-free method, it saves the computational costs of assessing acceptance probability of a trial move.

2.3. Thermodynamic Property Calculations

2.3.1. Potential Energy

Fluid-Fluid Potential

The Lennard-Jones (*LJ*) model is the most commonly used potential model to describe the interaction between two dispersive sites, because it is relatively simple and its parameters are readily available for a wide range of fluids. Moreover, this model is consistent with the well-known potential equations that are used to calculate the solid-fluid interactions, such as the Steele [224] and Bojan-Steele equations [225-228]. The Lennard-Jones 12-6 potential equation to calculate the interaction energy between two isolated fluid molecules of the same type is shown as below:

$$\varphi_{ff}(r) = 4\varepsilon_{ff}\left[\left(\frac{\sigma_{ff}}{r}\right)^{12} - \left(\frac{\sigma_{ff}}{r}\right)^{6}\right] \tag{2.10}$$

where r is the separation distance between the two molecules, ε_{ff} is the well-depth of the interaction energy and σ_{ff} is the collision diameter at which the ε_{ff} is zero.

For a molecule with many dispersive sites and fixed partial charges, the interaction energy between two molecules is given by the sum of the *LJ* and the Coulomb interactions:

$$\varphi_{ij} = \sum_{a=1}^{A}\sum_{b=1}^{B}\frac{q_i^a q_j^b}{4\pi\varepsilon_0 r_{ij}^{ab}} + \sum_{c=1}^{C}\sum_{d=1}^{D}4\varepsilon_{ij}^{cd}\left[\left(\frac{\sigma_{ij}^{cd}}{r_{ij}^{cd}}\right)^{12} - \left(\frac{\sigma_{ij}^{cd}}{r_{ij}^{cd}}\right)^{6}\right] \tag{2.11}$$

where φ_{ij} is the interaction energy between fluid molecules i and j, A and B are the numbers of partial charges on the molecules i and j, respectively, C and D are the

numbers of *LJ* sites on the molecules *i* and *j*, respectively, ε_0 is the permittivity of a vacuum, r_{ij}^{ab} is the separation distance between charge *a* on molecule *i* and charge *b* on molecule *j* having charges q_i^a and q_j^b, respectively, r_{ij}^{cd} is the separation distance between the *LJ* site *c* on molecule *i* and the *LJ* site *d* on molecule *j*, σ_{ij}^{cd} and ε_{ij}^{cd} are the combined *LJ* collision diameter and well-depth for the two *LJ* sites, respectively, which are calculated by the Lorentz-Berthelot mixing rules:

$$\sigma_{ij}^{cd} = \frac{\sigma_i^c + \sigma_j^d}{2} \qquad \varepsilon_{ij}^{cd} = \sqrt{\varepsilon_i^c \varepsilon_j^d} \tag{2.12}$$

Solid-Fluid Potential

There are two approaches that are commonly used to model the surface of carbon adsorbents. One is the structured solid model consisted of discrete carbon atoms, which are arranged in hexagonal units with a carbon-carbon bond length of 0.142 nm. The other is the unstructured model where the solid is composed of structureless graphene layers with constant density of carbon atoms. It has been proved that identical results can be obtained with these two models, provided the temperature of the system is high enough so that the barrier between the hexagonal sites is less than $k_B T$.

Structured model

To calculate the solid-fluid interaction energy for the structured surface, all pairwise interactions between each site of a molecule *i* and each carbon atom on the surface are summed up by using eq. (2.10), with the molecular parameters replaced by $\sigma_{i,s}$ and $\varepsilon_{i,s}$. The total solid-fluid interaction $\varphi_{i,s}$ is then calculated from:

$$\varphi_{i,s} = \sum_{a=1}^{M} \varphi_{i,a} \tag{2.13}$$

where the subscript *s* denotes the graphite surface and *M* is the number of carbon atoms of the graphite surface.

Infinite unstructured model

The solid-fluid interaction energy between a particle *i* and a homogeneous flat solid surface of infinite extent is calculated by the Steele 10-4-3 potential:

$$\varphi_{i,s} = 2\pi\rho_s\varepsilon_{sf}\sigma_{sf}^2\left\{\frac{2}{5}\left(\frac{\sigma_{sf}}{z_i}\right)^{10} - \left(\frac{\sigma_{sf}}{z_i}\right)^{4} - \frac{\sigma_{sf}^4}{3\Delta\left(0.61\Delta + z_i\right)^3}\right\} \tag{2.14}$$

where ρ_s is the surface carbon atom density of a graphene layer (38.2 nm^{-2}), Δ is the spacing between two adjacent graphene layers (0.3354 nm), z_i is the shortest distance between the particle and the surface. The solid-fluid molecular parameters, the cross collision diameter σ_{sf} and well-depth ε_{sf}, are calculated from the Lorentz-Berthelot mixing rule with $\sigma_{ss} = 0.34$ nm and $\varepsilon_{ss}/k = 28$ K.

Finite unstructured model

The Bojan-Steele potential is used to describe the interaction energy between a particle and a homogenous surface which is infinite in extent in the *x*-direction and finite in the *y*-direction and is given by:

$$\varphi_{f,s} = 2\pi\rho_s\varepsilon_{sf}\sigma_{sf}^2\left\{\left[\varphi_{rep}\left(z,y^+\right) - \varphi_{rep}\left(z,y^-\right)\right] - \left[\varphi_{att}\left(z,y^+\right) - \varphi\left(z,y^-\right)\right]\right\} \tag{2.15}$$

where *z* is the shortest distance between the particle and the surface, ρ_s is the surface density, σ_{sf} and ε_{sf} are the solid-fluid molecular parameters. The variables y^+ and y^- are the y-coordinates of the right hand edge and the left hand edge of the surface relative to the position of the fluid particle:

$$y^+ = \frac{W}{2} - y \qquad y^- = -\frac{W}{2} - y \tag{2.16}$$

The configuration of the surface with the origin of the *y*-coordinate at the centre of the surface is shown in Figure 2.1. The repulsive and attractive functions on the *RHS* of eq. (2.15) are given by:

$$\varphi_{rep}\left(z,y\right) = \frac{y}{\sqrt{y^2+z^2}}\left[\begin{array}{l}\frac{1}{5}\frac{\sigma_{sf}^{10}}{z^{10}} + \frac{1}{10}\frac{\sigma_{sf}^{10}}{z^8\left(y^2+z^2\right)} + \\ \frac{3}{40}\frac{\sigma_{sf}^{10}}{z^6\left(y^2+z^2\right)^2} + \frac{1}{16}\frac{\sigma_{sf}^{10}}{z^4\left(y^2+z^2\right)^3} + \frac{7}{128}\frac{\sigma_{sf}^{10}}{z^2\left(y^2+z^2\right)^4}\end{array}\right] \tag{2.17}$$

$$\varphi_{att}(z,y)=\frac{y}{\sqrt{y^2+z^2}}\left[\frac{1}{2}\frac{\sigma_{sf}^4}{z^4}+\frac{1}{4}\frac{\sigma_{sf}^4}{z^2\left(y^2+z^2\right)}\right] \tag{2.18}$$

The potential equation (2.15) is valid for any particle around the surface. When the particle is positioned exactly on the same level as the surface, i.e. at $z=0$, eqs. (2.17) and (2.18) become undefined. In this case, we take a Taylor series expansion of these two equations and find their limit when *z* approaches zero:

$$\lim_{z\to 0}\varphi_{rep}=\frac{y}{\sqrt{y^2}}\left[\frac{1}{5}\left(\frac{\sigma_{sf}}{z}\right)^{10}-\frac{63}{1280}\left(\frac{\sigma_{sf}}{y}\right)^{10}+O\left(z^2\right)\right] \tag{2.19}$$

$$\lim_{z\to 0}\varphi_{att}=\frac{y}{\sqrt{y^2}}\left[\frac{1}{2}\left(\frac{\sigma_{sf}}{z}\right)^{4}-\frac{3}{16}\left(\frac{\sigma_{sf}}{y}\right)^{4}+O\left(z^2\right)\right] \tag{2.20}$$

Substituting eqs. (2.19) and (2.20) into eq. (2.15), we can get the solid-fluid potential at $z=0$:

$$\varphi_{f,s}=\psi 2\pi\rho_s\varepsilon_{sf}\sigma_{sf}^2\left\{\frac{63}{1280}\left[\left(\frac{\sigma_{sf}}{y^-}\right)^{10}-\left(\frac{\sigma_{sf}}{y^+}\right)^{10}\right]-\frac{3}{16}\left[\left(\frac{\sigma_{sf}}{y^-}\right)^{4}-\left(\frac{\sigma_{sf}}{y^+}\right)^{4}\right]\right\} \tag{2.21}$$

where $\psi=1$ for positive y^+ and y^-, $\psi=-1$ for negative y^+ and y^-. It can be seen that there is no singularity in the solid-fluid potential energy as one would expect physically. The potential energy in the region of small *z* can be calculated from a Taylor series expansion of the Bojan-Steele equation (eq. 2.15) as:

$$\frac{\varphi_{f,s}}{\psi 2\pi\rho_s\varepsilon_{sf}\sigma_{sf}^2}=\left\{\frac{63}{1280}\left[\left(\frac{\sigma_{sf}}{y^-}\right)^{10}-\left(\frac{\sigma_{sf}}{y^+}\right)^{10}\right]-\frac{3}{16}\left[\left(\frac{\sigma_{sf}}{y^-}\right)^{4}-\left(\frac{\sigma_{sf}}{y^+}\right)^{4}\right]\right\}$$
$$-\left(\frac{z}{\sigma_{sf}}\right)^2\left\{\frac{231}{1024}\left[\left(\frac{\sigma_{sf}}{y^-}\right)^{12}-\left(\frac{\sigma_{sf}}{y^+}\right)^{12}\right]-\frac{5}{16}\left[\left(\frac{\sigma_{sf}}{y^-}\right)^{6}-\left(\frac{\sigma_{sf}}{y^+}\right)^{6}\right]\right\}$$
$$+\left(\frac{z}{\sigma_{sf}}\right)^4\left\{\frac{1287}{2048}\left[\left(\frac{\sigma_{sf}}{y^-}\right)^{14}-\left(\frac{\sigma_{sf}}{y^+}\right)^{14}\right]-\frac{105}{256}\left[\left(\frac{\sigma_{sf}}{y^-}\right)^{8}-\left(\frac{\sigma_{sf}}{y^+}\right)^{8}\right]\right\}$$
$$-\left(\frac{z}{\sigma_{sf}}\right)^6\left\{\frac{45045}{32768}\left[\left(\frac{\sigma_{sf}}{y^-}\right)^{16}-\left(\frac{\sigma_{sf}}{y^+}\right)^{16}\right]-\frac{63}{128}\left[\left(\frac{\sigma_{sf}}{y^-}\right)^{10}-\left(\frac{\sigma_{sf}}{y^+}\right)^{10}\right]\right\}$$
$$+\left(\frac{z}{\sigma_{sf}}\right)^8\left\{\frac{85085}{32768}\left[\left(\frac{\sigma_{sf}}{y^-}\right)^{18}-\left(\frac{\sigma_{sf}}{y^+}\right)^{18}\right]-\frac{1155}{2048}\left[\left(\frac{\sigma_{sf}}{y^-}\right)^{12}-\left(\frac{\sigma_{sf}}{y^+}\right)^{12}\right]\right\}$$
$$+O\left(\frac{z}{\sigma_{sf}}\right)^{10} \tag{2.22}$$

where $\psi=1$ for positive y^+ and y^-, $\psi=-1$ for negative y^+ and y^-.

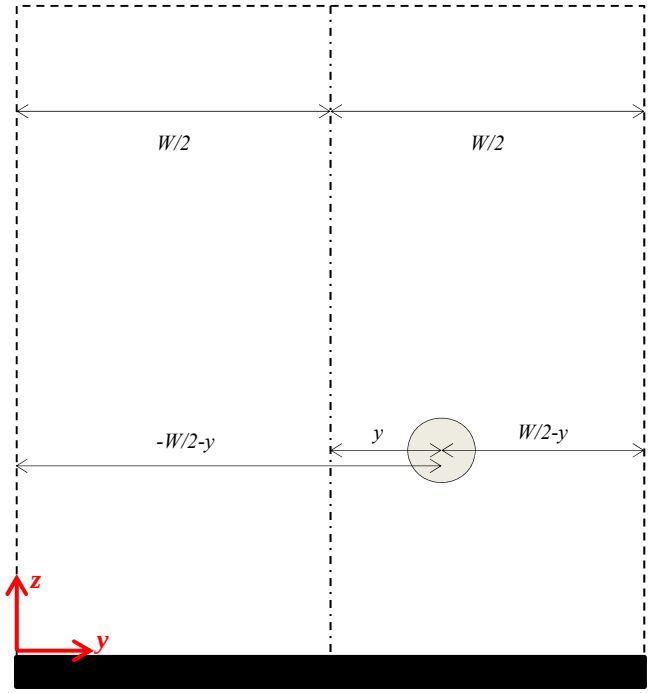

Figure 2.1 Schematic diagram of the finite stripe, which is finite in the *y*-direction and infinite in the *x*-direction (perpendicular to the page).

Solid-Solid Potential

In the studies of the adsorption-induced solid deformation, the solid-solid potential should be considered as part of the total potential energy of the system. For pores of finite length in the *y*-direction and infinite extent in the *x*-direction, the solid-solid interaction energy between two layers is calculated by integrating the Bojan-Steele equation, which is the sum of the interactions of all carbon atoms within one layer with the other. The interaction energy between a carbon atom with a solid layer can be calculated with the Bojan-Steele equation as described in eq. (2.15) with the molecular parameters replaced by σ_{ss} and ε_{ss}.

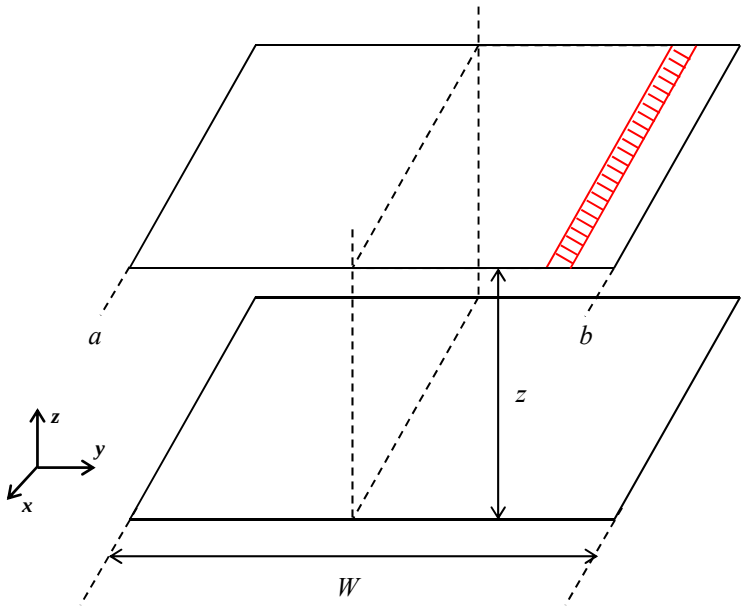

Figure 2.2 Schematic diagram of two solid layers modelled by the Bojan-Steele potential; *z* is the separation distance between the two layers in the *z*-direction; *W* is the length of the layer underneath in the *y*-direction; *a* and *b* are the lower and higher boundaries of the top layer in the *y*-direction, respectively.

For two solid layers described by the Bojan-Steele potential as shown in Figure 2.2, the interaction energy of all carbon atoms in the red differential strip of the top layer with the other layer underneath is

$$d\varphi_{ss} = 2\pi\rho_s\varepsilon_{ss}\sigma_{ss}^2\left\{\left[\varphi_{rep}\left(z,y^+\right)-\varphi_{rep}\left(z,y^-\right)\right]-\left[\varphi_{att}\left(z,y^+\right)-\varphi_{att}\left(z,y^-\right)\right]\right\}\times L_x\rho_s dy \tag{2.23}$$

where z is the separation distance between the two layers, L_x is the length of the simulation box in the x-direction.

By integrating eq. (2.23), we can get the final solution of the solid-solid interaction energy:

$$\varphi_{ss} = 2\pi\rho_s\varepsilon_{ss}\sigma_{ss}^2\int_a^b\left\{\left[\varphi_{rep}\left(z,y^+\right)-\varphi_{rep}\left(z,y^-\right)\right]-\left[\varphi_{att}\left(z,y^+\right)-\varphi_{att}\left(z,y^-\right)\right]\right\}\times L_x\rho_s dy \tag{2.24}$$

where a and b are the lower and higher boundaries of the top solid layer in the y-direction, respectively. The integrals for the repulsive and attractive functions are:

$$\int_a^b\varphi_{rep}\left(z,y^{\pm}\right)dy =$$

$$\left\{-\frac{1}{5}\frac{\sigma_{ss}^{10}}{z^{10}}\sqrt{\left(\pm W/2-b\right)^2+z^2}+\frac{1}{10}\frac{\sigma_{ss}^{10}}{z^8}\frac{1}{\sqrt{\left(\pm W/2-b\right)^2+z^2}}+\frac{1}{40}\frac{\sigma_{ss}^{10}}{z^6}\frac{1}{\left(\left(\pm W/2-b\right)^2+z^2\right)^{\frac{3}{2}}}\right.$$
$$\left.+\frac{1}{80}\frac{\sigma_{ss}^{10}}{z^4}\frac{1}{\left(\left(\pm W/2-b\right)^2+z^2\right)^{\frac{5}{2}}}+\frac{1}{128}\frac{\sigma_{ss}^{10}}{z^2}\frac{1}{\left(\left(\pm W/2-b\right)^2+z^2\right)^{\frac{7}{2}}}\right\}-$$
$$\left\{-\frac{1}{5}\frac{\sigma_{ss}^{10}}{z^{10}}\sqrt{\left(\pm W/2-a\right)^2+z^2}+\frac{1}{10}\frac{\sigma_{ss}^{10}}{z^8}\frac{1}{\sqrt{\left(\pm W/2-a\right)^2+z^2}}+\frac{1}{40}\frac{\sigma_{ss}^{10}}{z^6}\frac{1}{\left(\left(\pm W/2-a\right)^2+z^2\right)^{\frac{3}{2}}}\right.$$
$$\left.+\frac{1}{80}\frac{\sigma_{ss}^{10}}{z^4}\frac{1}{\left(\left(\pm W/2-a\right)^2+z^2\right)^{\frac{5}{2}}}+\frac{1}{128}\frac{\sigma_{ss}^{10}}{z^2}\frac{1}{\left(\left(\pm W/2-a\right)^2+z^2\right)^{\frac{7}{2}}}\right\} \tag{2.25}$$

$$\int_a^b \varphi_{att}\left(z, y^{\pm}\right) dy = \left\{ -\frac{1}{2}\frac{\sigma_{ss}^4}{z^4}\sqrt{\left(\pm W/2 - b\right)^2 + z^2} + \frac{1}{4}\frac{\sigma_{ss}^4}{z^2}\frac{1}{\left(\left(\pm W/2 - b\right)^2 + z^2\right)^{\frac{1}{2}}} \right\}$$
$$- \left\{ -\frac{1}{2}\frac{\sigma_{ss}^4}{z^4}\sqrt{\left(\pm W/2 - a\right)^2 + z^2} + \frac{1}{4}\frac{\sigma_{ss}^4}{z^2}\frac{1}{\left(\left(\pm W/2 - a\right)^2 + z^2\right)^{\frac{1}{2}}} \right\} \tag{2.26}$$

2.3.2. Chemical Potential

The chemical potential of a system is composed of the ideal and excess parts:

$$\mu = \mu_{id} + \mu_{ex} = -k_B T \ln\left(\frac{V/\Lambda^d}{N}\right) + \mu_{ex} \tag{2.27}$$

where V is the volume of the system, d is the dimensionality of the system, N is the number of particles.

The evaluation of the ideal chemical potential is straightforward. The excess chemical potential is defined in thermodynamics as the partial derivative of the potential energy to the number of particles in the system:

$$\mu_{ex} = \left(\frac{\partial U}{\partial N}\right)_{T,V} \tag{2.28}$$

The Widom particle insertion method based on statistical mechanics is commonly used to measure the excess chemical potential by a perturbation in the number of particles in the *NVT* ensemble [229, 230]. A test particle is inserted at a random position inside the simulation box at frequent intervals during the simulation, and the energy between the test particle and all the particles of the system is calculated for N_{test} particles and the ensemble average is calculated as:

$$\left\langle \exp\left(-\frac{U_{test}}{k_B T}\right)\right\rangle = \frac{1}{N_{cycle} N_{test}} \sum_{n=1}^{N_{cycle}} \sum_{j=1}^{N_{test}} \exp\left(-\frac{U_{test}}{k_B T}\right) \tag{2.29}$$

where N_{cycle} is the number of cycles that the insertion of N_{test} particles is carried out. The excess chemical potential is then calculated from:

$$\mu_{ex} = -k_B T \ln \left\langle \exp\left(-\frac{U_{test}}{k_B T} \right) \right\rangle \tag{2.30}$$

The Widom method is a very powerful scheme for computing the chemical potential of not too dense systems and simple molecules. For dense systems and complex molecules it becomes unreliable because the test particles are often overlapped with the real particles in the system.

Another way of calculating the chemical potential is by the equation of state (*EOS*). The Johnson et al.'s *EOS* can evaluate the chemical potential of *LJ* fluids and is used in the *GCMC* simulations in this thesis [231].

2.3.3. Pressure

The pressure of a bulk system in the *NVT* simulation can be calculated through the equation:

$$P = \frac{N k_B T}{V} + P_{ex} \tag{2.31}$$

where the excess pressure can be calculated as the pair-wise sum of the virial function [9]:

$$P_{ex} = -\frac{1}{3V} \left\langle \sum_{i=1}^{N-1} \sum_{j=i+1}^{N} r_{ij} \left(\frac{d\varphi_{ij}}{dr} \right) \Bigg|_{r_{ij}} \right\rangle \tag{2.32}$$

2.3.4. Surface Excess Density

In simulation, the surface excess of adsorption is defined as the excess above a reference amount:

$$\Gamma = \frac{\langle N \rangle - V_{acc} \rho_G}{S} \tag{2.33}$$

where $\langle N \rangle$ is the ensemble average of the number of particles in the system, V_{acc} is the accessible volume, ρ_G is the density of the bulk gas phase, S is the surface area of the solid.

The accessible volume is proposed by Do et al. [232] and is defined as the volume accessible to the centre of the mass of a molecule at zero loading. The method of calculating the accessible volume is as follows: the centre of mass of a molecule is inserted at a randomly chosen position in the simulation box and for a multi-site molecule, the molecule is given *M* different orientations. If the potential energies of these *M* orientations are all positive, this insertion is regarded as a failure; otherwise, this insertion is a success. This process is repeated and the accessible volume is calculated as $V_{acc} = V_{box} f$, where V_{box} is the volume of the simulation box and f is the fraction of successful insertions.

2.3.5. Pore Density

The absolute pore density with respect to the accessible volume is given by:

$$\rho = \frac{\langle N \rangle}{V_{acc}} \tag{2.34}$$

where $\langle N \rangle$ is the ensemble average of the number of particles in the pore. Any other volumes could also be used to define the pore density, but eq. (2.34) is the most appropriate to provide a better description of how dense the adsorbed phase is.

2.3.6. Isosteric Heat

One of the basic properties in adsorption studies is the isosteric heat, which is defined as the infinitesimal change in the adsorbate enthalpy to the infinitesimal change in the excess adsorbed amount. In simulation, the fluctuation of thermodynamic properties can be used to calculate a number of thermodynamic partial derivatives [7]. The nature of thermodynamic fluctuations and their connection to thermodynamic derivatives can be found in many books about statistical mechanics. In *GCMC* simulations, the isosteric heat can be obtained by applying the thermodynamic fluctuations:

$$q_{st} = k_B T - \frac{f(U,N)}{f(N,N) - \overline{N}_G} \tag{2.35}$$

where $\overline{N}_G$ is the number of molecules of an ideal gas that would occupy the adsorption space. Most work on adsorption neglects the second term in the denominator, and the equation is commonly used in the following form with the assumptions of ideal gas and a smaller molar volume of the adsorbed phase compared to the gas phase:

$$q_{st} = k_B T - \frac{f(U,N)}{f(N,N)} \tag{2.36}$$

where U is the configuration energy of the system, N is the number of particles, the function f is defined as $f(X,Y) = \langle X,Y \rangle - \langle X \rangle \langle Y \rangle$ with the notation $\langle\ \rangle$ represents the ensemble average. The assumptions of the above equation are reasonable for subcritical fluids, but become invalid for supercritical fluids or subcritical conditions close to the critical point, as the adsorptive density may be significant compared to the adsorbed density. A more general equation for the isosteric heat was proposed by Do et al. [233]

In a canonical ensemble, the differential heat of adsorption is defined as the change of the energy of the adsorbed phase per unit change in the excess number, shown in the following equation:

$$q_{diff} = k_B T - \frac{\partial\{\langle U \rangle - \langle U_G \rangle\}}{\partial\{N - N_G\}} \tag{2.37}$$

where U is the energy of the system, U_G is the energy of the bulk gas obtained as $\langle U_G \rangle = \frac{V}{V_M} \langle U_M \rangle$, with V_M being the volume of the region of the bulk phase and U_M being the energy of this region, N_G is the hypothetical number of particles occupying the accessible volume at the same density as the bulk gas.

2.3.7. Compressibility

Compressibility is defined as the negative of the relative volume change with respect to pressure at constant temperature. In *GCMC*, the local compressibility can be expressed in terms of the corresponding particle number fluctuation as:

$$\kappa = -\frac{1}{V}\frac{\partial V}{\partial p} = \frac{1}{k_B T \langle \rho_k \rangle}\frac{f(N_k, N_k)}{\langle N_k \rangle} = \frac{F_k}{k_B T \langle \rho_k \rangle} \tag{2.38}$$

where ρ_k is the density of bin k. F_k is the local number fluctuation, which approaches unity, i.e. $\lim_{N_k \to 0} f(N_k, N_k)/\langle N_k \rangle = 1$, when the gas phase is very dilute.

2.3.8. Solvation Pressure

The solvation pressure exerted by the adsorbate on the solid is

$$P_{solv} = \frac{1}{S}\left\langle -\sum_{i=1}^{N}\frac{\partial \varphi_i}{\partial z}\right\rangle \tag{2.39}$$

where S is the total surface area of the solid exposed to the adsorbate, φ_i is the solid-fluid interaction energy of particle i with the solid and z is the shortest distance between the adsorbate and the solid surface.

2.4. Microscopic Analysis

2.4.1. Local Density Distribution

The local density at the distance z from the solid surface is defined as:

$$\rho(z) = \frac{\langle \Delta N(z) \rangle}{L_x L_y \Delta z} \tag{2.40}$$

where $\Delta N(z)$ is the number of particles whose centres of mass are located in the segment between z and $z + \Delta z$, L_x and L_y are the dimensions of the solid surface in the x- and y-directions, respectively.

2.4.2. Radial Density Distribution

The radial density is calculated by finding the number of particles whose centres of mass are located at a radial distance *r* from the centre of any given particle:

$$\rho(r) = \frac{\langle \Delta N(r) \rangle}{\frac{4}{3}\pi\left[(r+\Delta r)^3 - r^3\right]} \tag{2.41}$$

where $\Delta N(r)$ is the number of particles in the radial bin bounded between *r* and $r+\Delta r$.

2.4.3. Orientation Density Distribution

The orientation density is calculated from the following equation:

$$\rho(z,\theta) = \frac{\langle \Delta N(z,\theta) \rangle}{L_x L_y \Delta z \sin\theta \Delta\theta} \tag{2.42}$$

where $\Delta N(z,\theta)$ is the number of particles whose centres of mass are in the segment between z and $z+\Delta z$, with angles between the molecular axis and the z direction between θ and $\theta+\Delta\theta$. The orientation density distribution with z and θ can help to evaluate the preferential orientation of the particles located at various distances from the solid surface. $\theta = 0$ means the particles are located perpendicular to the solid surface and $\theta = \frac{\pi}{2}$ a parallel orientation.

2.4.4. 2D Density Profile

The *2D* density is defined as the local density of a two-dimensional bin with the system divided into bins in the *z*- and *y*-directions:

$$\rho(z,y) = \frac{\langle \Delta N(z,y) \rangle}{L_x \Delta z \Delta y} \tag{2.43}$$

where $\Delta N(z,y)$ is the number of particles in the bin bounded by $[z, z+\Delta z]$ and $[y, y+\Delta y]$. The bin size in both dimensions is chosen to be $\Delta z = \Delta y = 0.1\sigma_{ff}$. The

results of the *2D* density profile are smoothed by averaging the density within a radius of $0.5\sigma_{ff}$.

2.4.5. Local Solvation Pressure Distribution

The local solvation pressure in the *z*-direction is defined as the sum of the forces per unit area exerted on the solid by particles in the segment bounded by z and $z+\Delta z$:

$$f(z)=\frac{1}{S}\left\langle -\sum_{i\in(z,z+\Delta z)}\frac{\partial \varphi_i}{\partial z}\right\rangle \tag{2.44}$$

where S is the surface area of the solid, φ_i is the solid-fluid interaction energy of particle i with the solid.

2.5. Setup of Simulation Systems

2.5.1. Bulk Fluids

To simulate bulk fluids, the simulation box is a cubic box with periodic boundary conditions imposed on boundaries in all directions. For the initial configuration, particles are placed at randomly chosen positions in the box.

2.5.2. Adsorption Systems

The most important difference of simulations of the adsorption systems from those of the bulk phase is that the system is no longer isotropic. In this study, the solid is placed on the plane perpendicular to the *z*-direction and there is no periodicity in this direction.

Graphite Surface

To simulate adsorption on a graphite surface, two approaches can be used to set up the simulation system. The first is a slit pore with a pore width large enough so that there is no overlap between the potential energies exerted by the two opposite pore walls, which therefore can be treated as two independent surfaces. The other is by putting a graphite surface at one boundary and a hard wall at the opposite end. The latter approach is usually used for systems under sub-critical conditions. However, for systems with high bulk gas density, the first approach is used to avoid the spurious effects at the hard wall.

Slit Pore

Slit-shaped pores are set up with two graphite surfaces parallel to each other. If the pore has infinite length (Figure 2.3a), periodic boundary conditions are applied in both the *x*- and *y*-directions. For pores of finite length (Figure 2.3b), the two open ends of the pore are connected to bulk gas reservoirs in the *y*-direction and molecules within the pore can interact with the bulk phase to maintain a mechanical equilibrium between the pore and the surroundings. In this model, periodic boundary condition is only applied in the *x*-direction. In both pore models, the pore width is defined as the distance between the plane passing though the centres of carbon atoms in the innermost layer of one wall and the corresponding plane of the opposite wall (denoted as *H* in Figure 2.3).

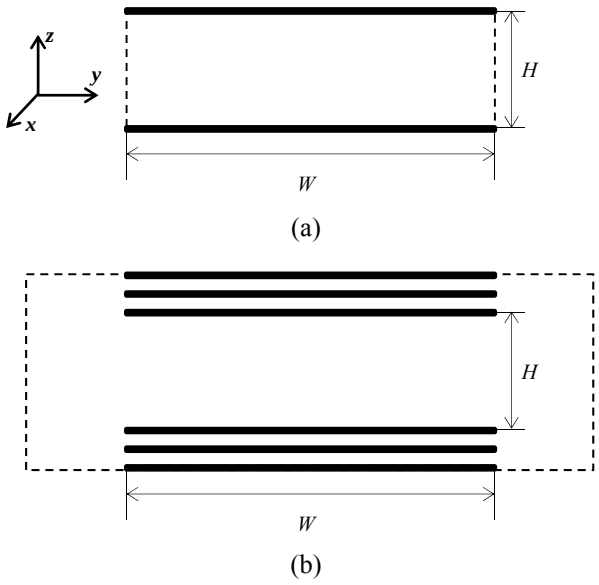

Figure 2.3 Schematic diagram of the slit pore model of (a) infinite length and (b) finite length.

Chapter 3. Adsorption on Graphite Surfaces

3.1. Introduction

Krypton at 77 K (well below its bulk triple point of 115.8 K) is the adsorbate of choice for measuring the surface area of low surface area solids [234]. At this temperature, the adsorption isotherm on homogeneous graphite surfaces is stepped, clearly indicating that adsorption proceeds by a layering mechanism, and for these reasons the system has attracted much attention both experimentally and theoretically [43, 44, 47, 50, 57, 72, 235-242]. The step-wise isotherm for Kr adsorption on the highly graphitized carbon black P-33 at 70 K, associated with the two-dimensional (*2D*) phase transitions occurring in both the first and second layers, was first reported by Clark [240]. Subsequently these transitions were observed experimentally by many other researchers. In addition to the layer-by-layer character of the krypton isotherm on a homogeneous graphite surface, small sub-steps are observed in the first layer, suggesting some ordering of the adsorbed molecules [47, 235, 236]. Simulations below the triple point have provided better insight into these various *2D* transitions at the molecular level [80-82, 99, 241, 242]. However, little attention has been paid to the origin of the experimentally observed hysteresis associated with the *2D* transitions [64, 78].

In this chapter, we studied the *2D*-transitions in open and closed krypton-graphite systems, and the connection between them, using a variety of simulation tools, including: Grand Canonical Monte Carlo (*GCMC*), Canonical kinetic Monte Carlo (*C-kMC*) and the Mid-Density Scheme (*MDS*), to shed light on the adsorption behaviour and phase transitions during gas adsorption on a highly homogenous surface as well as the hysteresis phenomenon in the adsorption-desorption cycle that has rarely been studied.

3.2. Simulation Details

GCMC Simulation

GCMC was used to simulate adsorption isotherms in open systems. 100,000 cycles were run for both the equilibrium and sampling stages. In each cycle, 1000 moves were attempted for displacement, insertion and deletion with equal probability, for each pressure point, giving a Markov chain of 2×10^8 configurations, which is much

longer than commonly used in the literature to ensure the reliability of the simulation results. The algorithm is assumed to be ergodic. To show that we have used sufficient number of cycles, the plots of the instant number of particles as a function of number of cycles are shown in the Appendix 1. To generate the adsorption branch of the isotherm, we started from zero pressure and an empty box, and the first point on the isotherm, corresponding to the lowest pressure, is simulated. The final configuration of one pressure point is used as the initial configuration for the next pressure point, tracing the isotherm. This has been the widely accepted methodology in the scientific community to generate adsorption isotherms with a Monte Carlo scheme because it mimics exactly the same way of how an actual experiment is carried out. In the equilibrium stage, the maximum displacement step length in each direction was initially set as half the dimension of the simulation box in that direction, and was adjusted at the end of each cycle to give an acceptance ratio of 20%. The lengths of the simulation box in the *x*- and *y*-directions parallel to the graphite surface were 20 times the collision diameter of Kr (0.3685 nm), and the dimension in the z-direction was 5 nm. The graphite surface is positioned at z = 0 and the opposite surface is a hard wall. The box size in the *z*-direction was large enough to prevent any spurious correlations in the temperature range studied. Periodic boundaries were applied in the *x*- and *y*-directions.

kMC Simulation

kMC simulation in the canonical ensemble (*C-kMC*) was used to obtain adsorption isotherms in closed systems. When the *GCMC*-isotherms show hysteresis, the *C-kMC* isotherms exhibit a van der Waals-type loop, which is not necessarily S-shaped, and may contain a vertical segment in the unstable portion of the loop.

The number of configurations in *kMC* simulation was 5×10^7 for both the equilibrium and sampling stages. The generation of a configuration involves only one type of move: a particle is selected according to the Rosenbluth algorithm and moved to a random position in the simulation box. The dimensions of the simulation box in the *x*- and *y*-directions were 10 and 40 times the collision diameter of Kr, respectively, and the size in the *z*-direction was 20 nm. We chose a rectangular surface because the coexistence of two phases is more readily achieved. The box size in the *z*-direction is much larger compared to that in *GCMC* simulations because

the rarefied region in the *z*-direction is used to calculate the bulk gas phase pressure by the virial method.

Mid-Density Scheme (MDS)

MDS was applied to determine the equilibrium phase transition within the hysteresis loop of the *GCMC*-adsorption-desorption isotherm. Full details of the *MDS* procedure can be found in [163, 164], but we summarise it briefly here. At a given chemical potential, say μ*, within the range of the hysteresis loop, the low and high density states on the adsorption and desorption boundaries of the loop are referred to as N_A and N_B, respectively. The *MDS* scheme involves three steps:

(1) A state with $(N_A + N_B)/2$ molecules is generated by deleting molecules randomly from the high density (N_B) state.

(2) This mid-density state is then relaxed in the canonical ensemble to minimize the Helmholtz free energy by running 200,000 cycles.

(3) The system having the last configuration of the second step is then exposed to an infinite gas surrounding of the same chemical potential μ*, and is allowed to evolve to an equilibrium state.

The *MDS* scheme yields the equilibrium state because there are co-existing phases in the *NVT* stage (step 2), which have the co-existence chemical potential $\mu_{coexistence}$. If μ* is either greater or smaller than $\mu_{coexistence}$ the system will evolve to the high density state or the low density state.

Fluid-Fluid and Solid-Fluid Potentials

The potential energy of interaction was assumed to be pairwise additive. The fluid−fluid interaction energy of Kr was described by the 12-6 Lennard-Jones (*LJ*) equation, with $\sigma_{ff} = 0.3685\,\text{nm}$ and $\varepsilon_{ff}/k_B = 164.4\,\text{K}$ [243], and the cut-off radius was taken as five times the collision diameter of Kr. The graphite surface was modelled either as a smooth structureless solid or as a surface of discrete carbon atoms. For the structureless surface, the solid-fluid interaction energy was described by the Steele 10-4-3 equation, with a surface carbon atom density of 38.2 nm^{-2}, and molecular parameters for a carbon atom in a graphene layer, $\sigma_{ss} = 0.34\,\text{nm}$ and

$\varepsilon_{ff}/k_B = 28\,\mathrm{K}$. The cross collision diameter and the well-depth of the solid-fluid interaction were calculated by the Lorentz-Berthelot mixing rule. When graphite was modelled as discrete carbon atoms, the interaction energy between a carbon atom and Kr was described by the 12-6 Lennard-Jones (*LJ*) equation.

3.3. Results and Discussions

3.3.1. Krypton Adsorption on Graphite Surface at 77 K

We first carried out *GCMC* simulations for Kr adsorption on the two models of graphite detailed in section 3.2. The simulated isotherms at 77 K are shown in Figure 3.1. The structureless model cannot account for the incommensurate to commensurate transitions that have received much attention in the past, especially for very low temperature systems [235, 244]. However, the figure shows that the structureless surface model captures all the major features of interest, including the *2D*-transition and the sub-steps. Hereafter, we shall use the structureless model to minimise the computation time needed to achieve a satisfactory description of the isotherm, and especially of the isosteric heat.

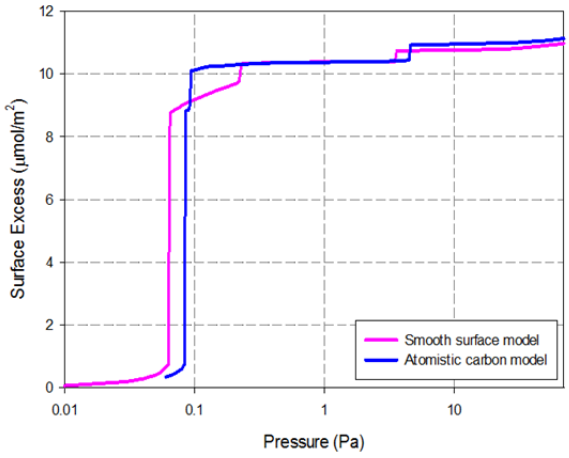

Figure 3.1 The *GCMC* simulated adsorption isotherm at 77 K for Kr on a graphite surface: Smooth surface model and the atomistic carbon model.

Figure 3.2 shows that there is qualitatively good agreement between the *GCMC*-adsorption isotherm for Kr on graphite at 77 K and the experimental data of Thomy and Duval [45].

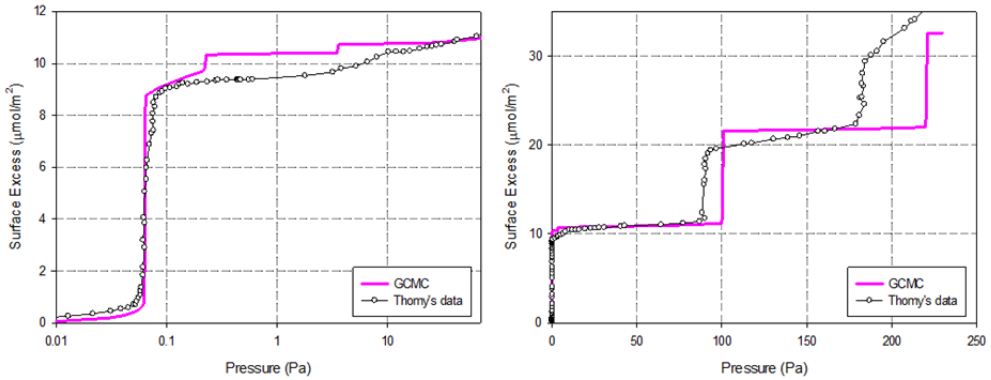

Figure 3.2 *GCMC* simulated adsorption isotherm at 77 K for Kr on a smooth graphite surface and experimental data on ex-foliated graphite from reference [45], (a) logarithm scale showing the *2D*-transition of the first layer, (b) linear scale showing the *2D*-transition of the second and third layers.

The general step-wise behaviour in the first three layers of the experimental isotherm is reproduced by the simulations. The experimental isotherm rises gradually after the first condensation in the first layer, but the simulation results show two vertical steps, representing the liquid-solid transition followed by a molecular rearrangement to a more ordered *2D*-solid. The gradual rise in the experimental sub-step may be due to geometrical factors not accounted for in the molecular model, such as the finite size of the graphene basal plane on a polyhedral side of the graphitized thermal carbon black. This may also be the reason why the pressures at which the transitions occur in the second and third layers differ from those in the simulation.

Figures 3.3 and 3.4 show the *2D* radial distributions and the *2D* density contour plots respectively, for the first layer, at the points A-E marked on the isotherm. At A, just before the *2D*-transition, the first layer is gas-like characterized by a single peak in the radial distribution, and changes to a liquid-like structure at B, just after the *2D*-condensation. This liquid-like structure is seen in the disordered *2D*-density plot in Figure 3.4b. The first sub-step, CD, corresponds to the transition from a liquid-like to a solid-like state, and as seen by the evolution of the second peak in the radial density distribution into two sub-peaks, signifying a hexagonal solid structure, as confirmed by the *2D*-density plots in Figures 3.4c and d. When the pressure is increased to Point E (the second sub-step), there is a further densification of the first layer, as seen in Figure 3.4e, where the molecules are localised into a *2D* hexagonal crystalline packing.

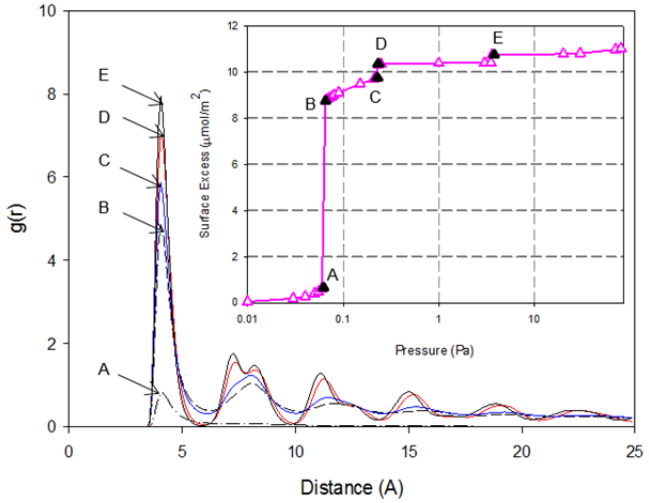

Figure 3.3 Radial distribution of Kr adsorption on graphite surface at 77 K.

3.3.2. Effects of Temperature on the 2D Transitions

The effects of temperature on the *2D*-transitions and sub-steps in the first layer are illustrated in Figure 3.5, which shows isotherms at temperatures from 60 to 88 K.

At 60 K (well below the triple point), there is a *2D*-transition from a gas-like to a solid-like state in the first layer, followed by a single sub-step which corresponds to the transition from a disordered solid-like state to an ordered one. This interpretation is substantiated by plots of the radial density distribution in Figure 3.6 at: (1) point A, the gas-like state just before the *2D*-condensation; (2) point B, just after the condensation; and (3) point C, just after the completion of the sub-step. The double second peaks at points B and C just after the *2D*-transition correspond to regular third neighbour locations and are characteristic of a solid-like structure of the adsorbate.

At temperatures greater than 73 K (Figure 3.5) there is a *2D* gas-liquid transition, and two sub-steps, corresponding to a liquid to disordered-solid transition and disordered to ordered-solid transition as seen in the 73 K radial distribution plots in Figure 3.7. It is interesting to note that the adsorbate densities for the disordered and ordered solids do not vary with temperature (see the two dashed lines in Figure 3.5a). From this family of isotherms at different temperatures, we can deduce a critical temperature for the *2D* gas-liquid transition in the first layer between 86 and 88 K (Figure 3.5b), which agrees closely with the value of 86 K reported experimentally

[50]. The 2D liquid to disordered-solid transition is first order and becomes less observed with the increase of temperature from 73 to 86 K due to the thermal motion of argon molecules, and changes continuously at 88 K as the isotherm in the monolayer region is supercritical.

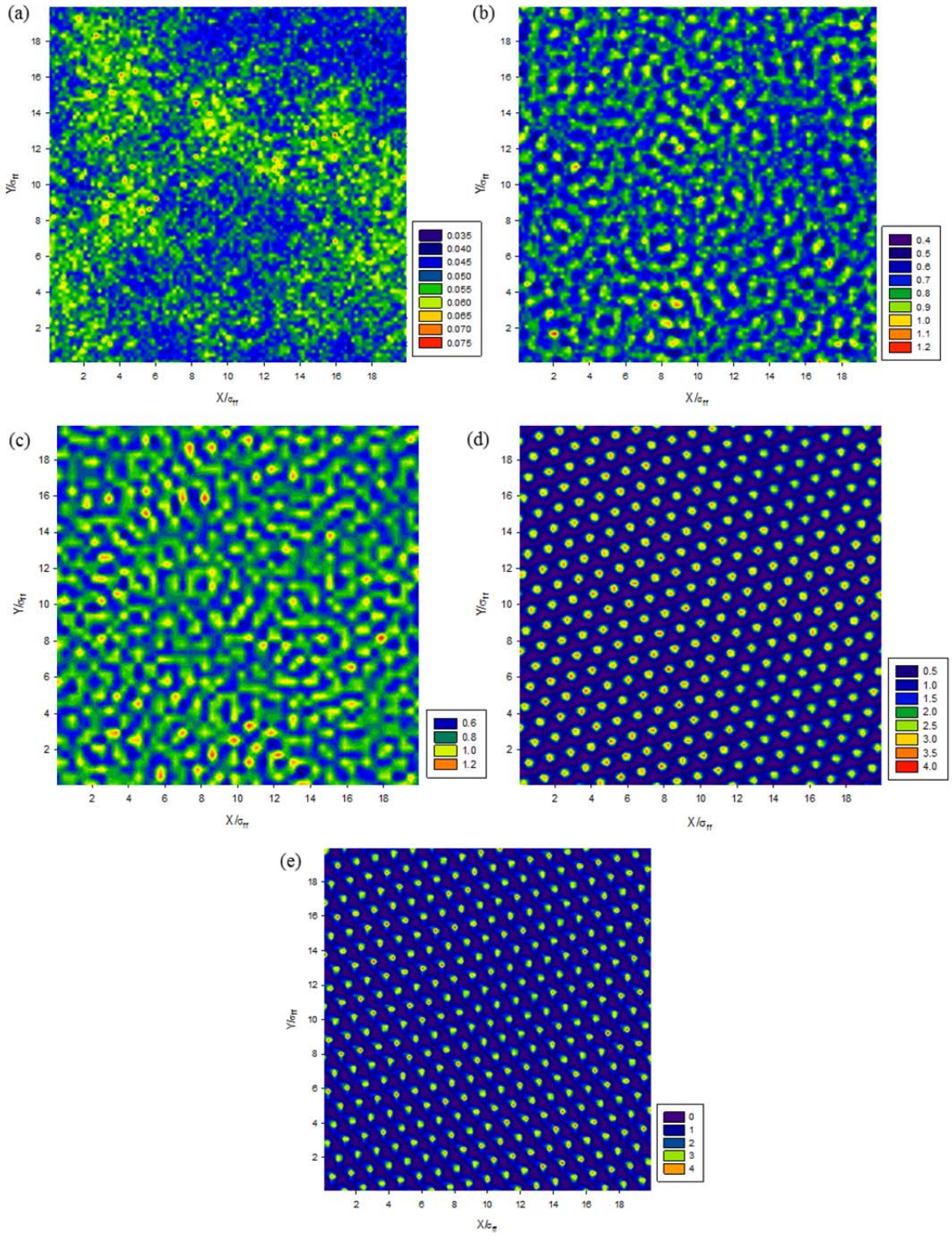

Figure 3.4 *2D*-Density Distribution of Kr adsorption on graphite surface at 77 K, (a) – (e) corresponding to points marked as A, B, C, D, E in the inset of Figure 3.3, respectively.

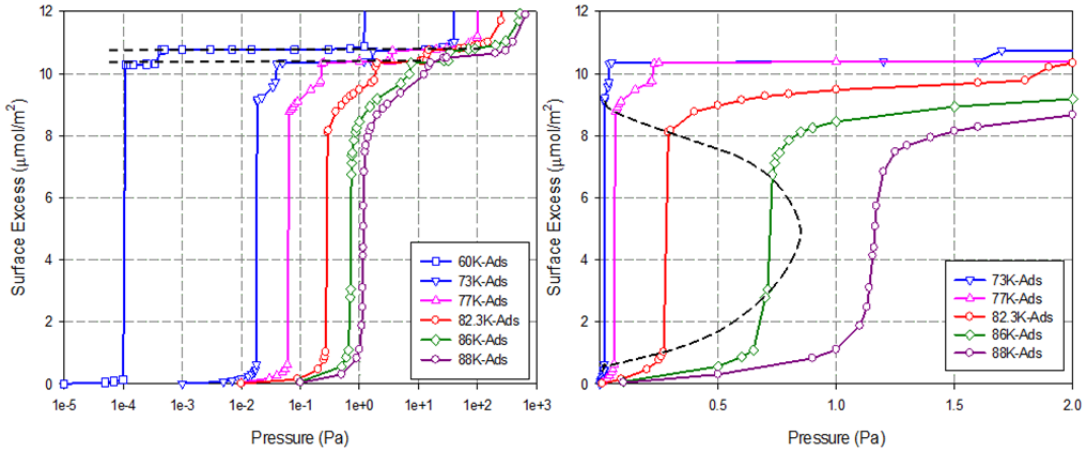

(a) (b)

Figure 3.5 *GCMC* adsorption isotherms for Kr on a graphite surface at 60-88 K: (a) logarithm scale, (b) linear scale.

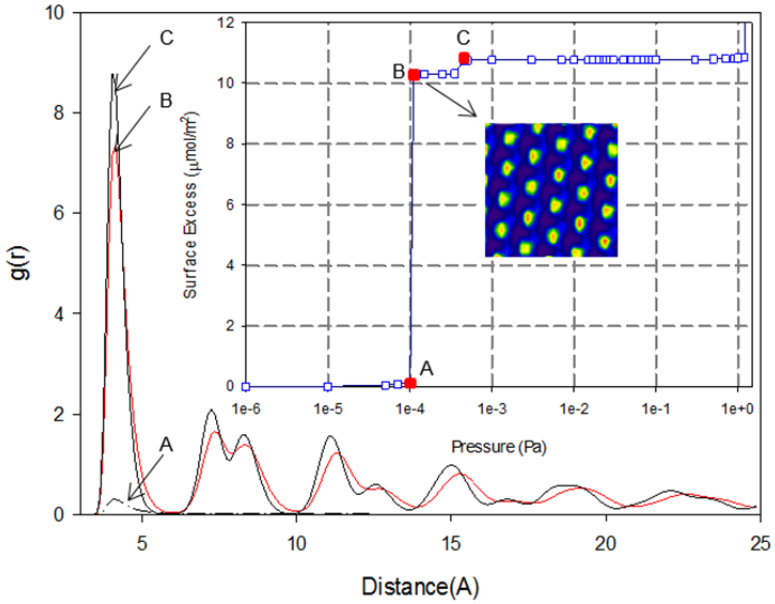

Figure 3.6 Radial distributions for Kr adsorption on a graphite surface at 60 K.

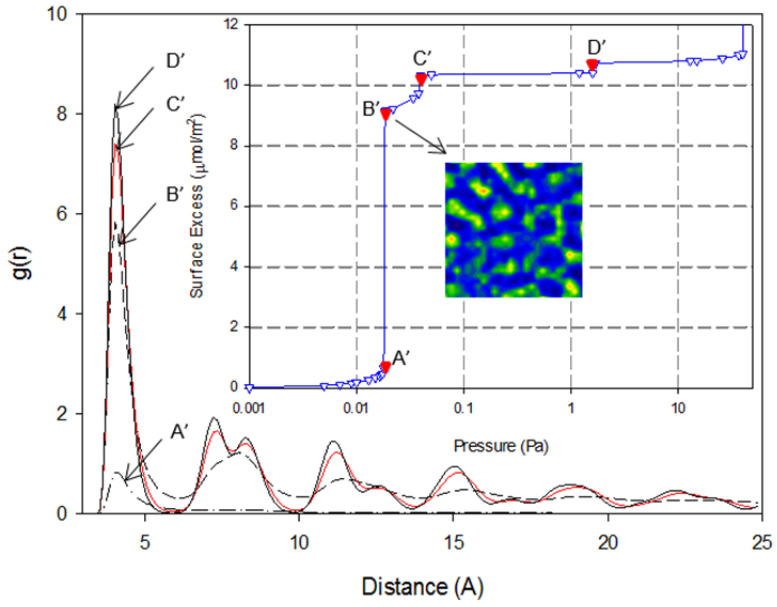

Figure 3.7 Radial distributions for Kr adsorption on a graphite surface at 73 K.

To probe the energetic behaviour of adsorption, we plot the isosteric heat versus loading for 60 and 77 K in Figure 3.8. These temperatures were chosen to show the *2D* transitions from the gas-like state to the solid state (60 K) and from the gas-like state to a liquid-like state. The isosteric heat increases linearly with loading up to the *2D*-transition, becomes constant across the transition, and then increases approximately linearly after the first transition. At 60 K, after the gas-solid transition but before the sub-step, the isosteric heat decreases because adsorption begins in the second layer. However, there is a spike in the heat curve at the sub-step, due to the squeezing of molecules into the disordered solid layer which is transformed into an ordered hexagonally packed array (an enlargement of the heat curve in the region of the monolayer is shown in the inset of Figure 3.8). This phenomenon has been extensively studied [83, 84]; the spike is due to two factors: (1) the lowering of the solid-fluid and fluid-fluid energy as the incoming molecules pack into the partially completed first layer, and (2) the simultaneous rearrangement of the molecules already in the first layer, to form a close packed hexagonal configuration. The heat spike phenomenon is not restricted to the first layer, but has also been observed experimentally in higher layers [63]. At 77 K, differs slightly after the first transition. The heat increases because of the compression of the liquid-like layer to point A (Figure 3.8) and then to disordered solid-like layer (Point B). No spike is observed at the first sub-step because molecules continually adsorb into the first layer forming a

disordered solid. After the first sub-step the layer is relatively dense, and adsorption begins in the second layer, resulting in a sharp decrease in the heat. When the chemical potential is further increased a heat spike occurs due to molecules squeezing into the first layer, to give an ordered hexagonal packing at the second sub-step in the isotherm (see Figure 3.5).

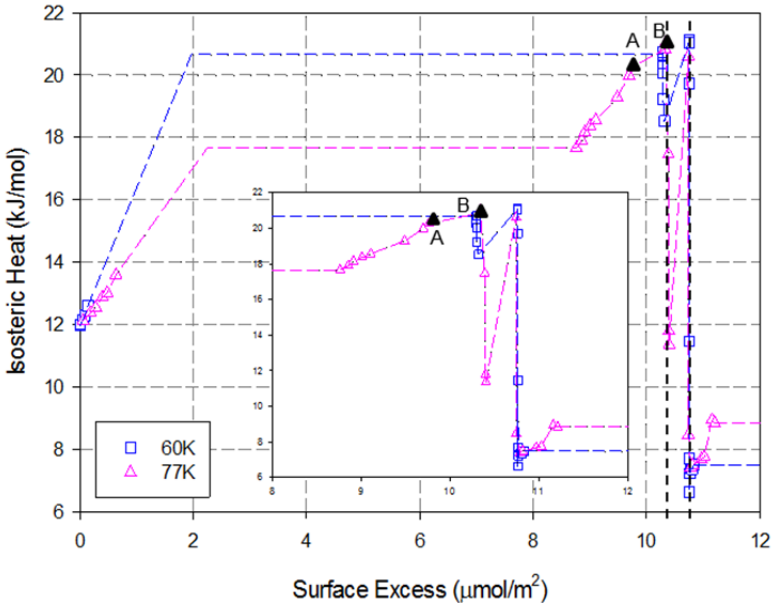

Figure 3.8 The isosteric heat of Kr adsorption on graphite surface at 60 and 77 K obtained with GCMC simulation.

3.3.3. Hysteresis at Temperatures 73-91.8 K

Conventional wisdom associates adsorption-desorption hysteresis with pores in the mesopore size range. However, a number of experimental papers [64, 78], including one for Kr adsorption on exfoliated graphite have reported hysteresis in low pressure transitions [78].

Figures 3.9a and b show the *GCMC*-adsorption and desorption isotherms at 77 K. Several interesting points arise:

1. *2D*-condensation and evaporation, with well-defined hysteresis, occurs in the first three layers.
2. There is also hysteresis at the sub-steps, which suggests that hysteresis is an intrinsic feature of any first order adsorption-desorption transition.

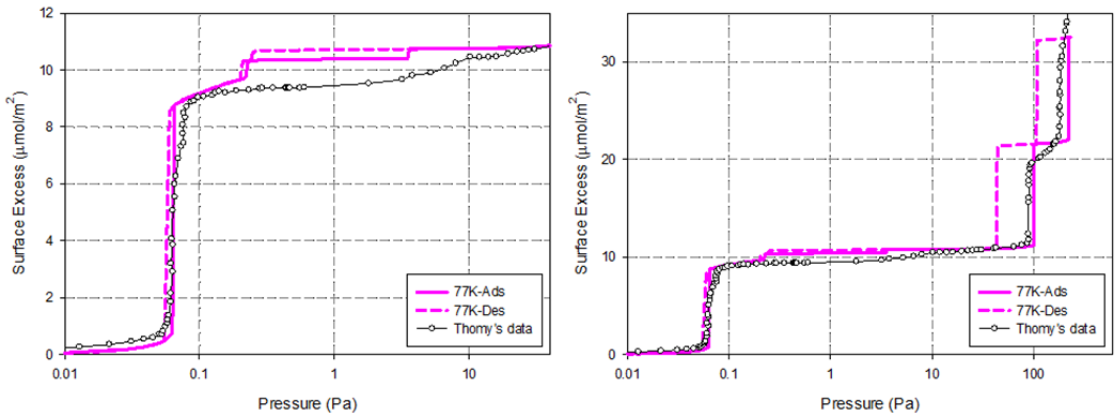

(a) (b)

Figure 3.9 The adsorption isotherm of Kr on graphite surface at 77 K obtained with *GCMC*, (a) first layer, logarithm scale, (b) first to third layer, logarithm scale.

We argue that it follows from this that the microscopic reason for the hysteresis lies in the restructuring and progressive cohesiveness of the adsorbate as loading increases. As evidence, we have plotted in Figure 3.10 the local compressibility of the first adsorbed layer at 77 K from zero loading up to three adsorbed layers on the surface, with the position of the *2D*-transitions in the first three layers marked as I, II, III. There is a sharp drop in the compressibility in the first layer at the first *2D*-condensation (I). After the *2D* liquid-solid transition (from A to B), the compressibility reaches that of solid Kr (5.6×10^{-10} Pa^{-1} shown as a black dashed line) [245]. The compressibility of the first layer continue to decrease even when there is adsorption in higher layers, implying that the cohesiveness in the first layer continues to increase towards a meta-stable state of lower energy. Therefore when the pressure is reduced during desorption the adsorbate does not evaporate until the pressure is lower than the condensation pressure, and a hysteresis loop is formed.

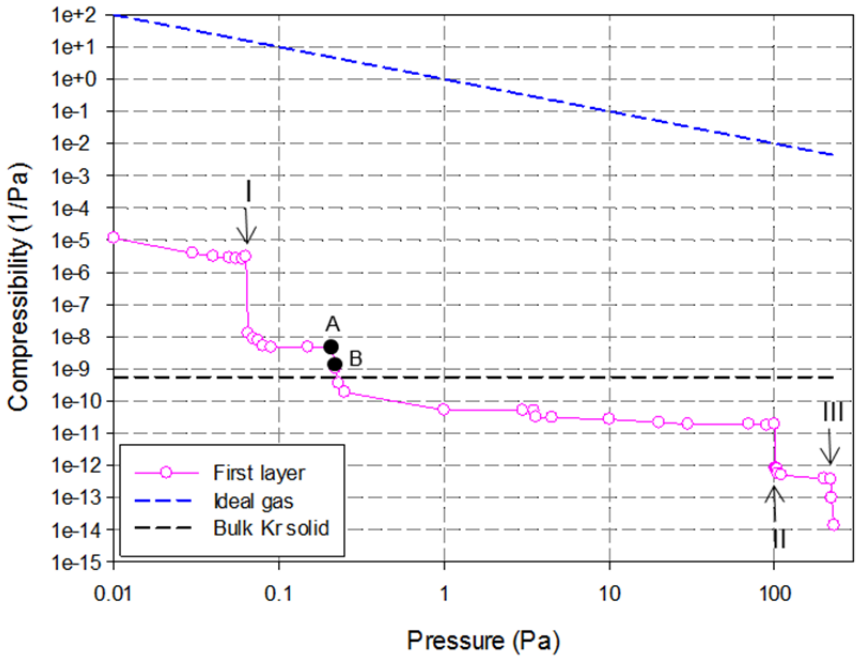

Figure 3.10 Layer compressibility in the first layer during Kr adsorption on graphite at 77 K obtained from GCMC simulation.

The effects of temperature on the size and position of the hysteresis loop are shown in Figure 3.11 for temperatures in the range between 73 and 91.8 K. The hysteresis loop for the first layer, becomes smaller as temperature is increased, and disappears at 82.3 K, indicating that the critical hysteresis temperature is between 77 and 82.3 K. For the second layer, the hysteresis loop is present for all the temperatures investigated here, suggesting that the hysteresis critical temperature of the second layer is greater than 91.8 K. However, at 91.8 K there is no hysteresis in the third layer, i.e., the *2D*-critical temperature and the hysteresis critical temperature of the third layer are between 88 and 91.8 K, in agreement with the simulation results obtained by Nguyen *et al*. [241]; i.e. the *2D*-critical temperature of the third layer is between those of the first and second layers.

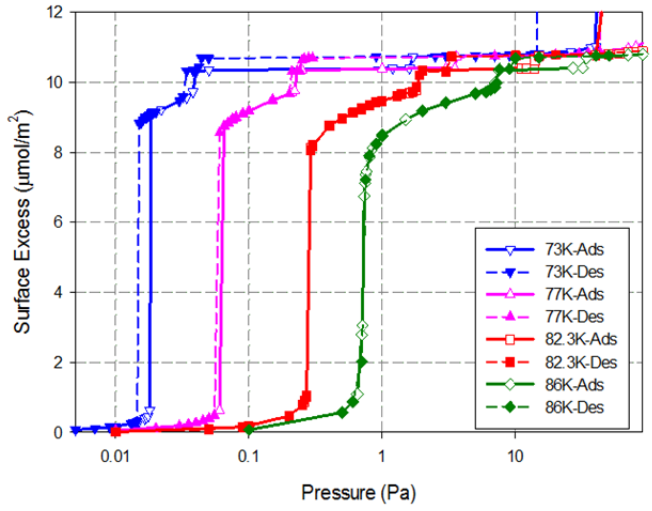

(a)

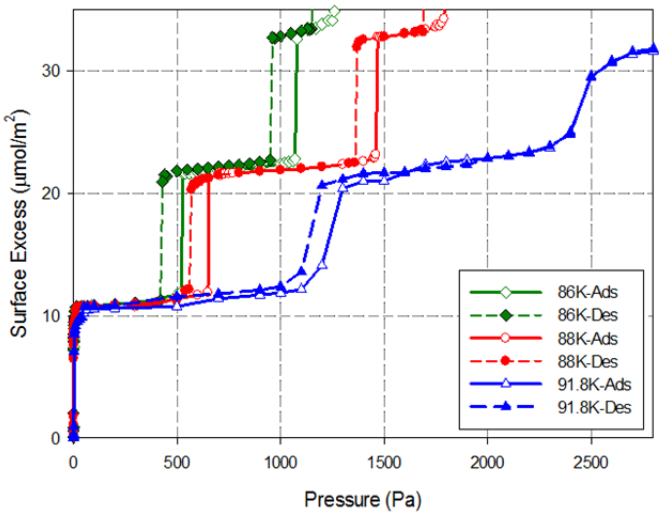

(b)

Figure 3.11 The adsorption isotherm of Kr on a graphite surface at (a) 73-86 K, logarithm scale and (b) 86-91.8K, linear scale obtained with *GCMC*.

The two sub-steps of the first layer for the isotherms at 73-86 K are shown in Figure 3.11a. The *2D* ordered solid persists over a very wide range of pressure and only evaporates at a pressure that is lower, by two orders of magnitude, than the pressure of the ordering transition during adsorption. This is further evidence that the ordered solid is in a highly cohesive low energy state. When the pressure is decreased further, the *2D*-disordered solid melts to a *2D* liquid-like phase, and finally evaporates to a gas-like state. This means that both the disordered solid and the *2D* liquid are in more cohesive, lower energy states. The hysteresis loop in the first sub-step of the liquid-disordered solid transition shrinks with temperature and disappears at 82.3 K,

while the second loop, associated with the rearrangement of adsorbate to form an ordered *2D* solid, persists at all the temperatures studied here, indicating that the *2D*-crystalline solid is very stable.

The hysteresis described above is associated with the first order transition in an open system (grand canonical), and the transition occurs at a pressure close to the spinodal point (its proximity depends on the temperature). To understand how a closed system evolves and how it is distributed between the two phases, we carried out simulations in the canonical ensemble to locate the spinodals and to determine how far the transition is from the spinodal point. We then applied the Mid-Density scheme (*MDS*) first proposed by Liu *et al*. [163, 164] to determine the pressure at the equilibrium transition.

Figure 3.12 shows the canonical (*C*)-isotherm at 73 K obtained with the kinetic Monte Carlo scheme and the *GCMC* adsorption-desorption isotherm. Since the *GCMC* isotherm shows transitions on both branches, the corresponding canonical isotherm has a van der Waals type of loop with a vertical segment in the unstable region. This type of loop is a clear indication of the co-existence of two phases. The equilibrium transition, determined by the *MDS* shows the overlap between this transition and the vertical segment of the *C*-isotherm. Interestingly, but not surprisingly, the *2D*-coexistence of two phases is not restricted to the first layer, but is also present in higher layers. In open systems, the transition always occurs before the spinodal point has been reached because of thermal fluctuations; as noted in earlier publications [82, 162, 246].

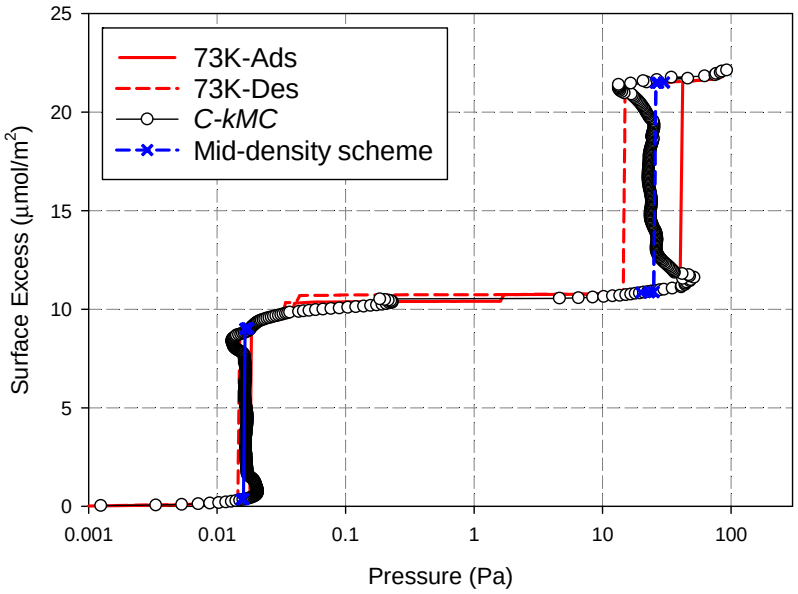

Figure 3.12 The adsorption isotherms of Kr on a graphite surface at 73 K: comparison between the results of *GCMC* and *kMC* simulations; and the equilibrium phase transition obtained by the Mid-Density scheme (*MDS*). The surface was a surface of $10\sigma_{ff} \times 40\sigma_{ff}$ rectangle.

3.4. Conclusions

In this chapter we have used *GCMC*, *C-kMC* and Mid Density scheme simulations to study the *2D* transitions and hysteresis of Kr adsorption on a structureless graphite surface at temperatures below the triple point. *2D* phase transitions (gas-solid, gas-liquid and liquid-solid, disordered-ordered solid) are observed at temperatures less than the *2D* critical temperature. Hysteresis was found to occur in every layer at temperatures less than the corresponding 2D hysteresis critical temperature. The existence of hysteresis was confirmed by the presence of van der Waals loops in the canonical isotherm. This loop contains a vertical segment, which indicates the coexistence of two phases in the system, a conclusion that is supported by the location of the equilibrium transition, as determined with the Mid Density scheme. As the adsorption hysteresis on graphite has been observed experimentally for other gases, such as xenon, methane, chloroform, acetone and ammonia, the mechanism of the hysteresis might be influenced by gas species, which is worth further study.

Chapter 4. Adsorption in Graphitic Slit Micropores

4.1. Introduction

In Chapter 3, we have studied the two-dimensional (*2D*) transitions in the adsorption of gas on graphite. The various *2D* transitions that can occur include *2D* gas-solid and *2D* gas-liquid transitions followed by *2D* liquid-solid transitions at temperatures below the *2D* critical temperature, $T_{c,2D}$. Above this temperature, a *2D*-hypercritical fluid-solid transition is possible if the temperature is not far from $T_{c,2D}$. The *2D* liquid-solid and *2D* hypercritical fluid-solid transitions can be viewed as *2D* ordering transitions, which may be identified by a spike in the curve of isosteric heat versus loading. This ordering transition has also been reported for adsorption in nanopores, and is related to the freezing/melting phenomena in confined fluids [11, 97]. In this chapter we extend our study to graphitic slit micropores to investigate the adsorption and phase behaviours of fluids under confinement.

Adsorption-desorption hysteresis is generally observed in isotherms for mesoporous solids at temperatures below the critical hysteresis temperature. The origin of this hysteresis is usually attributed to the different mechanisms of adsorption and desorption [139]. Experimentally observed hysteresis loops are classified into six types [4]. Although there is a large number of studies devoted to the hysteresis phenomena in mesoporous solids, little attention has been paid to pores of molecular dimensions (nanopore), and it is frequently stated that hysteresis does not occur for adsorption in pores in this size range. Nevertheless ordering transitions can occur in such pores accompanied by the formation of solid-like phases even at temperatures above the bulk triple point [80, 91]. Understanding the hysteresis associated with ordering transitions in nanopores would be a further step in helping to unravel the behaviour of adsorbates in confined spaces and should improve the structural characterization of nanoporous solids.

In this chapter we studied the order-disorder transitions and the associated hysteresis, for simple gas adsorption in narrow slit pores with two open ends. Microscopic analysis of the local density distribution, radial density distribution, and local compressibility have been made as an aid to gaining greater insight into the mechanisms involved in these processes as a function of pore size and temperature.

4.2. Simulation Details

Potential Models

The intermolecular potential energy for argon was described by the 12-6 Lennard-Jones (*LJ*) equation, with $\sigma_{ff} = 0.3405$ nm and $\varepsilon_{ff}/k_B = 119.8$ K [243].

For pores of infinite length in the *x*- and *y*-directions, we applied periodic boundary conditions and the solid-fluid potential energy was calculated with the Steele 10-4-3 equation. For the finite slit pores the pore walls were composed of three homogeneous graphene layers, finite in the *y*-direction and infinite in the *x*-direction. The solid-fluid potential energy was calculated from the Bojan-Steele equation. The molecular parameters for a carbon atom in the graphene layer are $\sigma_{ss} = 0.34$ nm and $\varepsilon_{ss}/k_B = 28$ K, and the carbon density of a graphene layer is 38.2 nm^{-2}. The cross collision diameter and the well-depth of the solid-fluid interaction energy were calculated from the Lorentz−Berthelot mixing rule.

Monte Carlo Simulation

Grand Canonical Monte Carlo (*GCMC*) simulation was used to simulate the adsorption isotherms with 100,000 cycles for both the equilibrium and sampling stages. For pores of infinite length, the dimensions of the simulation box in the *x*- and *y*-directions were 20 times the collision diameter of the adsorbate and the dimension in the *z*-direction was the same as the pore width. For a finite pore, the dimension of the simulation box in the *y*-direction was set as 10 times the collision diameter of the adsorbate, and the dimensions of the other two directions were determined by the pore width and length. The pore was connected to the bulk gas reservoirs of 3nm length at each end in the *x*-direction.

To obtain the radial density distributions of bulk liquid and solid argon, Canonical Monte Carlo (*CMC*) simulation was conducted with periodic boundary conditions imposed on all boundaries. For bulk solid argon, the initial configuration consisted of 2352 particles arranged on a Face Centred Cubic (*fcc*) lattice within the box of dimensions 3.81nm × 6.54nm × 3.81nm at 50 K. To simulate bulk liquid argon at 87K, 834 particles were placed on a simple cubic lattice within the box of dimensions 3.41nm × 3.41nm × 3.41 nm as the initial configuration giving a liquid

phase density equal to the experimental value [247]. 100,000 cycles were used in the *CMC* for the system to reach equilibrium before the radial density distribution was collected. The radial density distributions (*RDD*) of bulk liquid and solid argon are shown in Figure 4.1. The *RDD* of the bulk solid shows distinct structuring at large atom separations and minor peaks between major ones separated by approximately one collision diameter corresponding to neighbour distances with lower populations. These minor peaks are absent in the *RDD* of the bulk liquid.

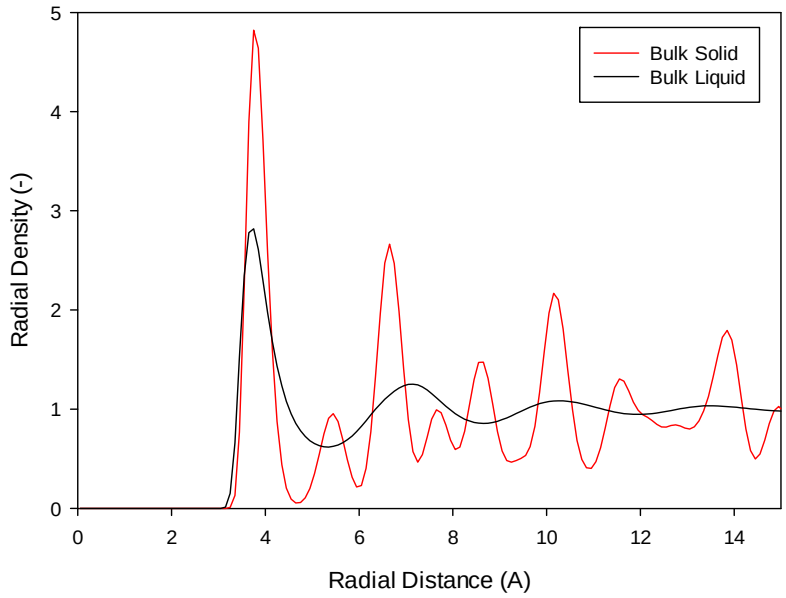

Figure 4.1 The radial density distributions of bulk liquid argon at 87 K and solid argon at 50 K.

4.3. Results and Discussions

4.3.1. Adsorption of Argon in an Infinite Pore at 87 K

Figure 4.2 shows the adsorption isotherm and the local density distributions of adsorbed argon at 87 K in an infinitely long pore of width 1.5 nm. The adsorption proceeds via the usual molecular layering mechanism, typical for simple molecules at subcritical temperatures, followed by a first order transition after the completion of approximately two layers. There is also a steep first order transition in the desorption branch, typical of cavitation in pores of infinite extent where evaporation cannot take place from a gas-adsorbate interface. The local density distributions in Figure 4.2b show that adsorption in this 1.5nm pore shows progressive build-up to four layers of molecules, followed by a sharp transition in these layers, especially in the two inner

layers. This leads to a compression of the adsorbate, evidenced by the transformation of the overlapping inner peaks into two distinct peaks. Upon desorption, this highly cohesive structure remains stable, as shown by the plateau of the desorption-branch, until the cavitation pressure has been reached. Note that the pore density just after cavitation is less than that just prior to the ordering transition.

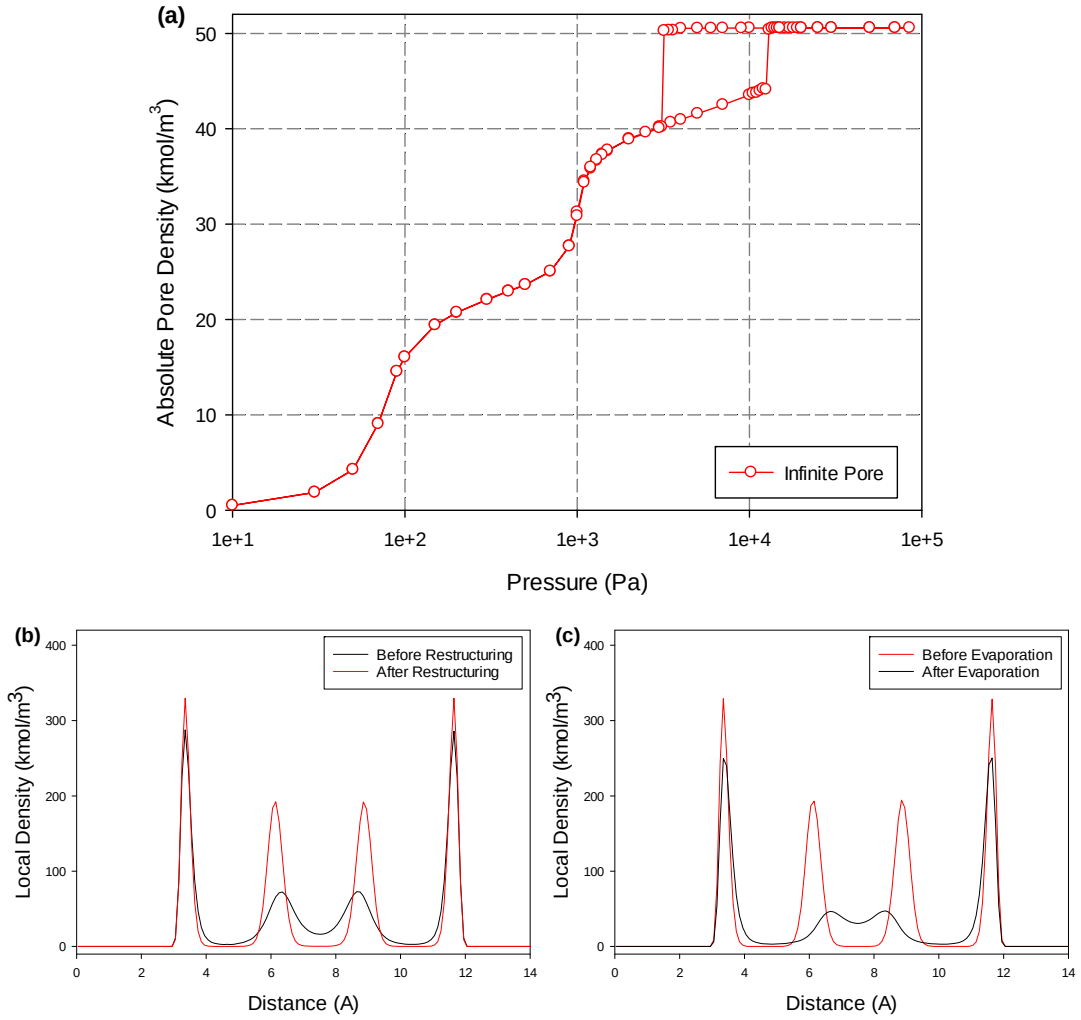

Figure 4.2 (a) The adsorption isotherm of argon at 87 K in an infinitely long pore of width 1.5 nm; the local density distributions in the pore (b) before and after the first-order transition in the adsorption branch, and (c) before and after the first-order transition in the desorption branch.

To obtain insight at a microscopic level into the adsorbate structure across the first order transition along the adsorption branch, we show, in Figures 4.3a and b, the radial density distributions (*RDD*) of the contact and inner layers, respectively together with the *RDD* of bulk liquid and solid argon. Just before the transition the *RDD* of the contact layer is similar to that of bulk liquid argon while the inner layer

resembles a compressed gas. After the transition both the contact and the inner layers become solid-like. Thus the first order transition along the adsorption branch is due to (1) a liquid-solid transition in the contact layer and (2) a compressed gas to solid transition in the inner layer. It should be noted that the temperature 87 K is above the bulk triple point 83.78 K and the *RDD* shows that the *2D* solid is square packed, as observed by other researchers [80, 97].

The difference between the first order transitions for desorption and adsorption is the delay in evaporation, due to the metastability of the adsorbate, resulting in a hysteresis. We can characterise this hysteresis as a consequence of both the ordering of the contact layer and of condensation/evaporation of the inner layer. This implies that for pores smaller than 1.5 nm, hysteresis, if it existed, would be due to an ordering process, and for larger pores it would occur by condensation/evaporation, followed by an ordering process. The results in Section 4.3.3 from our simulation of argon adsorption at 60 K demonstrate this latter process.

When an ordering transition occurs in the first layer for adsorption of gases on a homogeneous graphite surface, for example argon and nitrogen at 77 K, a spike is observed in the heat curve versus loading [69, 84], and this raises a question about whether a heat spike is similarly observed in pores across the ordering transition. Figure 4.4 shows the isosteric heat and the contributions from the solid-fluid (*SF*) and fluid-fluid (*FF*) interactions, and we see a steep increase in the heat from points A to B labelled in Figure 4.4 which corresponds to loadings across the ordering transition. This increase is mostly due to the contribution from the fluid-fluid interaction, brought about by the sharp increase in loading of the inner layers. This is distinct from the spike observed in surface adsorption which is due to the combined increase in both the *FF* and *SF* interactions, resulting from the rearrangement of first layer molecules as additional molecules are squeezed into this layer.

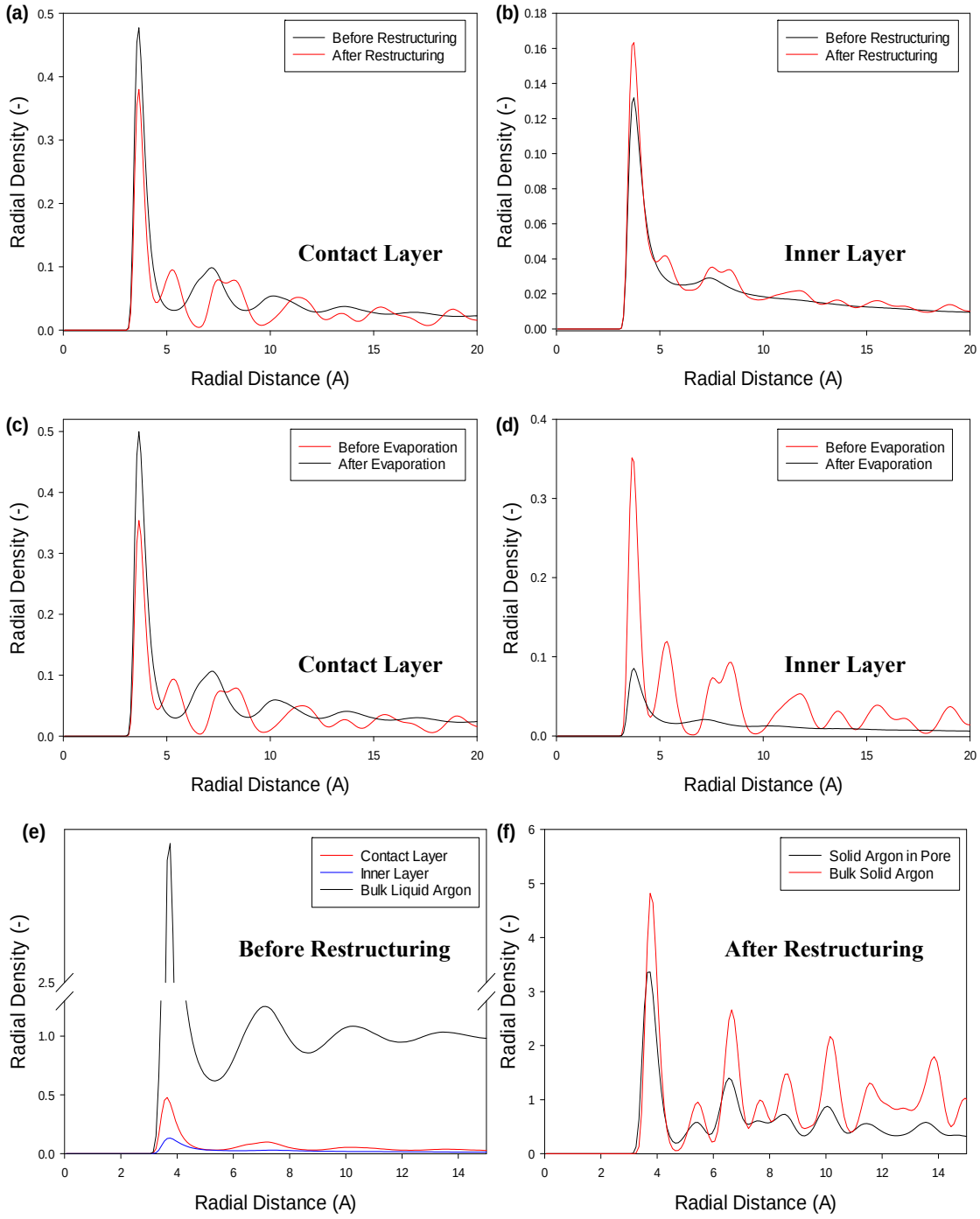

Figure 4.3 The radial density distributions of the infinitely long pore at points before and after the first-order restructuring transition for (a) the contact layers and (b) the inner layers; before and after the first-order evaporation for (c) the contact layers and (d) the inner layers; (e) the contact and inner layers in the pore before restructuring, and bulk liquid argon; (f) the adsorbed solid phase in the pore after restructuring, and bulk solid argon.

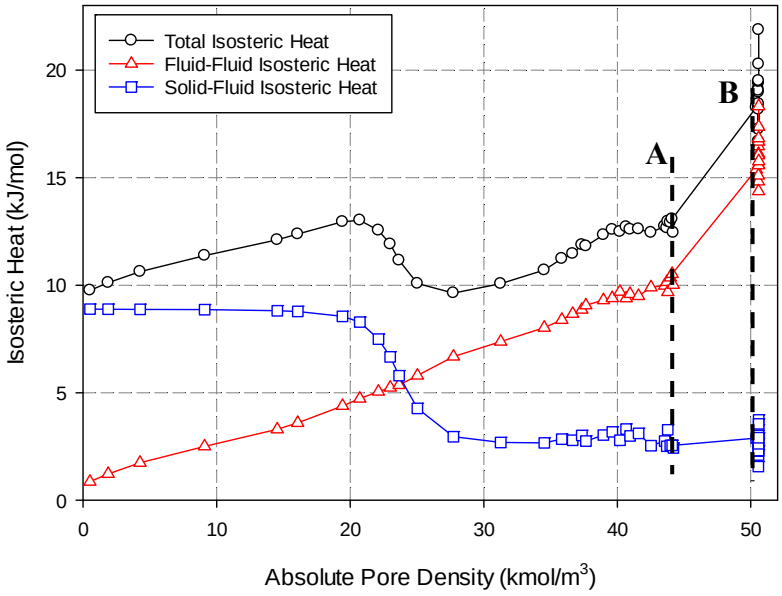

Figure 4.4 The isosteric heat of argon adsorption at 87 K in the infinite pore with pore width 1.5 nm.

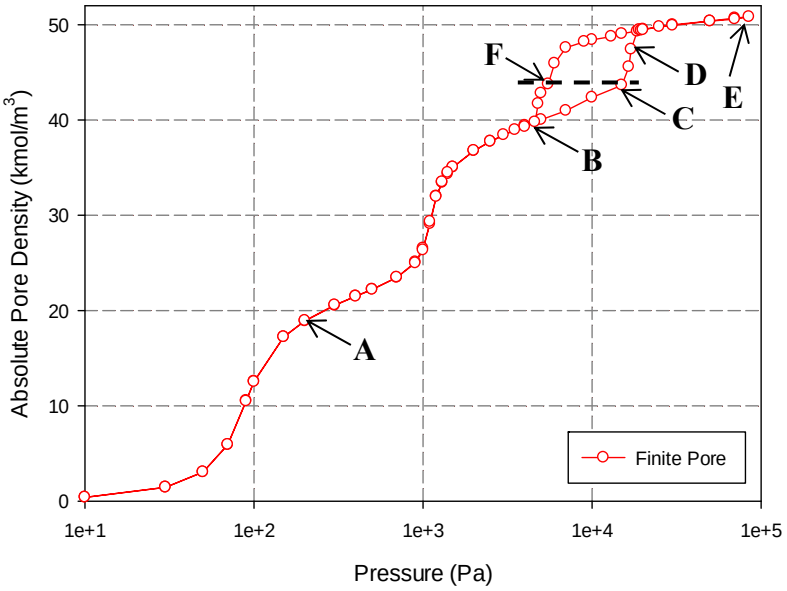

Figure 4.5 The adsorption isotherm of argon at 87 K in a finite pore (pore length 20 nm) with 1.5 nm width.

4.3.2. Adsorption of Argon in a Finite Pore at 87 K

Figure 4.5 shows the adsorption isotherm for argon at 87 K in a finite pore of 1.5 nm width and 20 nm length. It also exhibits hysteresis, but its characteristics are different from those of the infinite length pore; the transition in the hysteresis region

is now second order rather than first order, brought about by the presence of an interface separating the adsorbed and gas phases.

To shed further light on the transition along the adsorption branch we show, in Figure 4.6, the *3D* local density distribution (*LDD*) as a function of distance and pressure for the finite pore and the corresponding pore of infinite length. It is seen that the *3D LDD* of the finite pore show gradual changes in both the contact and inner layers.

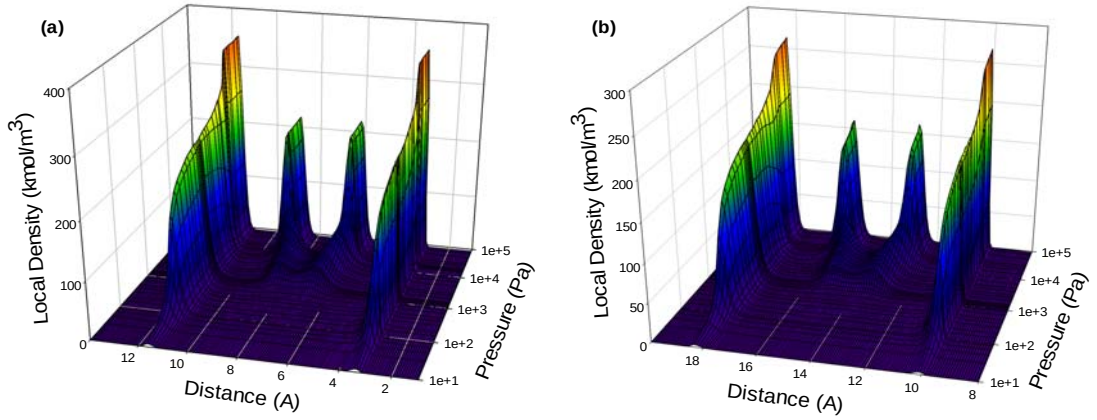

Figure 4.6 The 3D plot of local density as a function of distance and pressure, (a) infinite pore and (b) finite pore both with 1.5 nm pore widths.

Figure 4.7 shows the *RDD* of these layers at Points C, D, E and F marked on the isotherm in Figure 4.5. Points C and D illustrate the evolution of the *RDD* across the transition along the adsorption branch, and Points C and F illustrate the difference in the structure along the adsorption and desorption branches at the same density. The *RDD* at the saturation vapour pressure, Point E, is at the ultimate packing structure.

Point	Contact Layer	Inner Layer
C	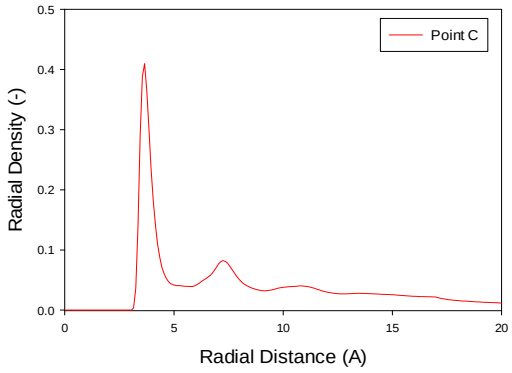	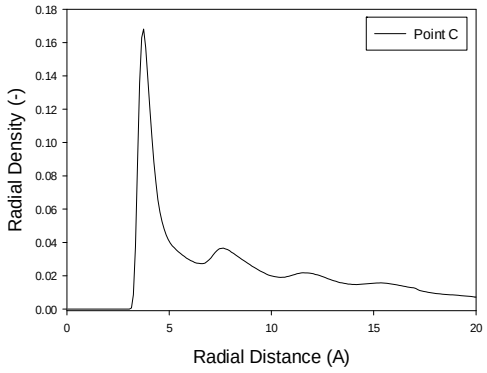
D	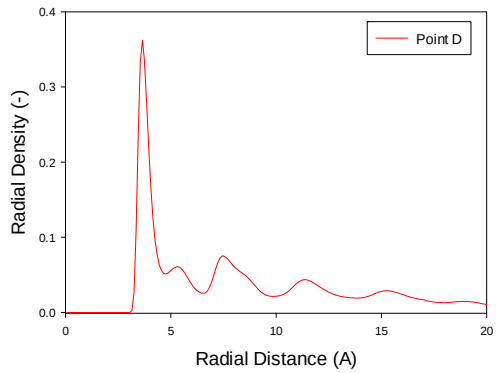	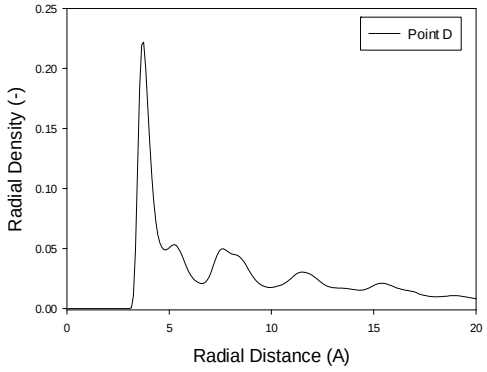
E	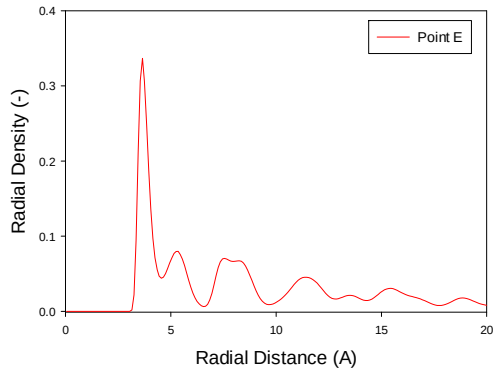	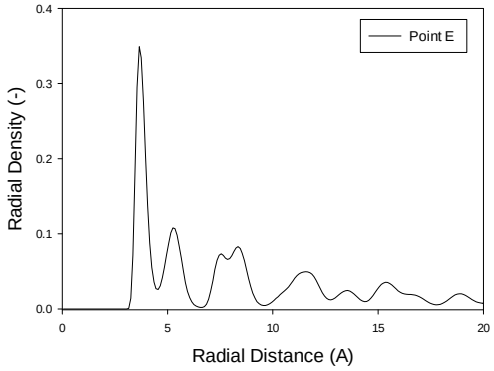
F	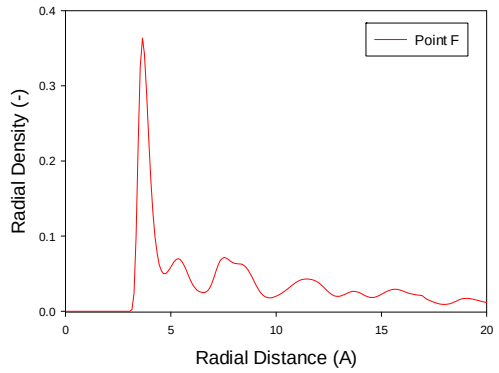	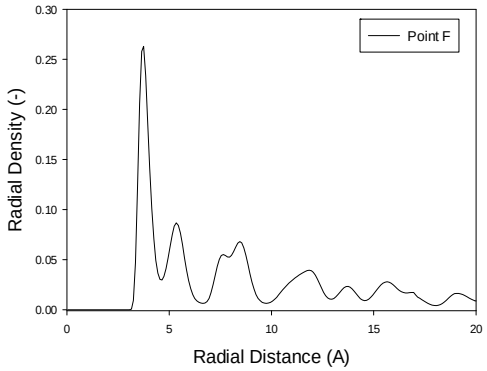

Figure 4.7 The radial density distributions of the finite pore at Points C, D, E, F in Figure 4.5 for the contact and inner layers.

The *RDD*s in Figure 4.7 reveal the following features:

1. The *RDD*s along the adsorption boundary of the ordering hysteresis loop (Points C to D) show that the contact and inner layers evolve from a liquid-like state to a solid-like state, where the first peaks de-convolute into two peaks, and the isotherm shows a gradual increase (Figure 4.5), indicating that this transition is second order. A similar continuous ordering transition has also been reported elsewhere for argon adsorption in slit pores [99].
2. Further increase in loading from Point D to E (saturation pressure) results in a further densification and ordering of all layers.
3. Along the desorption boundary of the hysteresis loop, the cohesiveness of the adsorbate persists to lower pressures, as shown by the solid-like *RDD* at Point F, compared to the liquid-like state at Point C on the adsorption branch at the same density as may be seen by comparing with the *RDD*s for bulk liquid and solid argon (see Figures 4.8a and b). Although the position and relative magnitudes of the peaks are very similar, the absolute intensities are greater in the bulk phase because the number of neighbours (especially distant neighbours) is greater in the bulk phases.

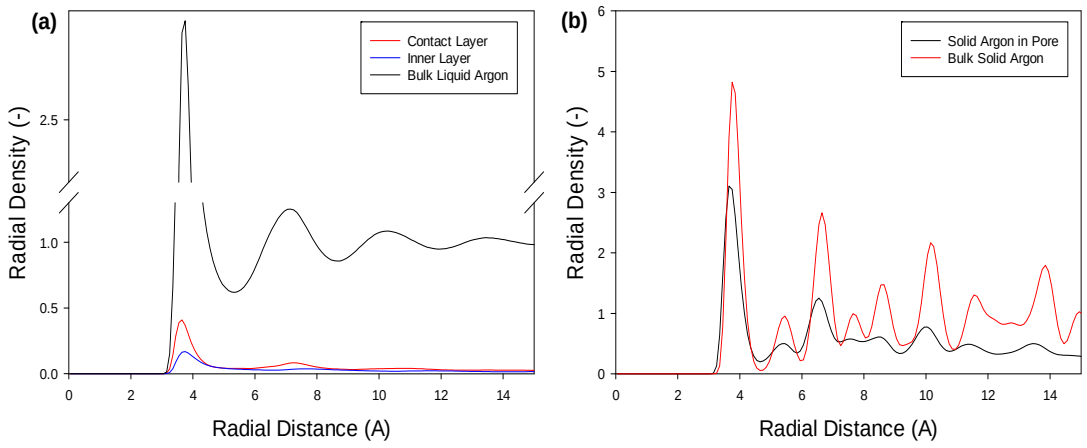

Figure 4.8 The radial density distributions of (a) the contact and inner layers in the pore at Point C, and bulk liquid argon; (b) the adsorbed solid phase at Point F, and bulk solid argon. Points C and F are marked in Figure 4.5.

To further understand the difference in the adsorbate structure along the adsorption and desorption boundaries of the ordering hysteresis loop, we show in Figures 4.9a and b the isosteric heat and the contributions from the solid-fluid (*SF*) and fluid-fluid

(*FF*) interactions, respectively. Along the adsorption boundary from Point C to D where the continuous 2D liquid-solid transition occurs, there is a heat spike in the isosteric heat curve, contributed solely by the *FF* interactions. After Point D where adsorption occurs at the pore mouth, the isosteric heat decreases because of the decrease in both the *SF* and *FF* interactions. At Point F on the desorption boundary, the isosteric heat is higher than at Point C with the same density on the adsorption boundary, due to larger contribution from the *FF* interactions which gives further support to the concept of cohesiveness in the adsorbate.

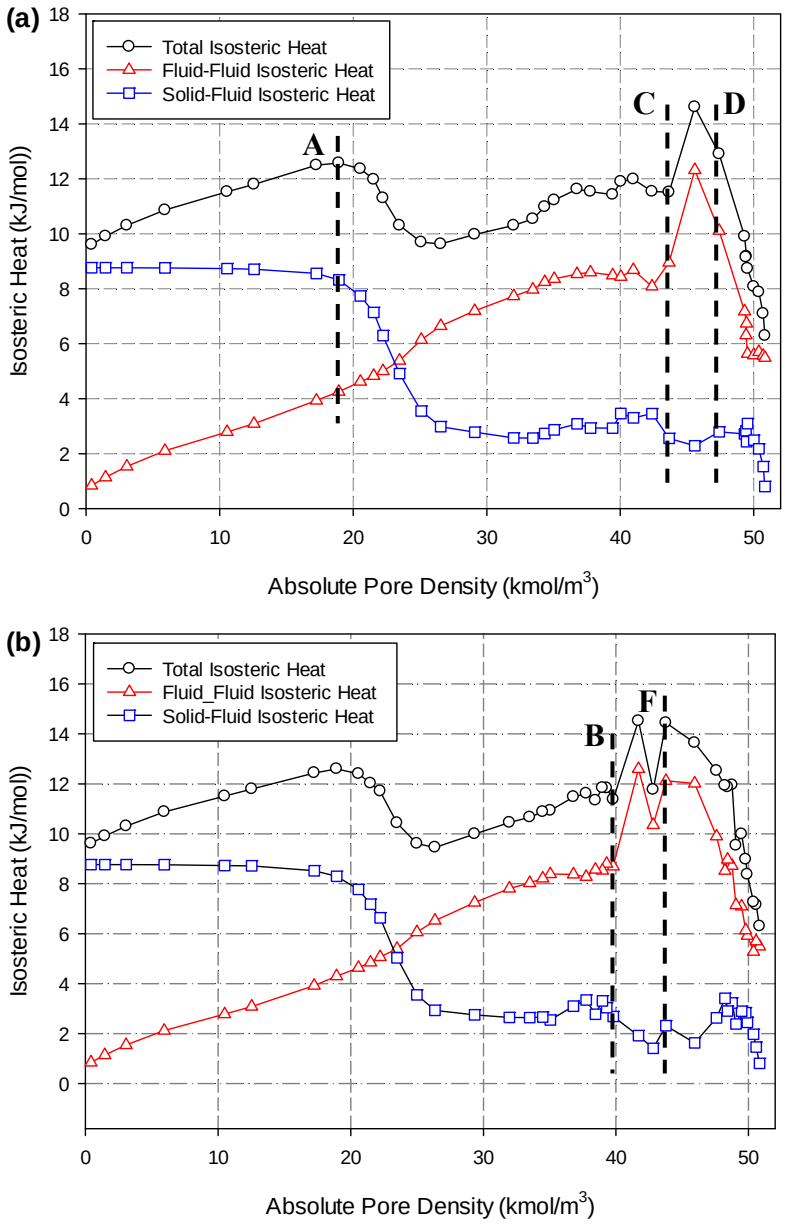

Figure 4.9 The isosteric heat of argon in the finite pore with 1.5 nm width and 20 nm length at 87 K during (a) adsorption and (b) desorption; Points A-D, F correspond to A-D, F in Figure 4.5.

Figure 4.10 shows the local compressibilities of the adsorbate for the whole pore, the contact layer and the core region. The compressibility of the contact layer is the lowest because of the greatest *SF* interaction, and that of the contact and core layers decreases continuously during adsorption, because the increasing cohesiveness of the adsorbate means that molecules move through a shorter distance before encountering repulsive resistance. At Point D where the transition from a liquid-like state to the solid-like state occurs, the compressibility drops steeply to below the compressibility of the bulk liquid (1.53×10^{-9} Pa^{-1}) [248] by about one order of magnitude.

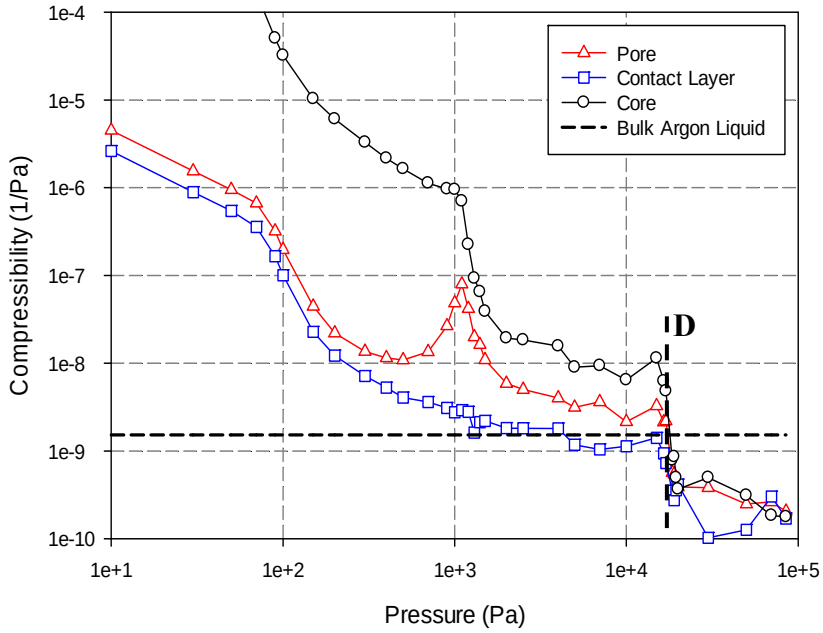

Figure 4.10 Local compressibility of the pore, contact layer and core regions during argon adsorption in the finite pore of 1.5 nm width and 20 nm length at 87 K; Point D corresponds to D in Figure 4.5.

4.3.3. Effects of Temperature

The effects of temperature on the hysteresis and phase transitions in the isotherm for argon adsorption in a finite slit graphitic pore of 1.5 nm width and 20 nm length are illustrated in Figure 4.11a at temperatures of 60 K and 87 K. At 60 K, there is a fused hysteresis loop, indicating that there are two mechanisms at play over the same pressure range, compared to the single ordering transition mechanism at 87 K. The first transition (section I) is the *2D* gas-liquid condensation in the contact layers, which is then followed by a second order transition from a *2D* liquid-like (Point A) to a *2D* solid-like state (Point B), as verified by the *RDD* of the contact layer in

Figure 4.11b. A first order condensation of the inner layers is observed as the 2nd step in the isotherm (section II) and from Point C to D there is a second order transition of the inner layers to a solid-like state. Upon desorption, the adsorbate undergoes a disordering transition and there is a sharp first order evaporation from the inner layers, and the fused desorption branch of the hysteresis loop is due to a combination of condensation/evaporation and the ordering transition of the inner layers.

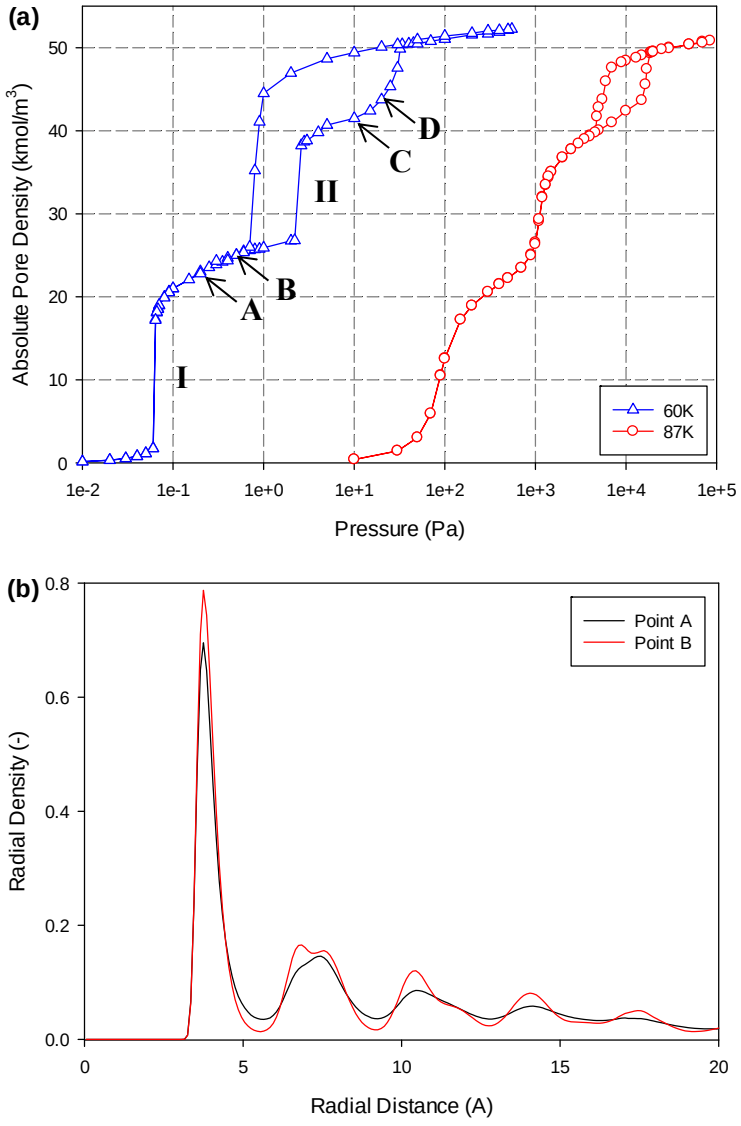

Figure 4.11 (a) The adsorption isotherms of argon at temperatures of 60 and 87 K in finite pores of 1.5 nm width and 20 nm length; (b) the radial density distributions of the contact layer at Points A, B at 60 K.

4.3.4. Effects of Pore Width

Since the freezing temperature of a Lennard-Jones fluid confined to molecularly thin layers is reported to be a nonlinear function of pore width [97], we further investigated the effects of pore width on the behaviour of the isotherm, especially the order of the transitions in the hysteresis loop. We chose a slit pore of 1.8 nm width, which can accommodate four adsorbate layers but with different packing from the 1.5 nm pore. The isotherm of the 1.8 nm pore in Figure 4.12 shows a steep capillary condensation/evaporation of the inner layers, and there is no second order stage in the hysteresis loop, which can be attributed to the incommensurate packing of these layers as shown in the local density distribution in Figure 4.13a. The radial density distribution of the contact layers shows some solid-like features at the second neighbour distance but the inner layer distributions are liquid-like (Figure 4.13b), confirming the random nature of the incommensurate packing. Similar features are also observed for larger pores (Appendix 2).

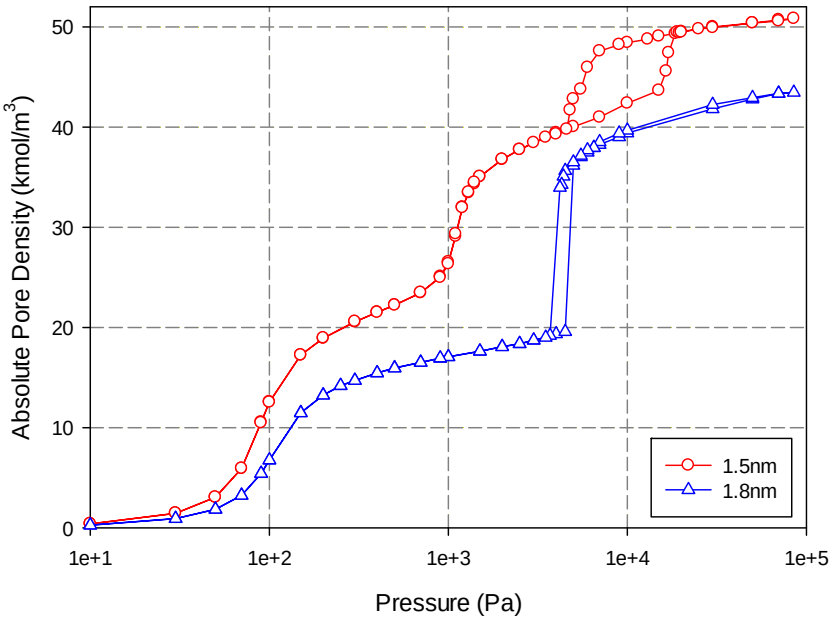

Figure 4.12 The adsorption isotherms of argon in finite length pores with widths of 1.5 and 1.8 nm; the pore lengths are 20 nm and the temperature is 87 K.

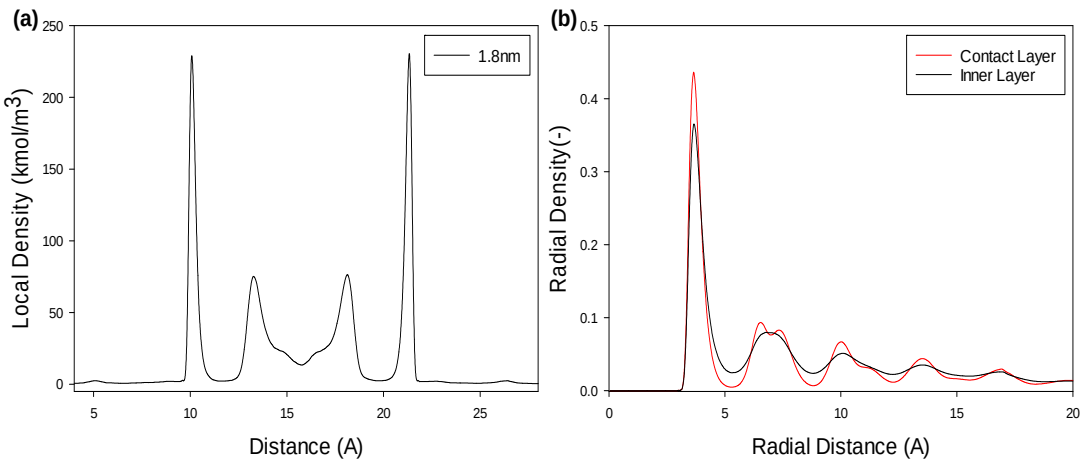

Figure 4.13 (a) The local density distribution; (b) the *2D* radial density distributions for the contact and inner layers at the saturation vapour pressure of 87 K for the 1.8 nm pore.

4.4. Conclusions

In this chapter we have used *GCMC* simulations to study the order-disorder transitions and the restructuring of the adsorbate associated with the hysteresis loops in argon isotherms adsorbed in open slit pores of molecular dimensions. The pore walls were constructed from homogeneous graphite. When the pore is infinitely long the ordering transition is first order with a Type H1 hysteresis loop. However, in finite length pores the transition is second order and hysteresis is entirely the result of adsorbate restructuring. When a first order capillary condensation/evaporation is followed by an ordering transition, the both mechanisms contribute to the hysteresis loop. The ratio of pore width to molecular size plays an important role in the ordering transition, and no ordering hysteresis loop is observed when the pore is incommensurate.

Chapter 5. Adsorption-Induced Deformation in Slit Micropores

5.1. Introduction

In modelling gas adsorption in porous solids it is customary to assume that the solid is a rigid body despite theoretical and experimental evidence that an adsorbate can induce adsorbent deformation due to the forces exerted by adsorbate molecules on the solid surfaces. In Chapter 4, we have found that solid-like phases of argon could be formed in graphitic slit micropores at temperatures above the bulk triple point and this confinement effect could also induce high pressures in the pore, which can be enhanced by a factor of 1000 compared to the bulk phase pressure and would cause the deformation of the solid. Studies have shown that adsorbent deformation can have significant effects on the adsorption capacity and on the heat of adsorption. Therefore, we extend our study to the adsorption-induced deformation in graphitic slit micropores to investigate its underlying mechanisms.

Grand Canonical Monte Carlo (*GCMC*) was applied by Do and co-workers to investigate the adsorption-induced deformation due to argon adsorption in infinitely long graphitic slit pores [218, 219]. Subsequently, *GCMC* was applied to study the deformation in more realistic models of finite length pores connected to bulk gas reservoirs at the pore-ends, allowing the equalization of chemical potentials and mechanical pressure between the bulk gas and the adsorbate within the pore [249, 250]. The effects of pore width, temperature and pore length on the deformation, were examined in this work and it was shown that molecules at different positions make different contributions to the solvation pressure, which has a direct relationship to the deformation. The focus of the present chapter is on adsorption-induced deformation in micropores, for which commensurate or incommensurate packing of the adsorbate molecules is particularly significant.

5.2. Simulation Details

We used argon as the model adsorbate and graphitic slit pores as the model adsorbent. Each of the pore walls is composed of a number of graphene layers that are moveable normal to the pore width with the outermost layers fixed, as shown in Figure 5.1. The separation distances between adjacent layers are determined by minimizing the potential energy of the system under vacuum.

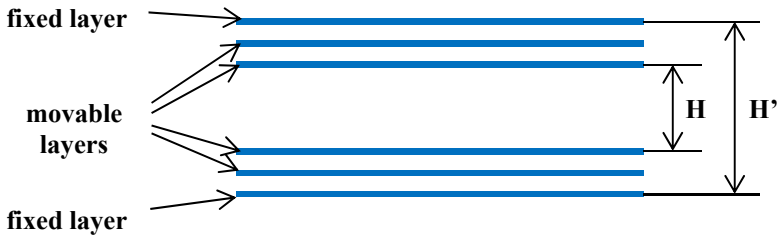

Figure 5.1 Schematic diagram of a slit pore with 4 movable layers and two fixed outermost layers; *H* and *H'* denote the pore width and the distance between the fixed layers, respectively. *H* varies with adsorbate loading while *H'* is constant.

Interaction Energies

The potential energy of a system is comprised of three contributions: (1) fluid-fluid (*FF*), (2) solid-fluid (*SF*) and (3) solid-solid (*SS*) interactions.

The fluid-fluid interaction energy of argon was described by the 12-6 Lennard-Jones (*LJ*) equation, with $\sigma_{ff} = 0.3405$ nm and $\varepsilon_{ff}/k_B = 119.8$ K [243].

For pores of infinite length in the *x*- and *y*-directions (parallel to the surface), each wall has one fixed outermost layer and two or more movable interior layers. The interaction energy between argon and each graphene layer was calculated with the Crowell 10-4 equation. For pores of finite length, the interaction energy was calculated with the Bojan-Steele equation. For both pore models, the molecular parameters for a carbon atom in the graphene layer are $\sigma_{ss} = 0.34$ nm and $\varepsilon_{ss}/k_B = 28$ K, and the carbon density of a graphene layer is 38.2 nm^{-2}. The cross collision diameter and the well-depth of the solid-fluid interaction energy were calculated from the Lorentz-Berthelot mixing rule.

In a deformable pore of infinite length, the solid-solid interaction energy has been given by Do *et al*. [218] For pores of finite length, the solid-solid interaction energy between two layers was calculated by integrating the Bojan-Steele equation.

Monte Carlo Simulation

Grand Canonical Monte Carlo (*GCMC*) was used to simulate argon adsorption in deformable slit pores, with 100,000 cycles used in the equilibration stage and the same number for the sampling stage. Each cycle has 1000 moves of four types:

displacement, insertion, deletion of argon molecule, and displacement of movable graphene layers, chosen at random with the following respective probabilities 333:333:333:1. In the equilibration stage, the maximum displacement step length for argon molecules in each direction was initially set as half the dimension of the simulation box in that direction, was adjusted at the end of each cycle to give an acceptance ratio of 20%, and then kept constant during the sampling stage. For the displacement of a movable layer, one layer was chosen at random and displaced in the direction normal to the pore walls, with acceptance following the usual Metropolis rule. The displacement step length for a movable layer was kept as 1/1000 of the separation distance between adjacent layers (set initially 0.3354 nm) in both the equilibration and sampling stages. The dimension of the simulation box in the *x*-direction was set as 10 times the collision diameter of argon. For pores of infinite length, the dimension in the *y*-direction was set as 20 nm, with periodic boundary conditions applied in both the *x*- and *y*-directions. For finite pores, the dimension in the *y*-direction was determined by the pore length with two bulk gas reservoirs of 3nm length connected at each end of the pore. In the calculation of interaction energies, the cut-off radius was set as 5 times the collision diameter of argon.

5.3. Results and Discussions

5.3.1. Effects of Pore Width

We first conducted *GCMC* simulations on argon adsorption at 87 K in deformable finite slit pores with four moveable layers, lengths of 20 nm and various widths in the micropore range. We present in Figure 5.2 the maximum adsorbate density, the solvation pressure and the compressibility of the adsorbed phase at the saturation vapour pressure (P_0) as functions of the initial pore width. The minimum width accessible to argon molecules is 0.60 nm. In pores of initial width 0.65 nm, only one adsorbate layer can be accommodated. As the initial pore width is increased both the maximum density and the solvation pressure oscillate synchronously with a damped amplitude. We noted that the solvation pressure is zero when the pore widths are initially 0.99 nm, 1.3 nm, 1.62 nm and 1.93 nm, indicating that there is no net force acting on the pore walls at P_0. This is tantamount to saying that the packing in these

pores is perfectly commensurate; i.e. an integral number of layers (2, 3, 4 and 5) can be accommodated in these pores, as confirmed by the location of the corresponding minima in the compressibility plot in Figure 5.2c. It is worth pointing out that, even though the solvation pressure at P_0 is zero for these commensurate pores, it is not zero at pressures less than P_0, because of the variation in the local solvation pressure distribution with pressure. It is only at P_0 that the force pushing the pore walls apart is exactly balanced by the attractive forces pulling them together. Figure 5.2 distinguishes the commensurate from the incommensurate pore widths under the stated conditions.

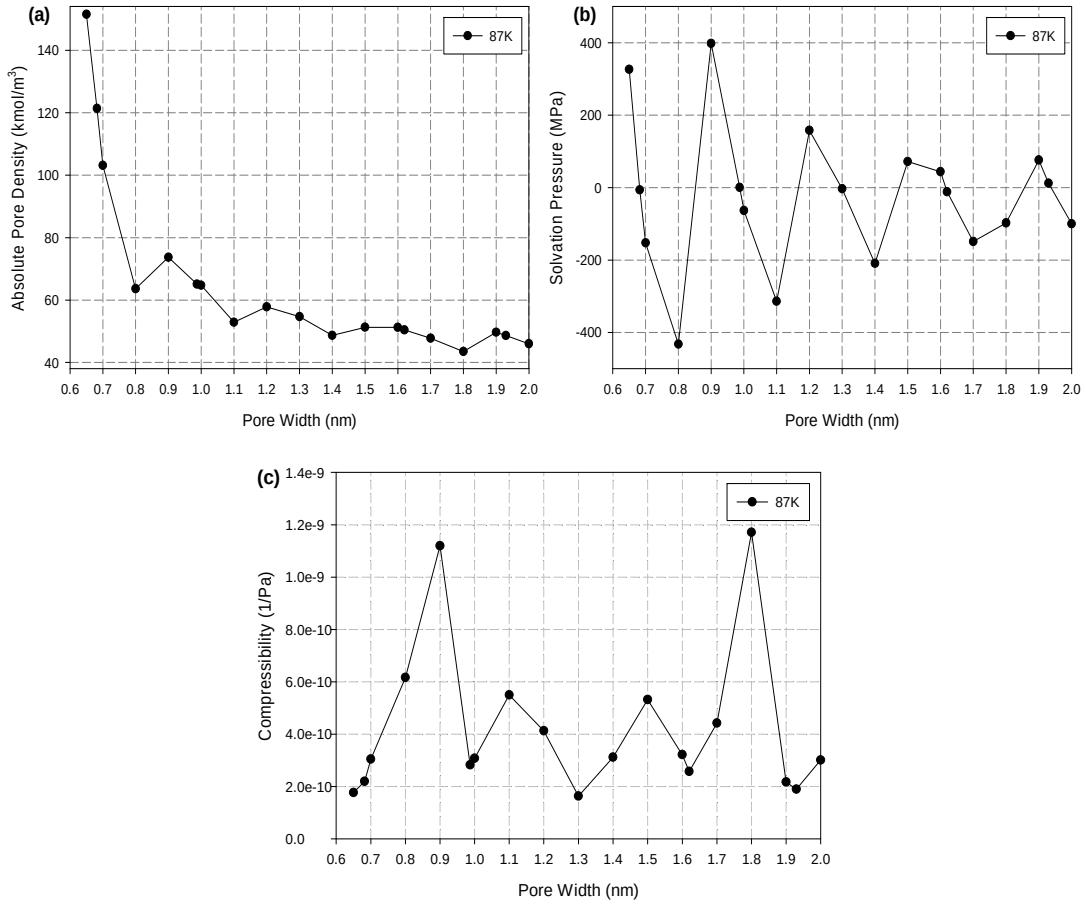

Figure 5.2 (a) The maximum loading, (b) the solvation pressure and (c) the compressibility as a function of the initial pore width for argon adsorption at 87 K and at the saturation vapour pressure, P_0, in finite slit pores of 20 nm length with four movable layers and two fixed outermost layers. The initial pore width with the corresponding distance between the fixed layers, H', is shown in Table 5.1.

Table 5.1 The initial pore width and the corresponding distance between the fixed layers

H (nm)	0.65	0.7	0.8	0.9	1.0	1.1	1.2	1.3
H' (nm)	2.0144	2.0610	2.1576	2.2566	2.3550	2.4545	2.5543	2.6541
H (nm)	1.4	1.5	1.6	1.7	1.8	1.9	2.0	
H' (nm)	2.7539	2.8537	2.9538	3.0536	3.1535	3.2535	3.3535	

Figures 5.3a and b show the solvation pressure and the fractional change of the pore width with loading (from zero to a maximum loading at P_0) for argon adsorption at 87 K in pores of various initial widths. The stress-strain curve of fractional change in pore width ($\Delta H/H_0$, where ΔH equals $H - H_0$ and H_0 is the initial pore width under vacuum) with loading (expressed as a percentage) is proportional to the solvation pressure, as confirmed by the linear plot of $\Delta H/H_0$ versus the solvation pressure in Figure 5.3c. The inverse of the slope of this plot is the bulk modulus, which depends on pore width, pore length (Section 5.3.3) and the number of movable layers (see Section 5.3.4). The bulk moduli of the 0.65 nm and 0.9 nm pores (with 4 moveable layers) are 12 and 20 GPa, respectively, indicating that the modulus increases moderately with pore width. These values are comparable to the bulk modulus of most solids, for example the reported bulk modulus of graphite is 15.3 GPa and that of silica is 35 GPa. From the behaviour of $\Delta H/H_0$ versus loading in Figure 5.3b, we can classify the deformation into four categories:

1. Expansion of 0.65 nm pore

Expansion is the only mode of deformation in this pore because it only accommodates one molecular layer, resulting in positive solvation pressures for all loadings.

2. Contraction at all loadings

The pattern of contraction at all loadings is exemplified by the 0.7 nm pore, which is wider than a monolayer, but not wide enough to accommodate two layers. Consequently, the adsorbate molecules pull the movable graphene layers on the opposite walls towards each other to optimise the solid-fluid interactions which over-compensate the positive solid-solid potential energy.

3. Contraction followed by expansion

This behaviour is found for most pore widths. As an example, consider the pore with an initial width of 0.9 nm; this pore is too small to accommodate two distinct layers at very low loadings and molecules on opposite pore walls therefore overlap. Because of this the Gibbs free energy is lowered by pulling the movable graphene layers on opposite walls towards each other, thus lowering the solid-fluid energy by more than enough to compensate for the positive solid-solid potential energy. As loading is increased, the pore expands sufficiently to accommodate two distinct layers, which lowers the fluid-fluid energy and also the solid-fluid energy because more molecules are closer to the potential energy minimum. The combination of lower *SF* and *FF* energies is more than sufficient to compensate for the reduced attraction between the solid layers which resulted from pushing the movable graphene layers outward.

4. Commensurate pores:

Examples of commensurate pore widths are 0.99 nm, 1.3 nm and 1.62 nm. These pores can accommodate an integral number of molecular layers at P_0, at which pressure the solvation pressure is zero, as discussed earlier and shown in Figure 5.2b.

The local density distributions and the local solvation pressure distributions, at the saturation vapour pressure P_0, for pores of width 0.65 nm, 0.7 nm, 0.9 nm and 1.3 nm pores highlight the relative contributions from molecules pushing the walls apart and those pulling them together at the maximum loading. These distributions form the basis for a microscopic explanation of the linear correlation between the solvation pressure and the percentage change in pore width.

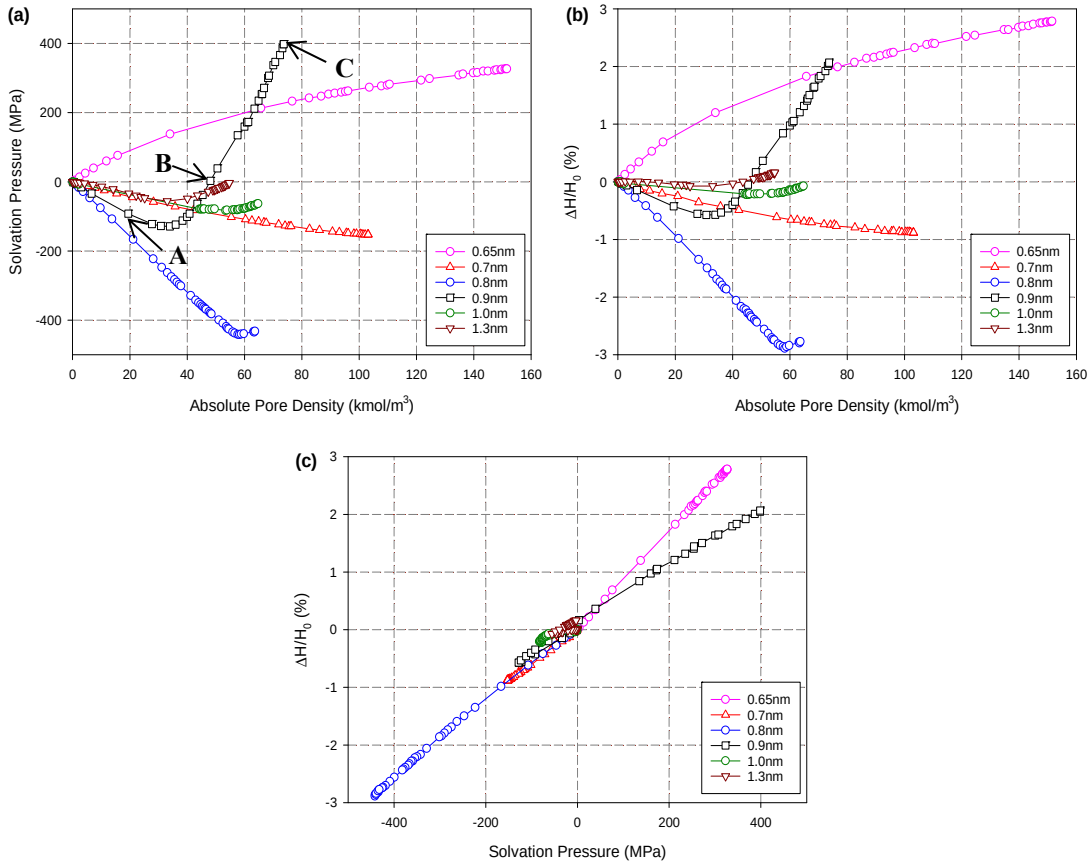

Figure 5.3 (a) The solvation pressure versus loading, (b) the percentage change of the pore width versus loading, (c) the percentage change of the pore width versus the solvation pressure during argon adsorption at 87 K in slit pores of different initial widths and 20 nm length with four movable layers and two fixed outermost layers.

With the exception of the 0.65 nm pore (Figure 5.4a), whose local solvation pressure is positive at all distances (i.e. all molecules have a tendency to push the pore walls apart), the local solvation pressure distribution shows two distinct regions. In the region close to the pore walls the solvation pressure is positive, but is negative in the interior; i.e. molecules near the pore walls some of which are in the repulsive part of the *SF* potential have a tendency to push them apart while those in the interior tend to pull them together. Since the total solvation pressure is the sum of the local solvation pressures, it could be either positive or negative. The 0.7 nm pore is an example of a case where attraction of the pore walls by molecules in the interior (the cross hatched area in Figure 5.4b) dominates over the repulsion due to those adjacent to the pore walls (the red area), resulting in a negative solvation pressure and pore contraction at P_0. In the 0.9 nm pore (Figure 5.4c) we observe the opposite; the

positive local solvation pressure dominates at P_0, and the pore expands. For the pore with an initial width of 1.3 nm, the local positive solvation pressure balances the negative pressure at P_0 (Figure 5.4d), resulting in zero solvation pressure and therefore there is no deformation. We again emphasise that this behaviour is at P_0 and that at pressures less than P_0 the behaviour is different, as discussed below.

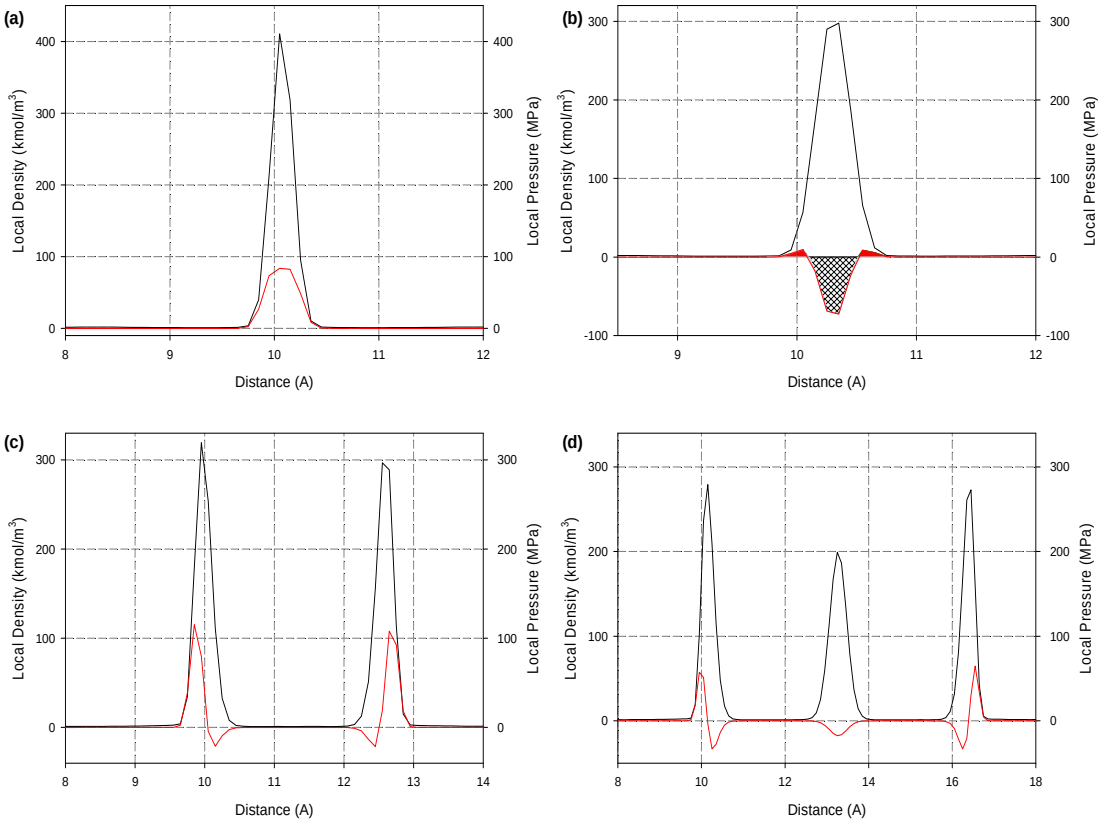

Figure 5.4 The local density distributions (black lines) and the local solvation pressure distributions (red lines) for argon adsorption at 87 K at the saturation vapour pressure P_0 for pore widths (a) 0.65 nm, (b) 0.7 nm, (c) 0.9 nm, (d) 1.3 nm pores.

To illustrate the evolution of the local density distribution and the local solvation pressure distribution with loading (pressure), we show in Figures 5.5a and b these distributions at the Points A-C, marked in Figure 5.3a, for the 0.9 nm pore, with the corresponding snapshots shown in Figure 5.5c. The local density distribution increases in area and shifts closer to the pore walls when the loading is increased from Point A to C (Figure 5.5a), and the corresponding local solvation pressure distribution also shifts closer to the pore walls (Figure 5.5b). At the low loading (Point A) the contribution from the negative local solvation pressures is greater than that from the positive ones and the pore contracts. On the other hand, at the higher

loading at Point C (the saturation vapour pressure, P_0) the opposite is true, and the pore expands. Therefore, there is an intermediate loading between these two values, where the contributions from the positive and negative local pressures cancel each other (Figure 5.5b), here the solvation pressure is zero and no change occurs in the pore width (Point B in Figure 5.3a).

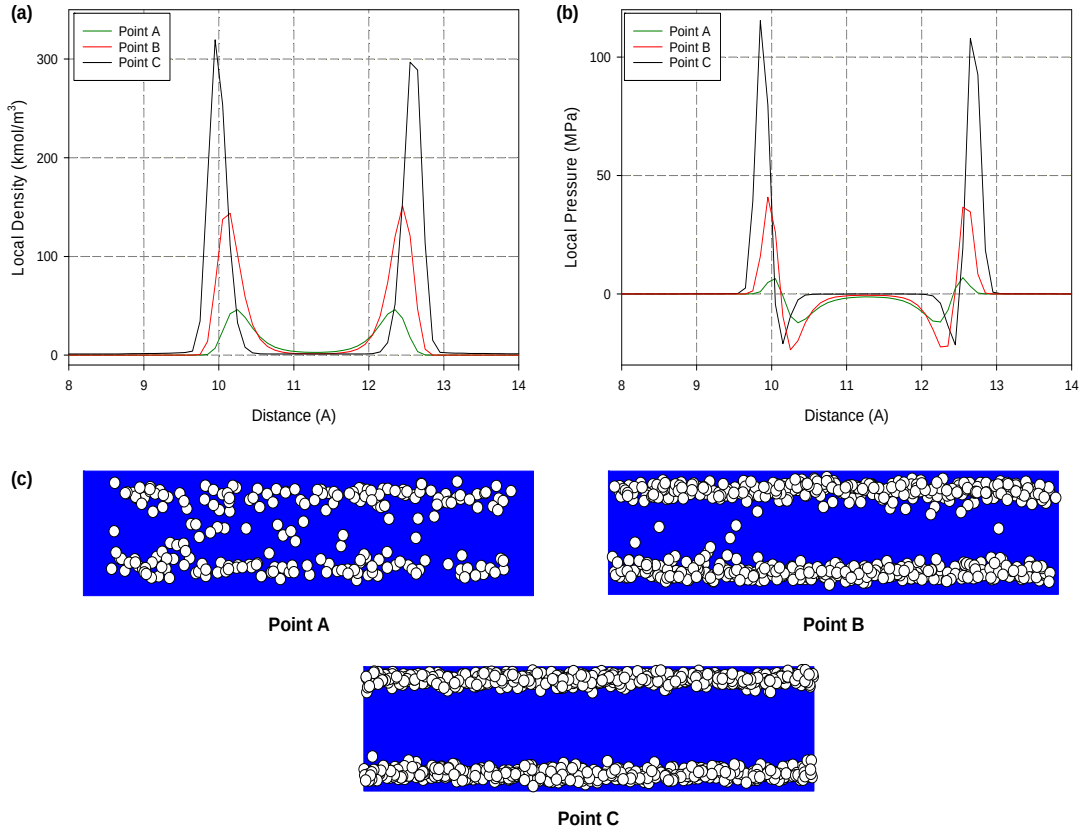

Figure 5.5 (a) The local density distributions, (b) the local solvation pressure distributions and (c) the snapshots of argon molecules at Points A, B, C of 0.9 nm pore in Figure 5.3a.

5.3.2. Effects of Temperature

At supercritical temperatures, the packing effect is different from that at sub-critical temperatures because of the increased thermal fluctuations. Figures 5.6a and b show the solvation pressure and the fractional change of the pore width, $\Delta H/H_0$, as a function of the initial pore width for argon adsorption at 298 K and 100 MPa, and at 87 K and P_0 respectively. For small pores (0.65-1.1 nm), both the solvation pressure and $\Delta H/H_0$ versus pore width exhibit the same pattern as those at the sub-critical temperature. However, at the supercritical temperature they end in a plateau when the pore width is greater than about 1.1 nm. This illustrates how thermal fluctuations

reduce molecular packing and shows that the reduction becomes greater as pore size increases.

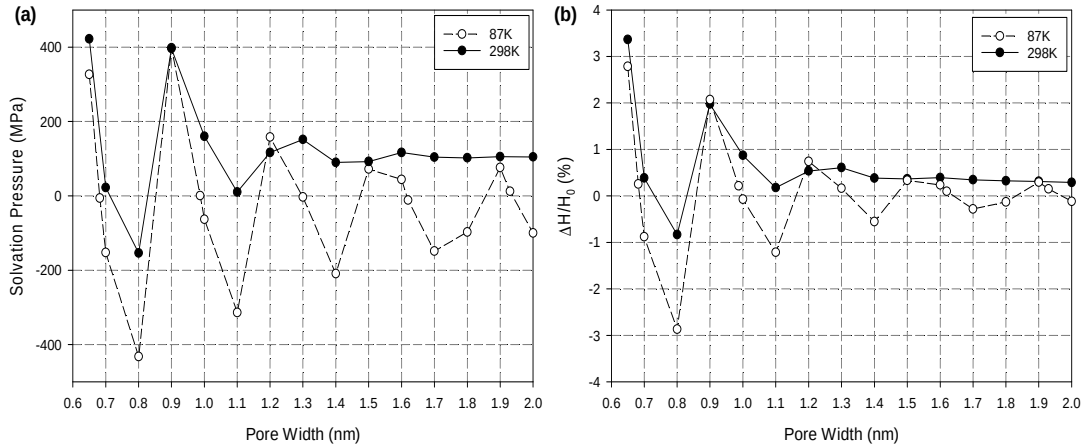

Figure 5.6 (a) The solvation pressure and (b) the percentage change of the pore width for argon in pores with different initial widths (0.65-2 nm) and 20 nm length at 298 K and 100 MPa, compared with argon at 87 K at the saturation vapour pressure P_0. The pores are composed of four movable layers and two fixed outermost layers.

Figures 5.7a and b show the change in solvation pressure with loading as a function of temperature for argon adsorbed at different temperatures in pores with initial widths of 0.65 nm and 0.8 nm. The corresponding fractional change in pore width, $\Delta H/H_0$, expressed as a percentage, is plotted as a function of loading in Figures 5.7c and d. Both the solvation pressure and $\Delta H/H_0$ increase with temperature at a given loading, and are linearly related (Figures 5.7e and f). The slopes (i.e. the inverse of the bulk modulus) for both pore widths are independent of temperature, which is consistent with the bulk modulus being an intrinsic property of the solid.

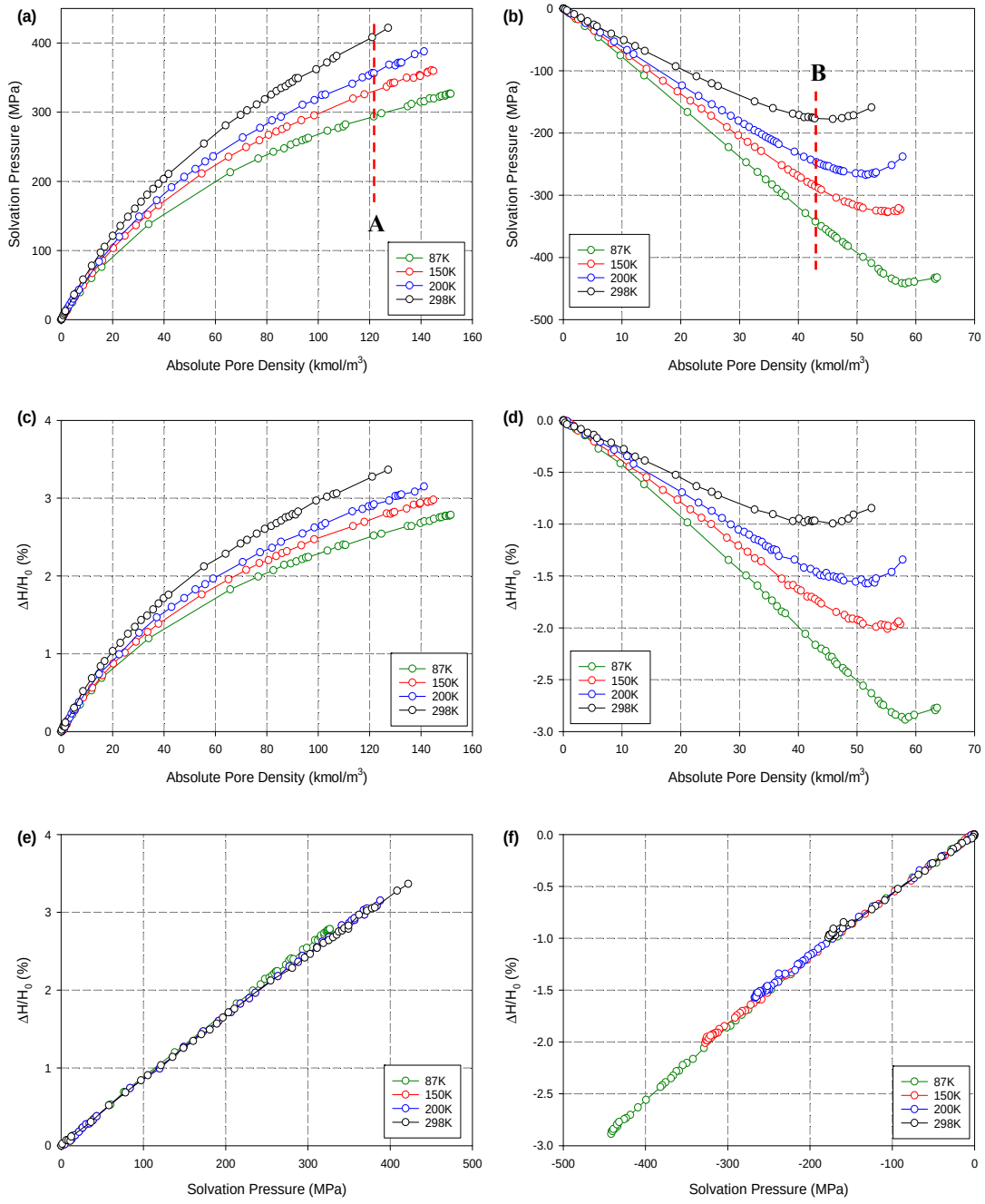

Figure 5.7 The solvation pressure versus loading in (a) 0.65 nm, (b) 0.8 nm pores; the percentage change in pore width versus loading in (c) 0.65 nm, (d) 0.8 nm pores; the percentage change in pore width versus the solvation pressure in (e) 0.65, (f) 0.8 nm pores for argon adsorption at different temperatures; the pores are composed of four movable layers and two fixed outermost layers and the pore length is 20 nm.

To shed further light on the effects of temperature, we present in Figure 5.8 the local density distribution, and the local solvation pressure distribution, at the points A and B in Figure 5.7, for the pores with initial widths of 0.65 nm and 0.8 nm. For the 0.65

nm pore, both the local density distribution and the local solvation pressure distribution move closer to the repulsive region of the potential as temperature increases, increasing the tendency for the adsorbate to push the moveable layers apart and expand the pore. It is interesting to see that the excursion of molecules towards the pore walls at high temperatures occurs at the expense of a decrease in the local solvation pressure at the centre of the pore. The same conclusions also apply for the 0.8 nm pore (Figures 5.8b and d), i.e. the contribution from the positive local solvation pressures increases while that from the negative ones decreases. For this 0.8 nm pore, where contraction occurs at all loadings, the effects of the temperature result in less contraction at higher temperatures.

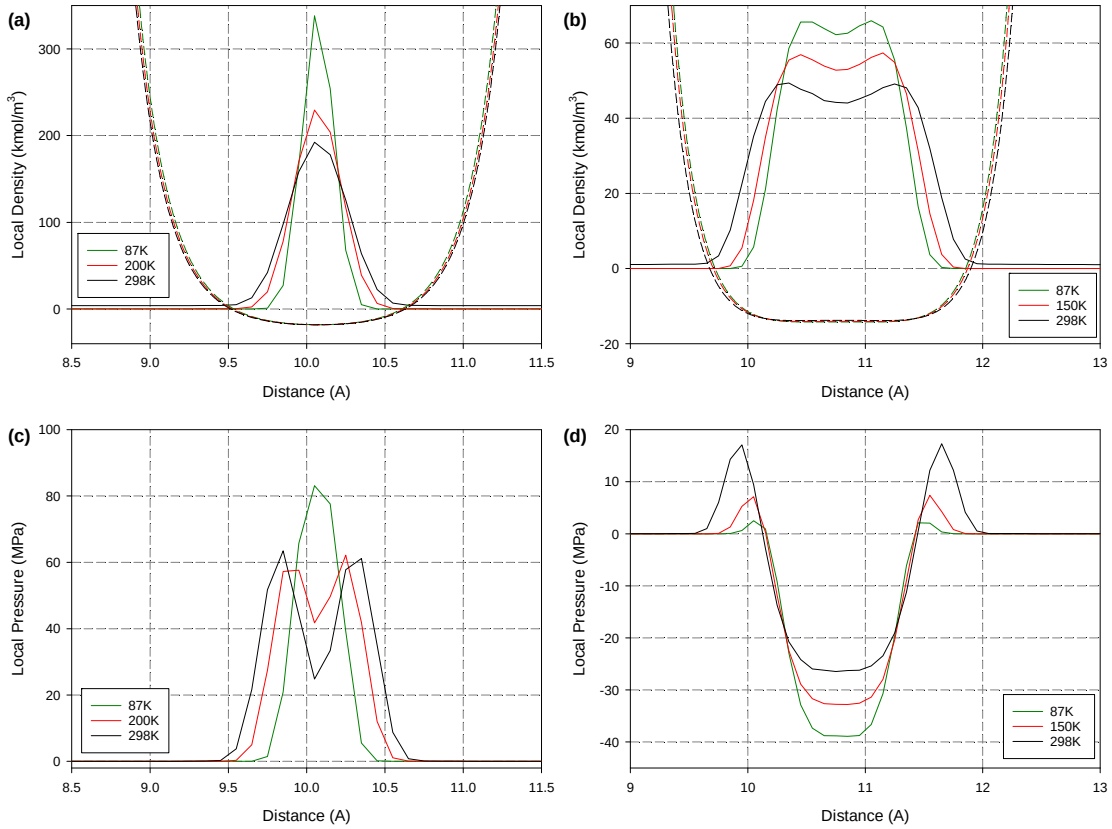

Figure 5.8 The local density distributions at (a) Point A of 0.65 nm, (b) Point B of 0.8 nm pores. The dashed lines show the solid-fluid potential energy function. The local solvation pressure distributions at (c) Point A of the 0.65 nm pore, and (d) Point B of the 0.8 nm pore, at different temperatures. Points A-B are marked in Figure 5.7.

5.3.3. Effects of Pore Length

Figure 5.9 shows the percentage change of the pore width with solvation pressure for argon adsorption at 87 K in pores of different lengths and initial widths of 0.65 nm

and 0.8 nm. The deformation is greater and the bulk modulus is smaller in the shorter pores at the same solvation pressure. However, the trend in deformation with pore width is the same, irrespective of the pore length. A similar conclusion also holds for adsorption at the supercritical temperature of 298 K.

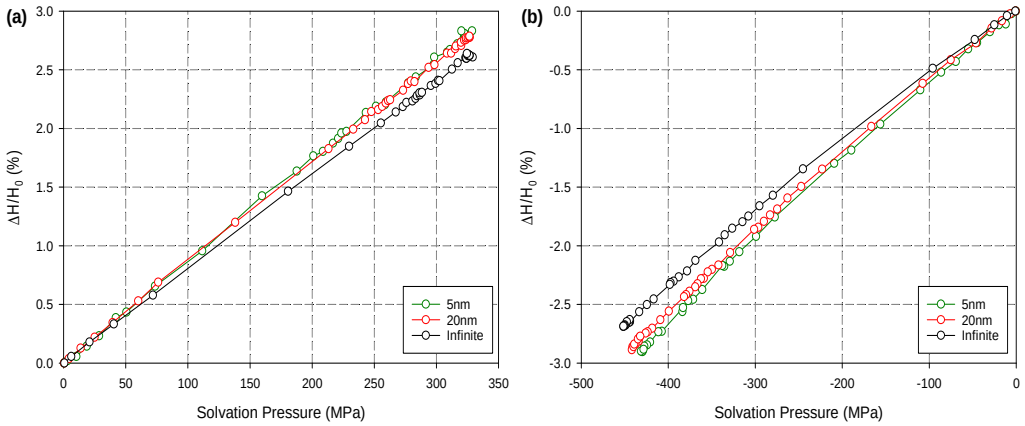

Figure 5.9 The percentage change of the pore width versus the solvation pressure in (a) 0.65, (b) 0.8 nm pores with different pore lengths for argon adsorption at 87 K. The pores are composed of four movable layers and two fixed outermost layers.

5.3.4. Effects of Number of Movable Layers

The effects on the deformation, of changing the number of movable layers, are shown in Figure 5.10, where we plot the percentage change of the pore width versus the solvation pressure for argon adsorption at 87 K in pores of 0.65 nm initial width with different numbers of movable layers. When the number of movable layers is increased from 2 to 4 on each wall, the pore deformation increases at a given solvation pressure as shown by an increase in the slope of the plot. The bulk modulus decreases from 12 GPa to 6 GPa, as expected, because it is easier to compress a larger number of movable layers.

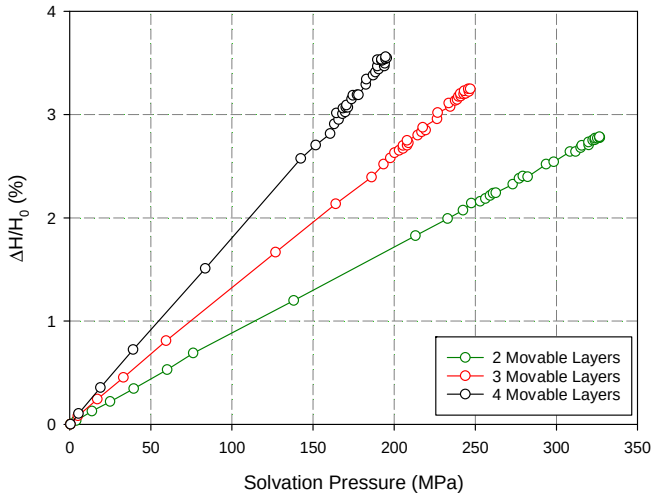

Figure 5.10 The percentage change of the pore width versus the solvation pressure in 0.65 nm pore with different number of movable layers on each wall for argon adsorption at 87 K; the pore length is 20 nm.

5.3.5. Comparison with Rigid Pore

As an example of the effects of pore deformation in this system, we compare the change in pore width and solvation pressure with loading for argon adsorption at 87 K in rigid and deformable pores with an initial width of 0.65 nm in Figures 5.11a and b, respectively. In the deformable pore, the pore expands from 0.65 nm at zero loading to 0.668 nm at the maximum loading at P_0. The solvation pressure is smaller in the deformable pore because there is a change in the pore width. Figure 5.11c shows that the distribution of solvation pressure is more delocalised in the deformable pore, and the much smaller area under the curve is consistent with the lower total solvation pressure. The difference between rigid and deformable pores diminishes as pore width increases.

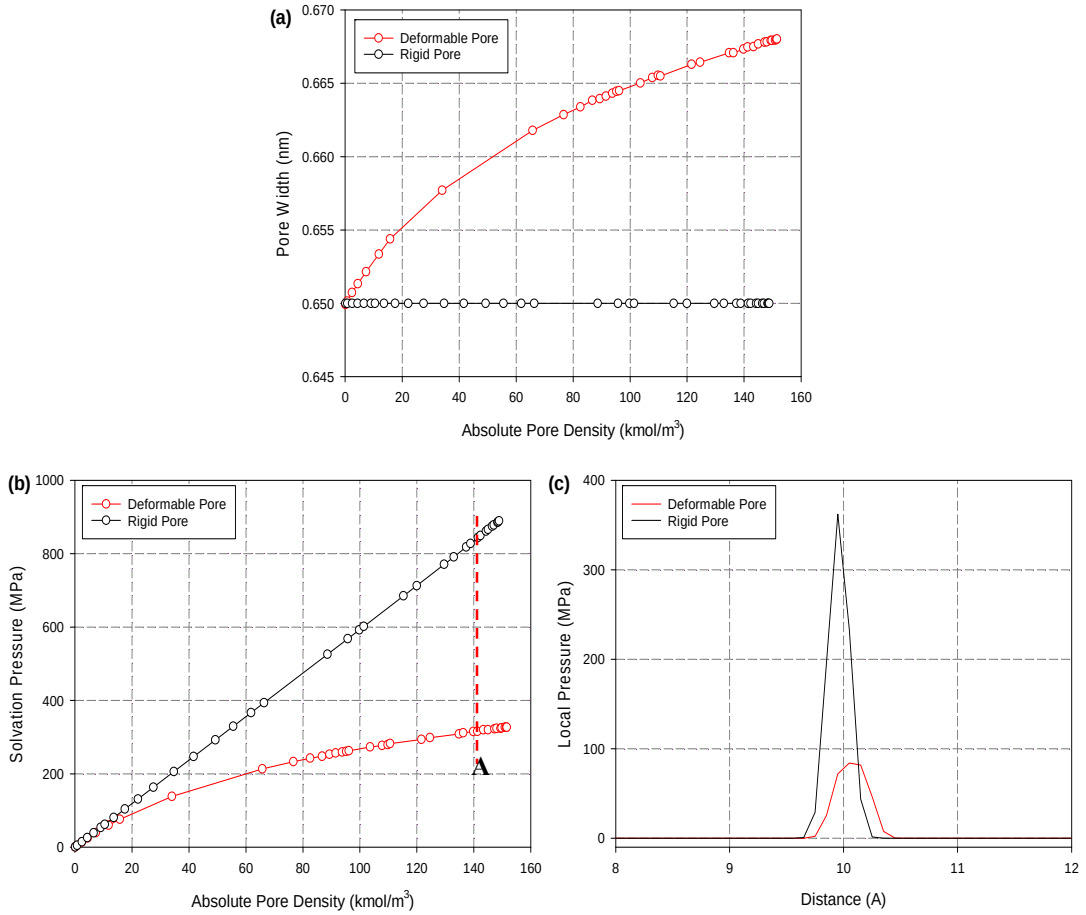

Figure 5.11 (a) The pore width versus loading and (b) the solvation pressure versus loading before and after deformation at 87 K in 0.65 nm pore; (c) the local solvation pressure distributions at Point A as labelled in Figure 5.11(b) before and after deformation; the pore length is 20 nm. The deformable pore has four movable layers and two fixed outermost layers and the rigid pore has a total of six layers.

5.4. Conclusions

In this Chapter, solvation pressure is found to be the driving force for the deformation induced by adsorption of argon in graphitic slit micropores. The local solvation pressure, plotted as a function of distance from the pore wall, reveals the way in which molecules at different locations contribute to the solvation pressure. Molecules near the pore walls have positive local solvation pressure and tend to expand the pore, while those in the interior have negative local solvation pressure and tend to contract the pore. At higher temperatures, the positive local solvation pressure is enhanced and pore expansion becomes more favoured. Packing effects are important under subcritical conditions, but at supercritical temperatures, and in wider pores, thermal fluctuations play a more significant role. Pore length also

affects deformation, especially in short pores, but it does not change the pattern of deformation as a function of pore width and temperature. The majority of the simulations reported here were made with a graphitic pore model having four moveable layers. When more moveable layers are added to the model, the deformation is increased.

Chapter 6. Adsorption-Induced Deformation in Slit Mesopores

6.1. Introduction

In Chapter 5, we have studied the adsorption-induced deformation in microporous solids and we extend the study to mesopore range in this Chapter, as the deformation behaviours of mesoporous solids are more complicated. In general, the deformation of mesoporous solids usually exhibits alternative stages of expansion and contraction, and a significant hysteresis could be observed in the course of desorption accompanied with the adsorption-desorption hysteresis.

We investigate systematically the deformation behaviours of graphitic slit mesopores with an aim of gaining better insight into the mechanisms of deformation. Different deformation behaviours are observed at different stages in the adsorption process, with different mechanisms and effects from the pore width and temperature.

6.2. Simulation Models

We use argon as the model adsorbate and graphitic slit pores as the model adsorbent. The schematic diagram of the pore model is shown in Figure 6.1. The pore is composed of two fixed outermost layers and a number of movable layers that are movable normal to the pore walls.

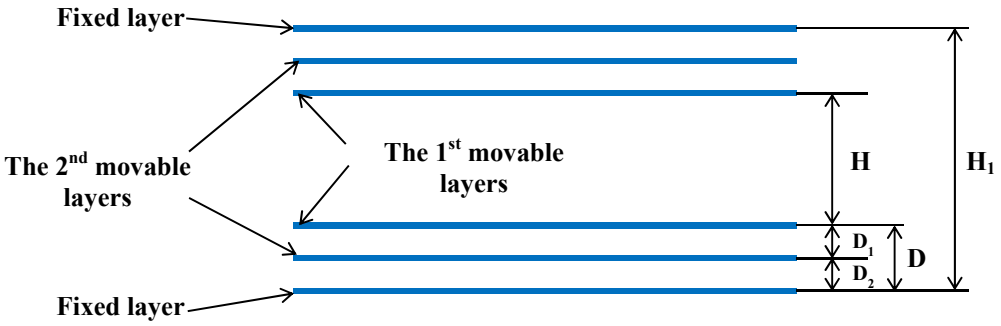

Figure 6.1 Schematic diagram of a slit pore with 4 movable layers and two fixed outermost layers; H and H_1 denote the pore width and the distance between the outermost fixed layers, respectively. D, D_1, D_2 denote the distances between the 1st movable layer (the innermost layer) and the fixed layer, the 1st and the 2nd movable layers, the 2nd movable layer and the fixed layer, respectively. H, D, D_1 and D_2 vary with adsorbate loading while H_1 is constant.

6.3. Results and Discussions

6.3.1. Adsorption-Induced Deformation in a 3 nm Pore

We define the strain as the fractional change in pore width $\Delta H/H_0$, where $\Delta H = H - H_0$ and H_0 is the initial pore width. The isotherms for strain and for argon density at 87 K, in a pore with an initial width of 3 nm, are shown in Figures 6.2a and b on linear and semi-logarithmic scales, respectively. The adsorption isotherm is typical for mesoporous solids: (1) molecular layering on the pore walls, (2) a sharp increase in density on capillary condensation and (3) pore filling. The strain isotherm exhibits three stages corresponding to these stages in the adsorption.

1. In the molecular layering region, and especially at sub-monolayer coverages, the pore expands and the strain isotherm exhibits a shape similar to the adsorption isotherm.
2. During capillary condensation, the pore contracts sharply.
3. Beyond the capillary condensation pressure, the pore contracts further until saturation vapour pressure (P_0) is reached.

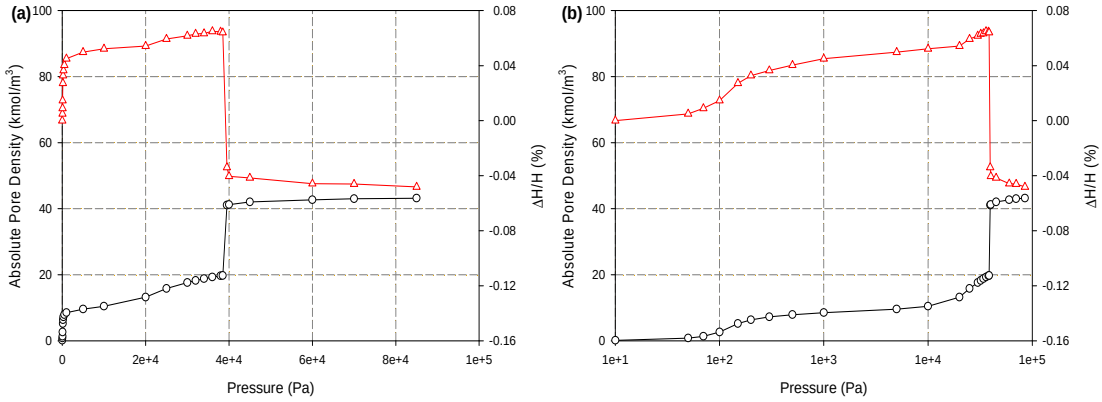

Figure 6.2 The adsorption isotherm (black line) and the strain isotherm (red line) for argon adsorption at 87 K in a slit pore of 3 nm initial width shown on (a) linear and (b) semi-logarithmic scales; the pore length is 20nm with four movable layers and two fixed outermost layers.

To provide an explanation for the pore expansion in the multilayer region, we show in Figure 6.3a the surface excess density (μmol/m^2) versus the bulk pressure for argon adsorption at 87 K on graphite, which is composed of one fixed graphene layer and two movable layers. The changes of the interlayer spacings δD_1, δD_2 with respect to the initial values and the change of the distance between the uppermost

movable layer and the fixed layer $\delta D = \delta D_1 + \delta D_2$ are shown in Figures 6.3b and c. Also plotted in Figure 6.3a is the adsorption isotherm of the 3 nm pore, plotted in terms of the surface excess density, for comparison with the adsorption isotherm of the graphite. The following observations may be made:

1. The adsorption isotherms and the plot of δD versus pressure for these two systems (the 3 nm pore and graphite) agree with each other in the multilayer region, indicating that the two pore walls behave like independent surfaces, i.e. the deformation at one wall in the 3 nm pore is unaffected by the presence of the opposite wall.
2. δD decreases with pressure in the multilayer region, which means that the graphene layers are compressed and the pore width expands.
3. The changes in the interlayer spacings δD_1, δD_2 are the same in the 3 nm pore and the graphite (Figure 6.3b).

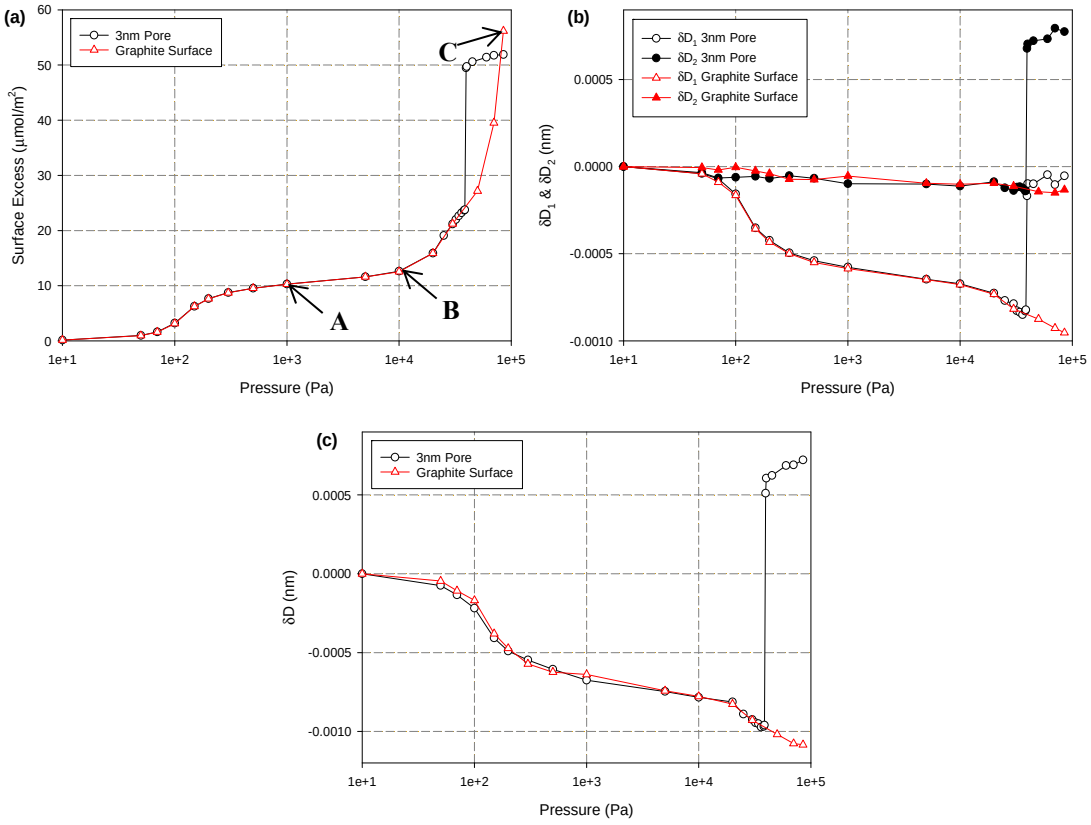

Figure 6.3 Changes in the adsorbent for argon adsorbed at 87 K in a slit pore of 3 nm initial width and on a graphite surface; the length of the pore and the surface is 20 nm, both pore walls and the surface are constructed with two movable and one fixed outermost layers. (a) The adsorption isotherm. (b) The change in distances between the 1st movable layer and the 2nd movable layer (δD_1), and the 2nd movable layer and the fixed layer (δD_2) with bulk pressure. (c) The change in distance between the 1st movable layer and the fixed layer with bulk pressure.

Figure 6.4a shows the distances between the 1st adsorbate layer and the 1st movable layer (ΔZ_1), the 2nd movable layer (ΔZ_2), and the fixed layer (ΔZ_3) plotted against the bulk pressure for argon adsorption on a graphite surface at 87 K. The position of the 1st adsorbate layer is determined by averaging over the z-coordinate of the adsorbate molecules in this layer, ($z_{ave} = \sum_{i=1}^{n} \rho_i z_i \Big/ \sum_{i=1}^{n} \rho_i$).

The interesting features summarized below, shed light on the microscopic mechanism resulting from the negative change in the *SF* potential due to the compression of the graphite surface, which balances the penalty of the positive change in the *SS* potential. Due to the lowering of the total potential, the stability of the system becomes higher than that in fixed pores.

1. In the sub-monolayer coverage region, ΔZ_1 increases slightly (supporting information is given in Appendix 3) while ΔZ_2 and ΔZ_3 decrease. The result is a lowering of the *SF* potential between the adsorbate molecules in the sub-monolayer and the 2nd graphene layer and to a lesser extent with the fixed layer.
2. At the onset of the 2nd adsorbate layer (Point B in Figure 6.3a), ΔZ_1, ΔZ_2 and ΔZ_3 decrease sharply with the increase of pressure until the saturation vapour pressure P_0 is reached (Point C in Figure 6.3a). This occurs because the multilayers are closer to all the graphene layers, resulting from the balance between the stronger *SF* interaction and the penalty from the more repulsive *SS* interaction. The local density distributions at these loadings are shown in Figure 6.4b.

After the initial expansion the pore width contracts across the capillary condensation to become smaller than its initial value of 3 nm pore. This is because of the attraction between the condensate in the pore interior and the pore walls, which lowers the *SF* potential. Because of the contraction of the pore, the interlayer spacings relax from their compressed state in the multilayer region, resulting in a decrease in the *SS* potential during the capillary condensation, as shown in Figure 6.5a. After completion of the capillary condensation, more particles are added into

the pore and the pore contracts to further lower the *SF* potential at the expense of the *SS* potential because of the expansion of the movable layers (i.e. a positive change in δD_1 and δD_2). We have found that the deformation pattern after the capillary condensation is a function of both pore width and temperature and elaborate this in more detail in Sections 6.3.2 and 6.3.3 below.

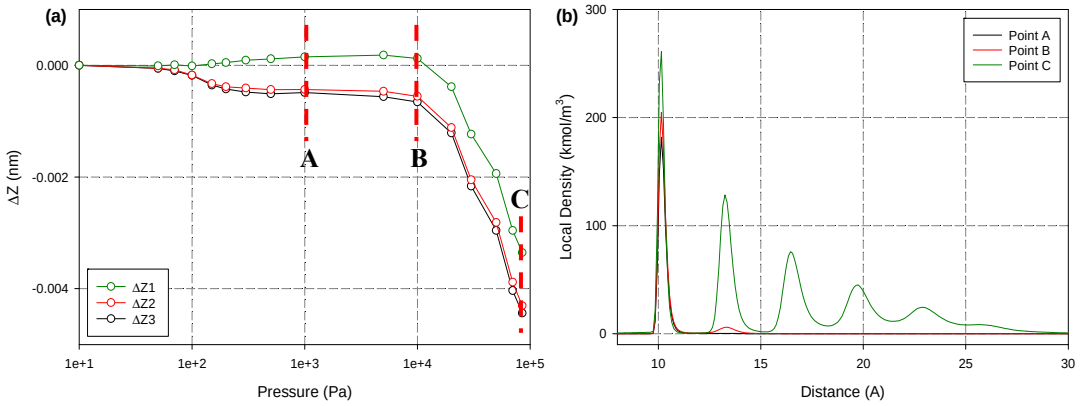

Figure 6.4 (a) The change of the distances between the 1st adsorbed layer and the 1st movable layer (ΔZ_1), the 2nd movable layer (ΔZ_2), and the fixed layer (ΔZ_3) with bulk pressure, (b) the local density distributions at Points A-C as marked in Figure 6.3a for argon adsorption at 87 K in a slit pore of 3 nm initial width and on a graphite surface.

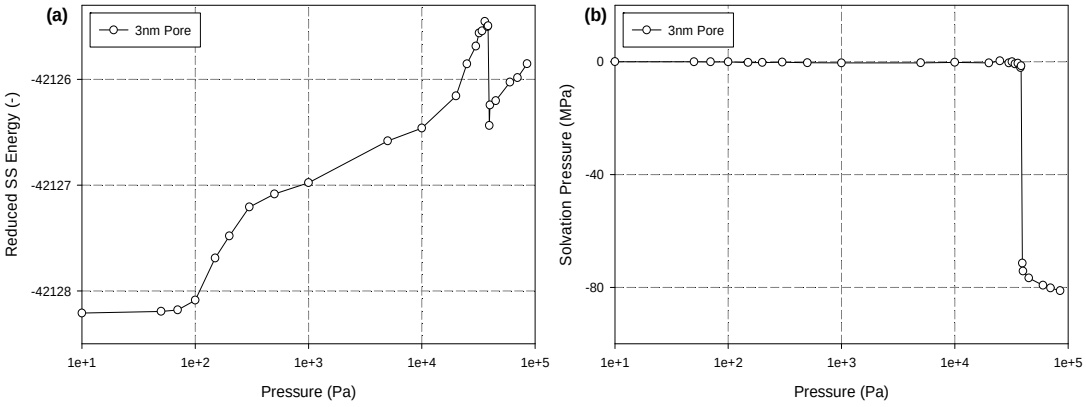

Figure 6.5 (a) The change in solid-solid (*SS*) Energy with bulk pressure, (b) the change in solvation pressure with bulk pressure for argon adsorption at 87 K in a slit pore of 3 nm initial width.

6.3.2. Effects of Pore Width

To investigate whether the pattern of deformation observed for the pore of 3 nm width remains valid for pores of different widths we made simulations for argon adsorption at 87 K in pores of various initial widths ranging from 2.5 to 3.4 nm.

Figure 6.6 shows the strain isotherms (change of the pore width with bulk pressure). The following observations are derived from this figure:

1. In the multilayer region, all the pores expand and the strain isotherms are identical, irrespective of the initial pore width. This confirms that at low loading, the pore walls behave like two independent graphite surfaces. In Appendix 4, the strain isotherms are plotted on semi-logarithm scales to illustrate the pattern of the strain more clearly in this region of the adsorption.
2. During capillary condensation all pores contract, but the extent of the contraction depends critically on the pore width. For pores in which the adsorbate packing is commensurate across the pore width at condensation, the contraction is minimal since any change in the pore size would alter the packing in such a way as to make the fluid-fluid interaction more repulsive. Pores of initial width 2.9 nm and 3.1 nm both give commensurate packing, but in the 3 nm pore the argon would be incommensurately packed if the pore remained rigid. Therefore the 3 nm deformable pore undergoes a contraction during adsorbate condensation to achieve a packing which minimises the combined contribution from the lowered *FF* interaction and the increased *SS* potential energy.
3. After completion of the capillary condensation the trend in deformation at the saturation vapour pressure (P_0) is different for pores of different initial widths as summarised in Table 6.1. Figure 6.7 illustrates these trends graphically as a function of the initial pore width. The oscillatory behaviour of the plot emphasises the importance of adsorbate packing during the capillary condensation and the subsequent pore filling.

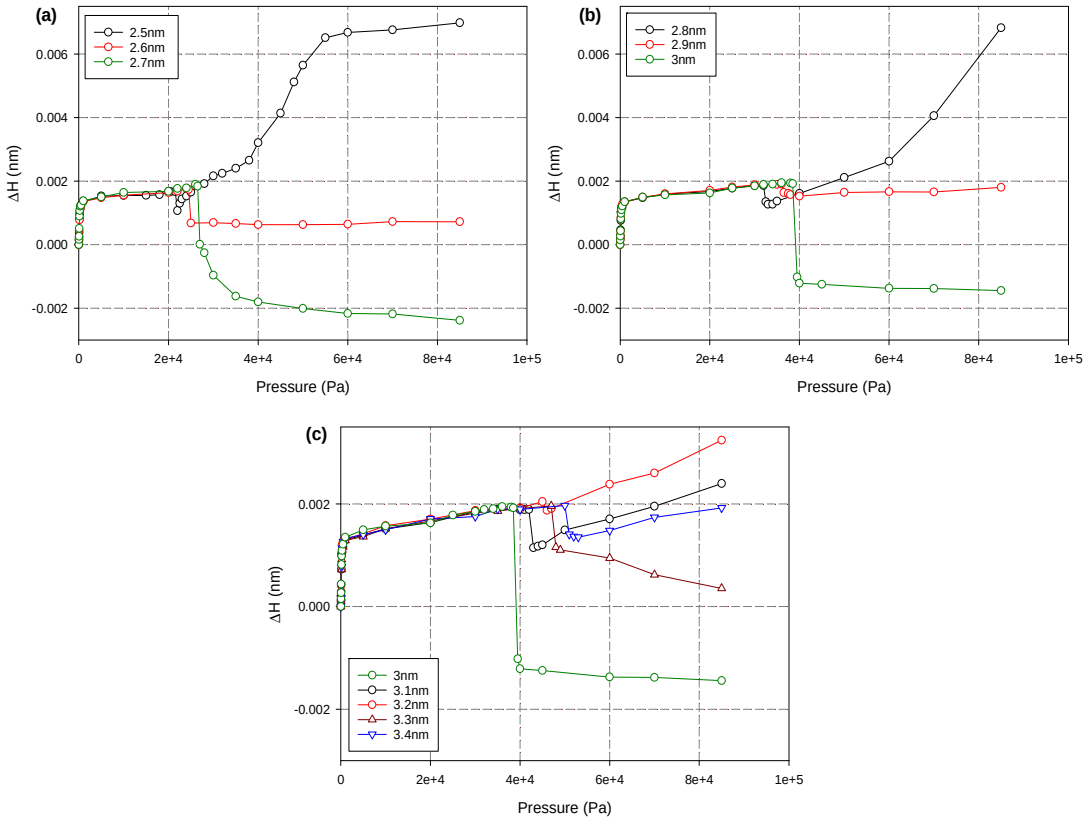

Figure 6.6 The strain isotherm for argon adsorption at 87 K in pores of length 20 nm with four movable layers and two fixed outermost layers and with different initial widths, (a) 2.5-2.7 nm, (b) 2.8-3 nm, (c) 3-3.4 nm.

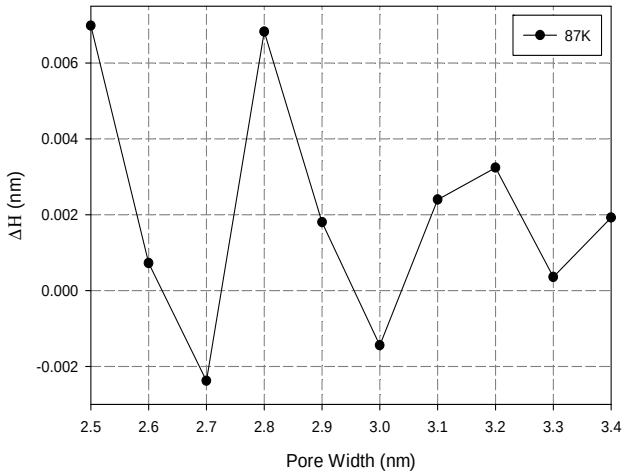

Figure 6.7 The change in pore width at saturation vapour pressure for argon adsorbed at 87 K in graphitic slit pores of 20 nm length with four movable graphene layers and two fixed outermost layers, as a function of the initial pore width.

Table 6.1 The deformation behaviour after capillary condensation of slit pores with different initial widths.

Initial pore width (nm)	Expansion (E) or Contraction (C)
2.5	E
2.6	-
2.7	C
2.8	E
2.9	-
3.0	C
3.1	E
3.2	E
3.3	C
3.4	E

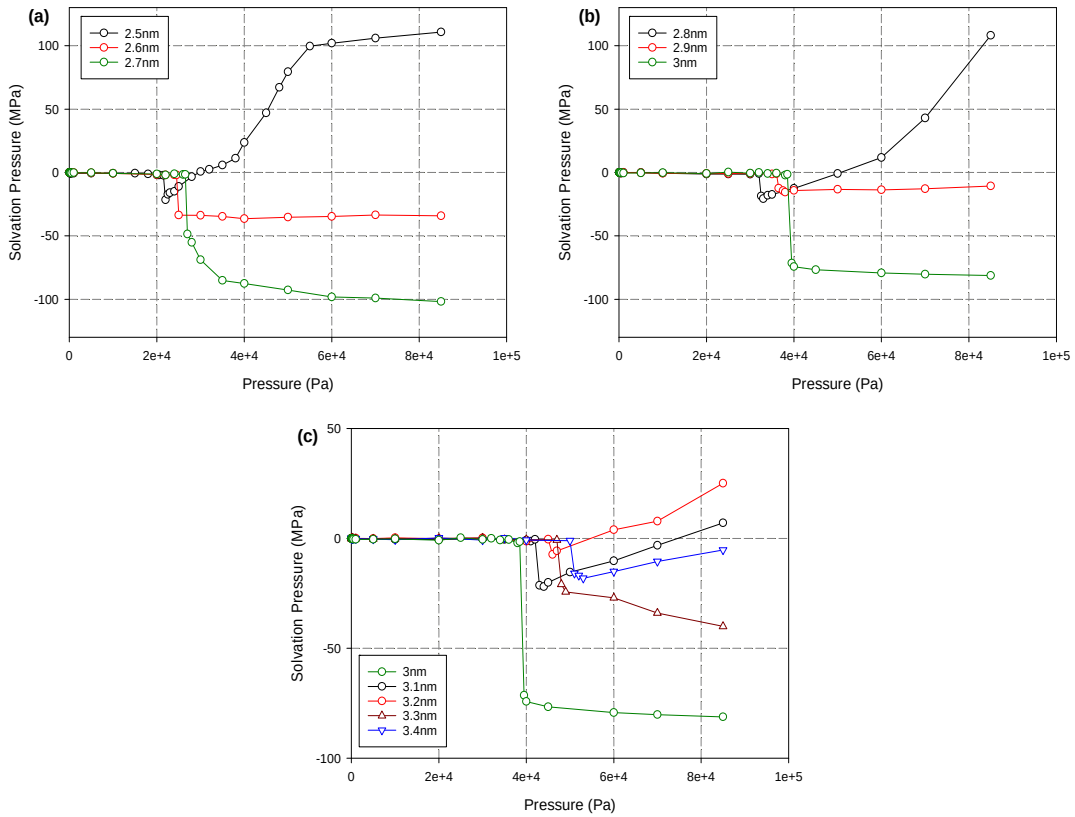

Figure 6.8 The variation in solvation pressure with bulk pressure for argon adsorption at 87 K in pores of length 20 nm with four movable layers and two fixed outermost layers and initial widths, (a) 2.5-2.7 nm, (b) 2.8-3 nm, (c) 3-3.4 nm.

As a further corroboration of our proposed deformation mechanism, we show that the solvation pressure is the driving force that is directly responsible for deformation. In Figures 6.8a to c, corresponding to the strain isotherms in Figures 6.6a to c, the solvation pressure is plotted against the bulk pressure. The complete match between the variation of the solvation pressure with pressure and the strain isotherm argues strongly that the solvation pressure is the driving force. The same conclusion was reached in our earlier work on micropores [251].

6.3.3. Effects of Temperature

The effects of thermal fluctuation on deformation were studied for temperatures in the range between 87 K and 100 K. Again, we take the 3 nm pore as an example since this is the one that shows the largest variation in expansion and contraction. Figures 6.9a and b show the strain isotherms plotted on linear and semi-logarithmic scales, respectively; a plot of the fractional change in the pore width with loading is shown in Figure 6.9c. Temperature has different effects on deformation at different stages in the adsorption process.

1. In the multilayer region, pore expansion is the same at a given loading regardless of the temperature. This suggests that fluctuations of the molecules in the first adsorbed layer are suppressed because of the strong *SF* interaction between the adsorbate layer and the graphite.
2. During the capillary condensation, the pore contracts sharply at all temperatures, but the contraction is less at higher temperatures.
3. After the capillary condensation, there are different patterns of deformation at different temperatures: there is a slight contraction at 87 K, but at higher temperatures, the pore expands and shows higher expansion at a given loading at higher temperatures (Figure 6.9c).

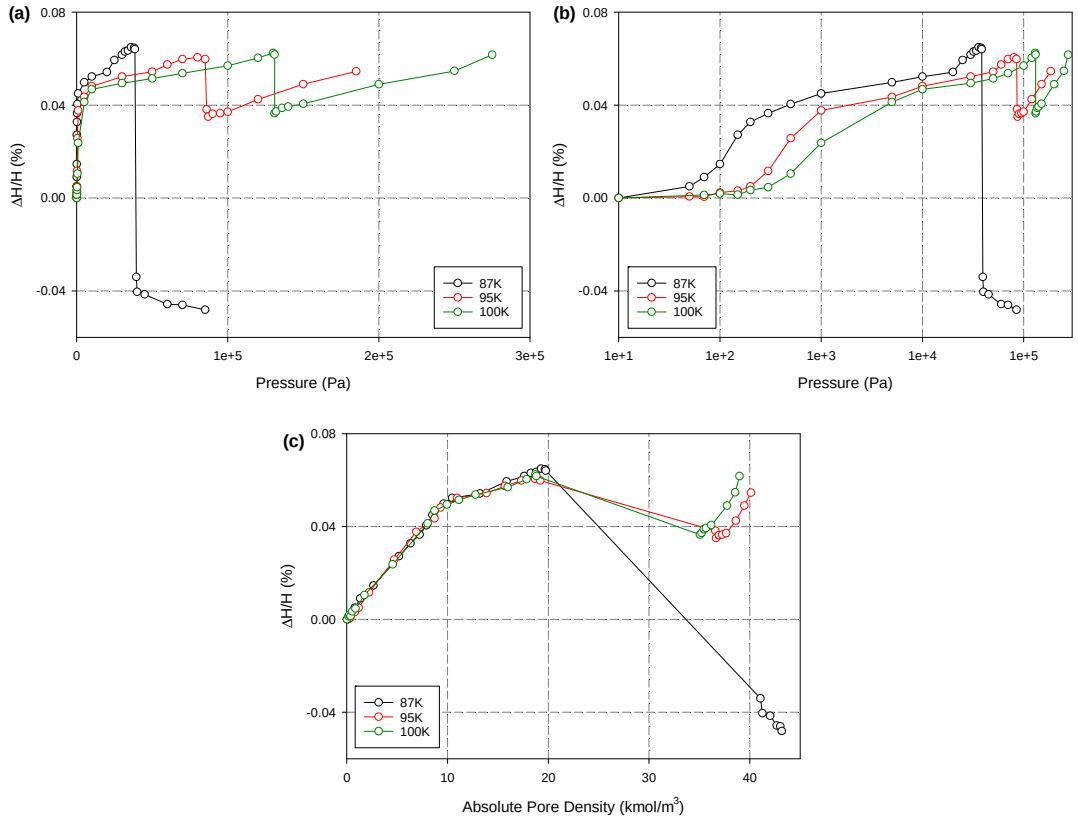

Figure 6.9 The strain isotherm for argon adsorption in a slit pore of 20 nm length and 3 nm initial width with four movable layers and two fixed outermost layers at different temperatures: (a) linear and (b) semi-logarithmic scales. (c) The fractional change of the pore width with loading.

6.3.4. Strain Hysteresis in Mesopores

The hysteresis in the adsorption-desorption isotherm and the strain isotherm are shown in Figures 6.10a and b for argon adsorption at 87 K in the 3 nm pore. The Type H1 hysteresis in the isotherm is typical for mesopores and the hysteresis observed in the strain isotherm occurs over the same pressure range as in the isotherm, suggesting that the hysteresis in the strain is a direct consequence of the hysteresis in the adsorption isotherm.

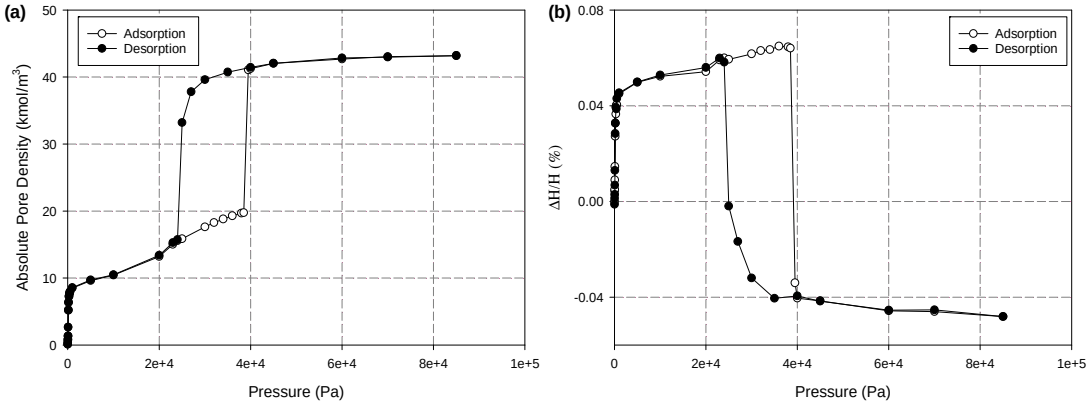

Figure 6.10 (a) The adsorption isotherm and (b) the strain isotherm for argon adsorption at 87 K in a slit pore of length 20 nm and 3 nm initial width with four movable layers and two fixed outermost layers.

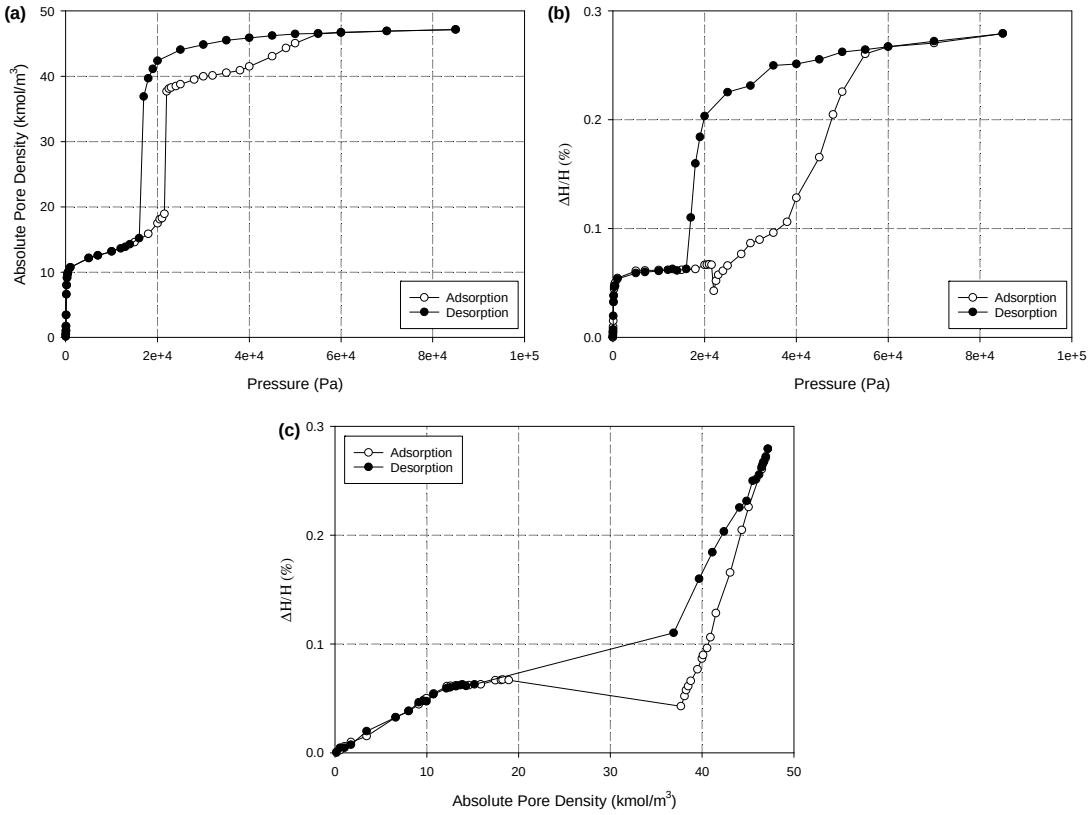

Figure 6.11 (a) The adsorption isotherm, (b) the strain isotherm and (c) the strain as a function of loading for argon adsorption at 87 K in a slit pore of length 20 nm and 3 nm initial width with four movable layers and two fixed outermost layers.

Deformation hysteresis also occurs in the other pores studied and shows quite interesting behaviour. The adsorption isotherm and the strain isotherm at 87 K for the 2.5 nm pore are shown in Figures 6.11a and b, respectively. Along the

adsorption branch, the pore contracts across the condensation, but to a much smaller extent than the 3 nm pore, and the pore width after this contraction is still greater than the initial width. Once the condensation has been completed, pore filling continues, resulting in pore expansion because of the increase in the solvation pressure. Upon desorption, the pore continuously contracts until the pore is emptied. The hysteresis is better described by plotting the percentage change in the pore width versus loading. For a given loading, the percentage change in width on desorption is greater than during adsorption, indicating that the condensate is more metastable in desorption than in adsorption.

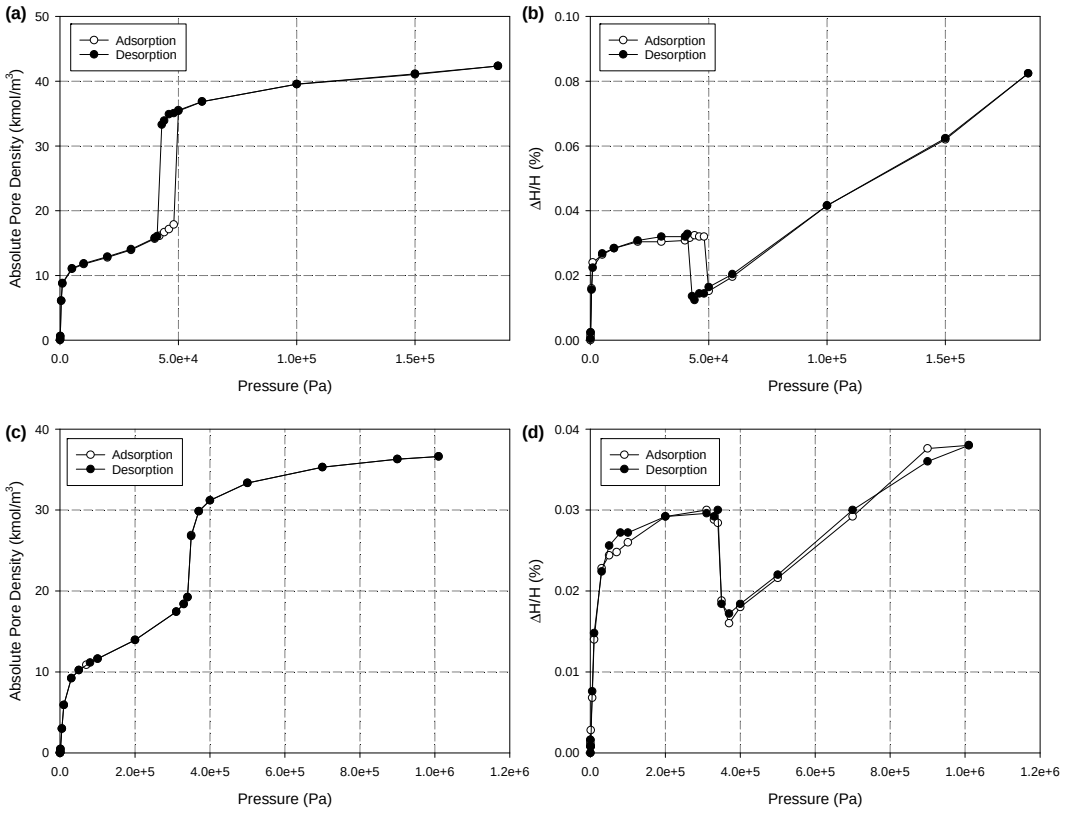

Figure 6.12 (a) The adsorption isotherm and (b) the strain isotherm at 95 K. (c) The adsorption isotherm and (d) the strain isotherm at 120 K for argon adsorption in a slit pore of 2.5 nm initial width; the pore length is 20 nm with four movable layers and two fixed outermost layers.

When the temperature is increased, both the adsorption isotherm and the strain isotherm for the 2.5 nm pore are different from the isotherms for the 3 nm pore, as shown in Figure 6.12 at 95 K and 120 K. Both the adsorption-desorption hysteresis and the deformation hysteresis evolve from a fused loop into a Type H1 hysteresis loop when the temperature is increased from 87 to 95 K. At 120 K, both the

adsorption-desorption isotherm and the strain isotherm are reversible, again highlighting the fact that the presence or absence of hysteresis in the strain isotherm is related directly to the adsorption isotherm. As the adsorption-desorption hysteresis at a given temperature shows the same behaviour for fixed and deformable pores, we suppose that they share the same mechanism for the disappearance of the hysteresis with increasing temperatures [252].

6.4. Conclusions

In this Chapter, we have studied the mechanisms of adsorption-induced deformation of an adsorbent solid in different stages of adsorption and desorption for argon at 87 K in deformable graphitic slit mesopores using grand canonical Monte Carlo simulations. In the multilayer region in a pore of width 3nm, the pore walls are slightly compressed (i.e. the pore expands) as the solid-fluid interaction increases. The pore walls behave as two independent surfaces at this stage and the extent of pore expansion is not affected by the changing the pore size within the range 2.5-3.4 nm or temperature up to 120 K. During the capillary condensation, the pore contracts sharply as attraction between the adsorbate molecules in the interior of the pore and the pore walls increases. Different amounts of pore contraction are observed when the pore width or temperature is varied. After completion of the capillary condensation, the pore can either expand or contract, depending on the whether the packing of the molecules across the pore width is commensurate or incommensurate, and their thermal motion. These factors determine the balance between attraction from molecules in the pore interior and the solid, and repulsion of molecules close to the surface. We find that strain is subject to hysteresis which closely follows the pattern of adsorption hysteresis.

Chapter 7. Conclusions and Recommendations

This thesis has presented a fundamental study of simple gas adsorption and adsorption-induced deformation in carbonaceous materials including both graphite and porous carbon. Monte Carlo simulation was conducted to obtain the behaviours of adsorption and adsorption-induced solid deformation that are comparable to experimental studies including the adsorption isotherm, the strain isotherm and the isosteric heat, as well as the relevant microscopic properties that facilitate the understanding of underlying mechanisms, such as the compressibility of the adsorbate, the solvation pressure, etc.

7.1. Conclusions

The first aim of this thesis is to study the adsorption and phase behaviours of simple gas on graphite surfaces. We chose the Kr-Graphite system and used *GCMC*, *C-kMC* and Mid-Density scheme as the simulation methods to investigate the *2D* phase transitions and hysteresis for Kr adsorption on a structureless graphite surface at temperatures below the triple point. The *GCMC* simulated adsorption isotherm shows qualitatively good agreement with the experimental data for Kr on a graphite surface at 77 K. The general step-wise behaviour in the first three layers of the experimental isotherm is reproduced by the simulations. The *2D* phase transitions (gas-solid, gas-liquid, liquid-solid, disordered-ordered solid) are observed at temperatures below the *2D* critical temperature. The critical temperature for the *2D* gas-liquid transition in the first layer is deduced between 86 and 88 K. Upon desorption, hysteresis is found for the first three layers at temperatures less than the corresponding *2D* hysteresis critical temperature. The existence of hysteresis is further confirmed by the presence of van der Waals loops in the canonical isotherm. There is a vertical segment in the unstable region of the van der Waals loop, which indicates the coexistence of two phases. This vertical segment in the canonical isotherm also overlaps with the equilibrium transition as determined by the Mid-Density scheme.

After the investigation of gas adsorption on graphite surfaces, we extended our study to adsorption in microporous solids with the simulation system of argon and graphitic slit micropores. We particularly looked into the order-disorder transitions and the restructuring of the adsorbate associated with the hysteresis loops. The

ordering transition is first order with a Type H1 hysteresis loop when the pore is infinitely long. However, the transition is second order in finite length pores and the hysteresis is entirely resulted from adsorbate restructuring. When a first order capillary condensation/evaporation is followed by an ordering transition, both mechanisms contribute to the hysteresis loop. The ratio of pore width to molecular size plays an important role in the ordering transition and there is no ordering hysteresis loop when the pore is incommensurate. The freezing temperature of the adsorbate is found to be a nonlinear function of the pore width and the contact layers could have different phase transitions compared with the inner layers.

Another aim of this thesis is to investigate the adsorption-induced solid deformation. We developed a deformable graphitic silt pore model of finite length as the model adsorbent and argon was used as the model adsorbate. The deformation behaviours of graphitic slit micropores were first studied, for which commensurate or incommensurate packing of the adsorbate molecules is particularly significant. The maximum density and the corresponding solvation pressure at the saturation vapour pressure oscillate synchronously with a damped amplitude as the initial pore width is increased from 0.65 to 2 nm. When the solvation pressure is zero at the saturation vapour pressure, the packing of the adsorbate in the pores is perfectly commensurate and these pores are called commensurate pores. We further found four categories of pore deformation, i.e. expansion of the 0.65 nm pore, contraction at all loadings, contraction followed by expansion and no deformation at the saturation vapour pressure for commensurate pores. Solvation pressure is found to be the driving force for the deformation and the local solvation pressure reveals how molecules at different locations of the pore contribute to the solvation pressure and deformation. Molecules near the pore walls have positive local solvation pressure and tend to contract the pore, while those in the interior have negative local solvation pressure and tend to contract the pore. At higher temperatures, the positive local solvation pressure is enhanced and pore expansion becomes more favoured. Packing effects are important under subcritical conditions and thermal fluctuations at supercritical conditions reduce molecular packing, and this reduction becomes greater when the pore size is increased. The pore length and number of movable layers also affect deformation, and the pore shows greater deformation in shorter pores or pores with more moveable layers.

We finally extended our study to the deformation of graphitic slit mesopores and found different deformation behaviours at different stages of adsorption. For pressures less than the condensation pressure, the pore walls are slightly compressed, which is brought about by the enhanced solid-fluid potential. This mechanism holds irrespective of pore size and temperature, because the pore walls behave like two independent surfaces at low loadings. However, at higher loadings during and after capillary condensation, the adsorbate molecules in the interior of the pore attract the pore walls while those close to the surface repulse the pore walls. The pore contracts during capillary condensation and with different extent with the variation of pore width and temperature. After capillary condensation, either pore expansion or contraction is observed as a function of pore width and temperature, indicating the important effects of packing and thermal fluctuations.

7.2. Recommendations

7.2.1. Ordering Transition in the Pore and Ordering Hysteresis

As shown in Chapter 4, we studied the ordering transition and the ordering hysteresis for argon adsorption in graphitic slit micropores. It is worthwhile to conduct more systematic and comprehensive simulation studies for different adsorbate, such as neon, krypton, methane and carbon dioxide, as well as different solid models.

7.2.2. Proper Model for Solid Deformation

The adsorption-induced solid deformation has been studied in Chapters 5 and 6. The deformable graphitic slit pore model has rather homogeneous surfaces. Therefore, we can develop more realistic solid models consisted of carbon atoms and further study the adsorption-induced solid deformation in more details with these solid models.

References

1. Rouquerol, F., et al., *1 - Introduction*, in *Adsorption by Powders and Porous Solids (Second Edition)*. 2014, Academic Press: Oxford. p. 1-24.
2. Gregg, S.J. and K.S.W. Sing, eds. *Adsorption, Surface Area and Porosity*. Second ed. 1982, Academic press INC.: New York.
3. Sing, K.S.W., et al., *Reporting physisorption data for gas/solid systems with special reference to the determination of surface area and porosity (Recommendations 1984).* Pure and Applied Chemistry 1985. **57**(4): p. 603-619.
4. Thommes, M., et al., *Physisorption of gases, with special reference to the evaluation of surface area and pore size distribution (IUPAC Technical Report)*, in *Pure and Applied Chemistry*. 2015. p. 1051-1069.
5. Langmuir, I., *The adsorption of gases on plane surfaces of glass, mica and platinum.* Journal of the American Chemical Society, 1918. **40**: p. 1361-1402.
6. Brunauer, S., P.H. Emmett, and T. Edward, *Adsorption of gases in multimolecular layers.* Journal of the American Chemical Society, 1938. **60**: p. 309-319.
7. Nicholson, D. and G. Parsonage, *Computer simulation and the statistical mechanics of adsorption*. 1982, London: Academic Press.
8. Frenkel, D. and B. Smit, *Understanding molecular simulation: from algorithms to applications.* Second ed. Computational Science Series, ed. D. Frenkel, et al. 2002, San Diego: Academic Press. 638.
9. Allen, M.P. and D.J. Tildesley *Computer Simulation of Liquids*. 1989, Oxford: Oxford University Press. xiii, 385.
10. Avgul, N.N. and A.V. Kiselev, *Physical adsorption of gases and vapous on graphitized carbon blacks.* Chemistry and Physics of Carbon, 1970. **6**: p. 1-124.
11. Alba-Simionesco, C., et al., *Effects of confinement on freezing and melting.* Journal of Physics: Condensed Matter, 2006. **18**(6): p. R15.
12. Long, Y., et al., *Under pressure: Quasi-high pressure effects in nanopores.* Microporous and Mesoporous Materials, 2012. **154**: p. 19-23.
13. Do, D.D., *Adsorption analysis: equilibria and kinetics*. 1998, London: Imperial College Press. xxi, 892.
14. Avgul, N.N., et al., *Heat of adsorption of hydrocarbons by carbon blacks of different degrees of graphitization.* Kolloidnyi Zhurnal, 1958. **20**: p. 298-304.
15. Bezus, A.G., V.P. Dreving, and A.V. Kiselev, *Isotherms and heats of adsorption of propane and propylene on graphitized carbon black - energy of adsorption forces.* Kolloidnyi Zhurnal, 1961. **23**(4): p. 328-334.
16. Kiselev, A.V., *Interaction energies in monolayers on solid surfaces. Heats of adsorption and adsorption equilibrium.* Russian Journal of Physical Chemistry, 1961. **35**(2): p. 111-123.
17. Kiselev, A.V., I. Akad, and K. Otd, *Adsorption and adsorption heat of ethylether, acetone and acetic acid vapors on graphitized carbon black (English).* 1961. **12**: p. 2116-2125.
18. Isirikyan, A.A. and A.V. Kiselev, *The absolute adsorption isotherms of vapors of nitrogen, benzene and n-hexane, and the heats of adsorption of benzene and n-hexane on graphitized carbon blacks. I. Graphitized thermal blacks.* The Journal of Physical Chemistry, 1961. **65**(4): p. 601-607.

19. Avgul, N.N., et al., *Isotherms and heats of adsorption on neopentane and carbon tetrachloride vapor on graphitized carbon black.* Izvestiya Akademii Nauk, Otdelenie Khtmicheskikh Nauk,, 1962. **5**: p. 769-777.
20. Isirikyan, A.A. and A.V. Kiselev, *Adsorption Isotherms of Nitrogen, Benzene and n-Hexane and the Heats of Adsorption of Benzene and n-Hexane on Graphitized Carbon Blacks. II. Adsorption on Graphitized Channel Blacks.* The Journal of Physical Chemistry, 1962. **66**(2): p. 205-209.
21. Fedorov, G.G., Y.A. Zarif'yants, and V.F. Kiselev, *Properties of the surface of freshly cleaved graphite. III. A temperature range of physical and chemical adsorption of oxygen on the surface of the fresh cleavage* Russian Journal of Physical Chemistry, 1963. **37**(10): p. 1267-1269.
22. Avgul, N.N., A.V. Kiselev, and I.A. Lygina, *Isotherms and Heats of Adsorption of Sphere-Like Molecules on Graphitized Carbon Black - Potential Energies and Chances in Thermodynamic Functions Upon Adsorption on Graphite.* Transactions of the Faraday Society, 1963. **59**(489): p. 2113-2127.
23. Isirikyan, A.A. and A.V. Kiselev, *Adsorption Isotherms of Nitrogen, Benzene and n-Hexane and the Heats of Adsorption of Benzene and n-Hexane on Graphitized Carbon Blacks. III. The Thermodynamic Characteristics of Adsorption Equilibria.* The Journal of Physical Chemistry, 1963. **66**(2): p. 210-215.
24. Isirikyan, A.A. and A.V. Kiselev, *Isotherms and Heats of Adsorption of Nitrogen, Benzene, and n-Hexane Vapours on Graphitised Carbon Blacks. III. Thermodynamic Quantities.* Russian Journal of Physical Chemistry, 1963. **37**(8): p. 957-961.
25. Kiselev, A.V. and M.V. Serdobov, *Heats of adsorption of benzene, carbon tetrachloride, methylcyclo-hexane, and perfluoromethylcyclo-hexane on a graphitised carbon black.* Russian Journal of Physical Chemistry, 1963. **37**(11): p. 1402-1404.
26. Bezus, A.G., V.P. Dreving, and A.V. Kiselev, *Isotherms and Heats of Adsorption of Methane on Graphitised Carbon Black.* Russian Journal of Physical Chemistry, 1964. **38**(12): p. 1589-1593.
27. Bezus, A.G., V.P. Dreving, and A.V. Kiselev, *Energy of adsorption of ethane and ethylene on different kinds of surfaces. 1 Isotherms and heats of adsorption of ethane on graphitized carbon black.* . Russian Journal of Physical Chemistry,Ussr, 1964. **38**: p. 30-35.
28. Aristov, B.G. and A.V. Kiselev, *Adsorption of Nitrogen and Argon Vapors on Non-specific Adsorbents Surfaces, Graphitized Carbon Black, Poly-ethylene, and Poly(tetrafluoroethylene).* Kolloidnyi Zhurnal, 1967. **29**(5): p. 631-637.
29. Bezus, A.G., V.P. Dreving, and A.V. Kiselev, *Variation with Pressure and Temperature of the Adsorption of Methane, Ethane, and Ethylene on Graphitised Carbon Black.* Russian Journal of Physical Chemistry, 1967. **41**(11): p. 1568-1572.
30. Beljakov, L.D., A.V. Kiselev, and N.V. Kovaleva, *Determination by Gas Chromatography of Adsorption Isotherms and Heats of Adsorption for Steam and Benzene on Graphitized Carbon Black.* Bulletin De La Societe Chimique De France, 1967(1): p. 285-289.
31. Belyakova, L.D., A.V. Kiselev, and N.V. Kovaleva, *Gas-Chromotographic Determination of Isotherms and Heats of Adsorption of Water, Benzene and*

Methanol Vapours on Graphitised Carbon Black. Russian Journal of Physical Chemistry, 1968. **42**(9): p. 1204-1208.

32. Avgul, N.N., et al., *Isotherms and differential heats of adsorption of methylcyclohexane and perpluoromethylcyclohexane on graphitised thermal black and dax zeolite crystals.* Russian Journal of Physical Chemistry,Ussr, 1968. **42**(7): p. 914-918.
33. Kiselev, A.V., I.A. Migunova, and Y.I. Yashin, *Absolute values of retention volumes and heats of adsorption of various molecules on graphitised carbon black.* Russian Journal of Physical Chemistry,Ussr, 1968. **42**(5): p. 644-646.
34. Berezin, G.I., A.V. Kiselev, and I.V. Kleshnin, *Heat Capacities of Alcohols Adsorbed on Graphitised Carbon Black.* Russian Journal of Physical Chemistry, 1969. **43**(11): p. 1657-1658.
35. Berezin, G.I., et al., *Heat of Adsorption of Carbon Tetrachloride on a Graphitised Carbon Black Above and Below Two-Dimensional Critical Temperature.* Russian Journal of Physical Chemistry, 1969. **43**(1): p. 118.
36. Berezin, G.I., et al., *Heat Capacities of Ethyl and Tertiary Butyl Alcohols in Adsorption Layers on Graphitised Carbon Black.* Russian Journal of Physical Chemistry, 1969. **43**(6): p. 894-696.
37. Berezin, G.I. and A.V. Kiselev, *Variation of Heats of Adsorption and Heat Capacity of Adsorbate with Surface Coverage. III. Non-Localised Polymolecular Adsorption.* Russian Journal of Physical Chemistry, 1969. **43**(5): p. 683-686.
38. Berezin, G.I., A.V. Kiselev, and V.A. Sinitsyn, *Adsorption of Benzene and n-Hexane on Graphitised Carbon Black.* Russian Journal of Physical Chemistry, 1970. **44**(3): p. 408-411.
39. Berezin, G.I., et al., *Heat Capacity of n-Propyl Alcohol Adsorbed on Graphitised Thermal Black.* Russian Journal of Physical Chemistry, 1970. **44**(2): p. 292-293.
40. Berezin, G.I., et al., *Adsorption of Ethanol on Surface of Graphitized Carbon Black at Different Temperatures.* Russian Journal of Physical Chemistry, 1972. **46**(3): p. 432-433.
41. Derkaui, A., A.V. Kiselev, and B.V. Kuznetsov, *Calorimetric Measurement of Heats of Vapor Adsorption on Graphitized Thermal Carbon Black.* Journal of the Chemical Society-Faraday Transactions I, 1985. **81**: p. 1685-1692.
42. Thomy, A. and X. Duval, *Adsorption of simple molecules on graphite. I. Homogeneity of the surface of oxfoliated graphite. Origin and complexity of adsorption isotherms.* J. Chim. Phys. Physicochim. Biol., 1969. **66**(11-12): p. 1966.
43. Thomy, A. and X. Duval, *Adsorption Of Simple Molecules On Graphite. 2. Variation Of Adsorption Potential As Function Of Number Of Adsorbed Layers.* Journal De Chimie Physique Et De Physico-Chimie Biologique, 1970. **67**(2): p. 286-290.
44. Thomy, A. and X. Duval, *Adsorption of Simple Molecules on Graphite. 3. Passage of First Layer by Three Sucessive States.* Journal De Chimie Physique Et De Physico-Chimie Biologique, 1970. **67**(6): p. 1101-1110.
45. Thomy, A. and X. Duval, *Adsorption of simple molecules on graphite. 1. Homogeneity of stripped graphite surface. Origin and complexity of adsorption isotherms.* Journal De Chimie Physique Et De Physico-Chimie Biologique, 1970. **66**(11-1): p. 1966-1973.

46. Thomy, A., et al., *Different steps in the formation of a rare gas or methane adsorbed film on a uniform surface of graphite.* Journal of Crystal Growth, 1971. **13**: p. 159-163.
47. Duval, X. and A. Thomy, *The interpretation of Krypton adsorption isotherms on exfoliated graphite.* Carbon, 1975. **13**(3): p. 242-243.
48. Regnier, J., A. Thomy, and X. Duval, *Adsorption of rare gases on graphite. Structure and density of the first adsorbed layer after its solidification.* Journal De Chimie Physique Et De Physico-Chimie Biologique, 1977. **74**(9): p. 926-931.
49. Menaucourt, J., A. Thomy, and X. Duval, *Variation in temperature function of the number of adsorbed ethylene layers on the cleavage faces of graphite.* J. Phys. (Paris), Colloq., 1977(4): p. 195-200.
50. Thomy, A., X. Duval, and J. Regnier, *Two-dimensional phase transitions as displayed by adsorption isotherms on graphite and other lamellar solids.* Surface Science Reports, 1981. **1**(1): p. 1-38.
51. Thomy, A., et al., *Developments in the study of two-dimensional phase transitions during the last decade*, in *Studies in Surface Science and Catalysis*. 1982, Elsevier. p. 411-420.
52. Bah, A., N. DupontPavlovsky, and X. Duval, *Adsorption Hysteresis and 2D Phase Nucleation of Chloroform on Graphite.* Surface Science, 1996. **352**: p. 518-522.
53. Madih-Ayadi, K., et al., *Methane adsorption on dichloromethane preplated graphite: 2D phase transitions on dual surfaces.* Surface Science, 1998. **402-404**: p. 836-840.
54. Beebe, R.A. and D.M. Young, *Heats of adsorption of argon on a series of carbon blacks graphitized at successively higher temperatures.* The Journal of Physical Chemistry, 1954. **58**(1): p. 93-96.
55. Beebe, R.A. and R.M. Dell, *Heats of adsorption of polar molecules on carbon surfaces. 1. Sulfur dioxide.* Journal of Physical Chemistry, 1955. **59**(8): p. 746-754.
56. Dell, R.M. and R.A. Beebe, *Heats of adsorption of polar molecules on carbon surfaces. 2. Ammonia and methylamine.* Journal of Physical Chemistry, 1955. **59**(8): p. 754-762.
57. Amberg, C.H., W.B. Spencer, and R.A. Beebe, *Heats of adsorption of Krypton on highly graphitized carbon black.* Canadian Journal of Chemistry-Revue Canadienne De Chimie, 1955. **33**(2): p. 305-313.
58. Holmes, J.M. and R.A. Beebe, *An example of desorption hysteresis at low relative pressure on a non-porous adsorbent - Ammonia on graphitized carbon black.* Journal of Physical Chemistry, 1957. **61**(12): p. 1684-1686.
59. Spencer, W.B., C.H. Amberg, and R.A. Beebe, *Further studies of adsorption on graphitized carbon blacks.* Journal of Physical Chemistry, 1958. **62**(6): p. 719-723.
60. Piper, J. and J.A. Morrison, *Heats of adsorption and vibrational frequencies for xenon adsorbed on graphite.* Chemical Physics Letters, 1984. **103**(4): p. 323-327.
61. Piper, J. and J.A. Morrison, *Heats of Adsorption of Methane Multilayers on Graphite.* Physical Review B, 1984. **30**(6): p. 3486-3488.
62. Piper, J., J.A. Morrison, and C. Peters, *The adsorption of carbon monoxide on graphite.* Molecular Physics, 1984. **53**(6): p. 1463-1480.

63. Inaba, A. and J.A. Morrison, *Ethylene on graphite: Heats of adsorption and phase diagram.* Phys. Rev. B, 1986. **34**(5): p. 3238-3242.
64. Inaba, A., Y. Koga, and J.A. Morrison, *Multilayers of Methane Adsorbed on Graphite.* Journal of the Chemical Society-Faraday Transactions II, 1986. **82**: p. 1635-1646.
65. Peters, C., J.A. Morrison, and M.L. Klein, *The adsorption of acetylene on a graphite surface.* Surface Science, 1986. **165**(2-3): p. 355-374.
66. Inaba, A. and J.A. Morrison, *The wetting transition and adsorption/desorption hysteresis for the CH4/graphite system.* Chemical Physics Letters, 1986. **124**(4): p. 361-364.
67. Inaba, A., J.A. Morrison, and J.M. Telefer, *Critical wetting of graphite by krypton and xenon.* Molecular Physics, 1987. **62**(4): p. 961-969.
68. Meichel, T., et al., *Adsorption of ethylene on graphite near saturation wetting transition capillary condensation.* Langmuir, 1990. **6**(10): p. 1579-1584.
69. Rouquerol, J., S. Partyka, and F. Rouquerol, *Calorimetric evidence for a bidimensional phase-change in monolayer of nitrogen or argon adsorbed on graphite at 77K.* Journal of the Chemical Society-Faraday Transactions I, 1977. **73**: p. 306-314.
70. Grillet, Y., F. Rouquerol, and J. Rouquerol, *Two-dimensional freezing of nitrogen or argon on differently graphitized carbons.* Journal of Colloid and Interface Science, 1979. **70**(2): p. 239-244.
71. Suzanne, J., J. Rouquerol, and K.S.W. Sing, *Phase Transitions, Dynamics and Orientational Ordering in Hydrocarbon Molecules Adsorbed on Graphite*, in *Studies in Surface Science and Catalysis*. 1982, Elsevier. p. 421-438.
72. Ross, S. and W. Winkler, *On physical adsorption: IX. Sub-critical and subpracritical adsorption isotherms for krypton monolayers on graphitized carbon black.* Journal of Colloid Science, 1955. **10**(4): p. 330-337.
73. Ross, S. and W. Winkler, *On physical adsorption: VIII. Monolayer adsorption of argon and nitrogen on graphitized carbon.* Journal of Colloid Science, 1955. **10**(4): p. 319-329.
74. Ross, S. and W.W. Pultz, *On physical adsorption: X. Adsorbed monolayers of argon and nitrogen on boron nitride and on a graded series of partially graphitized carbon blacks.* Journal of Colloid Science, 1958. **13**(4): p. 397-406.
75. Steele, W.A. and R. Karl, *Two-dimensional critical behavior of rare gases adsorbed on graphitized carbon black.* Journal of Colloid and Interface Science, 1968. **28**(3-4): p. 397-402.
76. Rayment, T., et al., *The Structure and Properties of Methane Adsorbed on Graphitized Carbon Black Determined by Neutron Diffraction.* Molecular Physics, 1981. **43**(3): p. 601-620.
77. Piper, J., et al., *Heats and Entropies of Adsorption of N_2 on Grafoil at 79.3K.* Journal of the Chemical Society-Faraday Transactions I, 1983. **79**: p. 2863-2874.
78. Kosugi, T., Y. Usui, and I. Arakawa. *Adsorption-Desorption Hysteresis in the Adsorption-Isotherms for Kr and Xe on Exfoliated Graphite*. 1992. The Hague, Netherlands.
79. Ustinov, E.A. and D.D. Do, *Two-dimensional order-disorder transition of argon monolayer adsorbed on graphitized carbon black: Kinetic Monte Carlo method.* J. Chem. Phys., 2012. **136**: p. 134702/1-134702/10.

80. Ustinov, E. and D. Do, *Simulation study of two-dimensional phase transitions of argon on graphite surface and in slit micropores.* Adsorption, 2014. **20**(2-3): p. 439-451.
81. Ustinov, E.A., *Improved modeling of two-dimensional transitions in dense phases on crystalline surfaces. Krypton–graphite system.* The Journal of Chemical Physics, 2015. **142**(7): p. 074701/1-074701/10.
82. Phadungbut, P., et al., *On the phase transition in a monolayer adsorbed on graphite at temperatures below the 2D-critical temperature.* Molecular Simulation, 2014. **41**(5-6): p. 446-454.
83. Wongkoblap, A. and D.D. Do, *Explanation of the unusual peak of calorimetric heat in the adsorption of nitrogen, argon and methane on graphitized thermal carbon black.* Physical Chemistry Chemical Physics, 2008. **10**: p. 1106-1113.
84. Fan, C., et al., *On the identification of the sharp spike in the heat curve for argon, nitrogen, and methane adsorption on graphite: Reconciliation between computer simulation and experiments.* The Journal of Physical Chemistry C, 2012. **116**(1): p. 953-962.
85. Dubinin, M.M., *Physical adsorption of gases and vapors in micropores.* Progress in Surface and Membrane Science, 1975. **9**: p. 1-70.
86. Peterson, B.K., J.P.R.B. Waltont, and K.E. Gubbins, *Fluid Behaviour in Narrow Pores.* Journal of the Chemical Society, Faraday Transactions, 1986. **2**(82): p. 1789-1800.
87. Gubbins, K.E., *Molecular adsorption in micropores.* Chem. Eng. Prog., 1990. **86**(8): p. 42-44.
88. Jiang, S., C.L. Rhykerd, and K.E. Gubbins, *Layering, freezing transitions, capillary condensation and diffusion of methane in slit carbon pores.* Molecular Physics, 1993. **79**(2): p. 373-391.
89. Müller, E.A., et al., *Adsorption of Water on Activated Carbons: A Molecular Simulation Study.* Journal of Physical Chemistry, 1996. **100**(4): p. 1189-1196.
90. Radhakrishnan, R., et al., *Freezing of simple fluids in microporous activated carbon fibers. Comparison of simulation and experiment.* J. Chem. Phys., 1999. **111**(19): p. 9058-9067.
91. Coasne, B., et al., *Freezing of argon in ordered and disordered porous carbon.* Physical Review B, 2007. **76**(8): p. 085416/1-085416/10.
92. Coasne, B., et al., *Effect of Pressure on the Freezing of Pure Fluids and Mixtures Confined in Nanopores†.* The Journal of Physical Chemistry B, 2009. **113**(42): p. 13874-13881.
93. Jazdzewska, M., et al., *Novel ice structures in carbon nanopores: pressure enhancement effect of confinement.* Phys Chem Chem Phys, 2011. **13**(19): p. 9008-9013.
94. Gelb, L.D., et al., *Phase separation in confined systems.* Reports on Progress in Physics, 1999. **62**(12): p. 1573-1659.
95. Watanabe, A., T. Iiyama, and K. Kaneko, *Melting temperature elevation of benzene confined in graphitic micropores.* Chemical Physics Letters, 1999. **305**(1-2): p. 71-74.
96. Kaneko, K., et al., *A Remarkable Elevation of Freezing Temperature of CCl4 in Graphitic Micropores.* The Journal of Physical Chemistry B, 1999. **103**(34): p. 7061-7063.

97. Vishnyakov, A. and A.V. Neimark, *Specifics of freezing of Lennard-Jones fluid confined to molecularly thin layers.* Journal of Chemical Physics, 2003. **118**(16): p. 7585-7598.
98. Kanda, H. and M. Miyahara, *Freezing of Lennard-Jones fluid in cylindrical nanopores under tensile conditions.* Adsorption, 2007. **13**(3-4): p. 191-195.
99. Ustinov, E.A. and D.D. Do, *Simulation of gas adsorption on a surface and in slit pores with grand canonical and canonical kinetic Monte Carlo methods.* Physical Chemistry Chemical Physics, 2012. **14**(31): p. 11112-11118.
100. Miyahara, M., et al., *Solid-liquid phase transition of Lennard-Jones fluid in slit pores under tensile condition.* Journal of Chemical Physics, 2000. **112**(22): p. 9909-9916.
101. Miyahara, M. and K.E. Gubbins, *Freezing/melting phenomena for Lennard-Jones methane in slit pores: A Monte Carlo study.* The Journal of Chemical Physics, 1997. **106**(7): p. 2865-2880.
102. Morishige, K., H. Fujii, and D. Kinukawa, *Capillary Critical Point of Argon, Nitrogen, Oxygen, Ethylene, and Carbon Dioxide in MCM-41.* Langmuir, 1997. **13**(13): p. 3494-3498.
103. Morishige, K. and M. Shikimi, *Adsorption hysteresis and pore critical temperature in a single cylindrical pore.* Journal of Chemical Physics, 1998. **108**(18): p. 7821-7824.
104. Morishige, K. and M. Ito, *Capillary condensation of nitrogen in MCM-41 and SBA-15.* Journal of Chemical Physics, 2002. **117**(17): p. 8036-8041.
105. Morishige, K. and N. Tateishi, *Adsorption hysteresis in ink-bottle pore.* Journal of Chemical Physics, 2003. **119**(4): p. 2301-2306.
106. Morishige, K., N. Tateishi, and S. Fukuma, *Capillary condensation of nitrogen in MCM-48 and SBA-16.* J. Phys. Chem. B, 2003. **107**(22): p. 5177-5181.
107. Morishige, K. and Y. Nakamura, *Nature of Adsorption and Desorption Branches in Cylindrical Pores.* Langmuir, 2004. **20**(11): p. 4503-4506.
108. Morishige, K. and N. Tarui, *Capillary Condensation of Nitrogen in Ordered Mesoporous Silica with Bicontinuous Gyroid Structure.* J. Phys. Chem. C, 2007. **111**(1): p. 280-285.
109. Morishige, K., *Adsorption hysteresis in ordered mesoporous silicas.* Adsorption, 2008(14): p. 157-163.
110. Morishige, K., *Capillary condensation in ordered mesoporous materials.* Zeoraito, 2008. **25**(2): p. 51-58.
111. Morishige, K., *Hysteresis Critical Point of Nitrogen in Porous Glass: Occurrence of Sample Spanning Transition in Capillary Condensation.* Langmuir, 2009. **25**(11): p. 6221-6226.
112. Morishige, K. and K. Yoshida, *Neck Size of Ordered Cage-Type Mesoporous Silica FDU-12 and Origin of Gradual Desorption.* The Journal of Physical Chemistry C, 2010. **114**(15): p. 7095-7101.
113. Neimark, A.V., P.I. Ravikovitch, and A. Vishnyakov, *Adsorption hysteresis in nanopores.* Physical Review E, 2000. **62**(2): p. 1493-1496.
114. Neimark, A.V., P.I. Ravikovitch, and A. Vishnyakov. *Molecular approach to adsorption hysteresis*. 2000. World Scientific Publishing Co. Pte. Ltd.
115. Neimark, A.V. and P.I. Ravikovitch, *Capillary condensation in MMS and pore structure characterization.* Microporous and Mesoporous Materials, 2001. **44-45**: p. 697-707.

116. Kornev, K.G., I.K. Shingareva, and A.V. Neimark, *Capillary condensation as a morphological transition.* Advances in Colloid and Interface Science, 2002. **96**(1-3): p. 143-167.
117. Ravikovitch, P.I. and A.V. Neimark, *Experimental Confirmation of Different Mechanisms of Evaporation from Ink-Bottle Type Pores: Equilibrium, Pore Blocking, and Cavitation.* Langmuir, 2002. **18**(25): p. 9830-9837.
118. Ravikovitch, P.I. and A.V. Neimark, *Density Functional Theory of Adsorption in Spherical Cavities and Pore Size Characterization of Templated Nanoporous Silicas with Cubic and Three-Dimensional Hexagonal Structures.* Langmuir, 2002. **18**(5): p. 1550-1560.
119. Vishnyakov, A. and A.V. Neimark, *Monte Carlo simulation test of pore blocking effects.* Langmuir, 2003. **19**(8): p. 3240-3247.
120. Thommes, M., et al., *Adsorption Hysteresis of Nitrogen and Argon in Pore Networks and Characterization of Novel Micro- and Mesoporous Silicas.* Langmuir, 2006. **22**(2): p. 756-764.
121. Ravikovitch, P.I., et al., *Characterization of micro-mesoporous materials from nitrogen and toluene adsorption: Experiment and modeling.* Langmuir, 2006. **22**(2): p. 513-516.
122. Muroyama, N., et al., *Argon Adsorption on MCM-41 Mesoporous Crystal Studied by In Situ Synchrotron Powder X-ray Diffraction.* Journal of Physical Chemistry C, 2008. **112**(29): p. 10803-10813.
123. Cychosz, K.A., et al., *Characterization of the Pore Structure of Three-Dimensionally Ordered Mesoporous Carbons Using High Resolution Gas Sorption.* Langmuir, 2012. **28**: p. 12647-12654.
124. Gor, G.Y., C.J. Rasmussen, and A.V. Neimark, *Capillary Condensation Hysteresis in Overlapping Spherical Pores: A Monte Carlo Simulation Study.* Langmuir, 2012. **28**(33): p. 12100-12107.
125. Maddox, M.W., J.P. Olivier, and K.E. Gubbins, *Characterization of MCM-41 using molecular simulation: Heterogeneity effects.* Langmuir, 1997. **13**(6): p. 1737-1745.
126. Liu, B., W. Wang, and X. Zhang, *A hybrid cylindrical model for characterization of MCM-41 by density functional theory.* Physical Chemistry Chemical Physics, 2004. **6**(15): p. 3985-3990.
127. Coasne, B., K.E. Gubbins, and R.J.M. Pellenq, *A Grand Canonical Monte Carlo Study of Adsorption and Capillary Phenomena in Nanopores of Various Morphologies and Topologies: Testing the BET and BJH Characterization Methods.* Particle & Particle Systems Characterization, 2004. **21**(2): p. 149-160.
128. Coasne, B., et al., *Adsorption of Simple Gases in MCM-41 Materials: The Role of Surface Roughness.* Langmuir, 2006. **22**(1): p. 194-202.
129. Hung, F.R., et al., *Argon and krypton adsorption on templated mesoporous silicas: molecular simulation and experiment.* Adsorption, 2007. **13**(5-6): p. 425-437.
130. Rocken, P. and P. Tarazona, *Capillary condensation in structured pores.* Journal of Chemical Physics, 1996. **105**(5): p. 2034-2043.
131. Thommes, M., R. Koehn, and M. Froeba, *Sorption and Pore Condensation Behavior of Nitrogen, Argon, and Krypton in Mesoporous MCM-48 Silica Materials.* J. Phys. Chem. B, 2000. **104**(33): p. 7932-7943.

132. Thommes, M., R. Koehn, and M. Froeba, *Sorption and pore condensation behavior of pure fluids in mesoporous MCM-48 silica, MCM-41 silica and controlled pore glass.* Stud. Surf. Sci. Catal., 2001. **135**: p. 2893-2901.
133. Thommes, M., R. Koehn, and M. Froeba, *Pore condensation and hysteresis phenomena in mesoporous molecular sieves*, in *Studies in Surface Science and Catalysis* 2002, Elsevier. p. 1965-1702.
134. Thommes, M., et al., *Characterization of mesoporous solids: Pore condensation and sorption hysteresis phenomena in mesoporous molecular sieves*, in *Studies in Surface Science and Catalysis*. 2002, Elsevier. p. 1695-1702.
135. Thommes, M., R. Kohn, and M. Froba, *Sorption and pore condensation behavior of pure fluids in mesoporous MCM-48 silica, MCM-41 silica, SBA-15 silica and controlled-pore glass at temperatures above and below the bulk triple point.* Applied Surface Science, 2002. **196**(1-4): p. 239-249.
136. Thommes, M., *Physical adsorption characterization of ordered and amorphous mesoporous materials.*, in *Nanoporous Materials, Science & Engineering* G. Lu and X.S. Zhao, Editors. 2004, Imperial College Press: New Jersey. p. 317-364.
137. Kleitz, F., et al., *Probing Adsorption, Pore Condensation, and Hysteresis Behavior of Pure Fluids in Three-Dimensional Cubic Mesoporous KIT-6 Silica.* The Journal of Physical Chemistry C, 2010. **114**(20): p. 9344-9355.
138. Thommes, M., *Physical adsorption characterization of nanoporous materials.* Chem. Ing. Tech., 2010. **82**: p. 1059-1073.
139. Thommes, M., *Recent advances in the characterization of mesoporous materials by physical adsorption.* Annu. Rev. Nano Res., 2010. **3**: p. 515-555.
140. Rasmussen, C.J., et al., *Cavitation in Metastable Liquid Nitrogen Confined to Nanoscale Pores.* Langmuir, 2010. **26**(12): p. 10147-10157.
141. Kruk, M., et al., *Characterization of High-Quality MCM-48 and SBA-1 Mesoporous Silicas.* Chemistry of Materials, 1999. **11**(9): p. 2568-2572.
142. Kruk, M., et al., *Characterization of Highly Ordered MCM-41 Silicas Using X-ray Diffraction and Nitrogen Adsorption.* Langmuir, 1999. **15**(16): p. 5279-5284.
143. Kruk, M., et al., *Characterization of the porous structure of SBA-15.* Chemistry of Materials, 2000. **12**(7): p. 1961-1968.
144. Kruk, M. and M. Jaroniec, *Argon adsorption at 77 K as a useful tool for the elucidation of pore connectivity in ordered materials with large cagelike mesopores.* Chemistry of Materials, 2003. **15**(15): p. 2942-2949.
145. Kruk, M., J.R. Matos, and M. Jaroniec, *Argon and nitrogen adsorption studies of changes in connectivity of ordered cage-like large mesopores during the hydrothermal treatment.* Colloids and Surfaces A: Physicochemical and Engineering Aspects, 2004. **241**(1-3): p. 27-34.
146. Mason, G., *The Effect of Pore-Space Connectivity on the Hysteresis of Capillary Condensation in Adsorption Desorption Isotherms.* Journal of Colloid and Interface Science, 1982. **88**: p. 36-46.
147. Mason, G., *A Model of Adsorption-Desorption Hysteresis in Which Hysteresis is Primarily Developed by the Interconnections in a Network of Pores.* Proceedings of the Royal Society of London Series A-Mathematical Physical and Engineering Sciences, 1983. **390**: p. 47-72.

148. Libby, B. and P.A. Monson, *Adsorption/Desorption Hysteresis in Inkbottle Pores: A Density Functional Theory and Monte Carlo Simulation Study.* Langmuir, 2004. **20**(10): p. 4289-4294.
149. Monson, P.A., *Recent progress in molecular modeling of adsorption and hysteresis in mesoporous materials.* Adsorption, 2005. **11**: p. 29-35.
150. Monson, P.A., *Contact Angles, Pore Condensation, and Hysteresis: Insights from a Simple Molecular Model.* Langmuir, 2008. **24**(21): p. 12295-12302.
151. Naumov, S., et al., *Understanding capillary condensation and hysteresis in porous silicon: Network effects within independent pores.* Physical Review E, 2008. **78**(6): p. 060601/1-060601/4.
152. Naumov, S., et al., *Understanding adsorption and desorption processes in mesoporous materials with independent disordered channels.* Physical Review E, 2009. **80**(3): p. 031607/1-031607/9.
153. Monson, P.A., *Understanding adsorption/desorption hysteresis for fluids in mesoporous materials using simple molecular models and classical density functional theory.* Microporous and Mesoporous Materials, 2012. **160**: p. 47-66.
154. Nguyen, P.T.M., D.D. Do, and D. Nicholson, *On the Cavitation and Pore Blocking in Cylindrical Pores with Simple Connectivity.* The Journal of Physical Chemistry B, 2011. **115**(42): p. 12160-12172.
155. Nguyen, P.T.M., D.D. Do, and D. Nicholson, *On the Hysteresis Loop of Argon Adsorption in Cylindrical Pores.* The Journal of Physical Chemistry C, 2011. **115**(11): p. 4706-4720.
156. Nguyen, P.T.M., et al., *On the Cavitation-Like Pore Blocking in Ink-Bottle Pore: Evolution of Hysteresis Loop with Neck Size.* The Journal of Physical Chemistry C, 2013. **117**(10): p. 5475-5484.
157. Nguyen, P.T.M., D.D. Do, and D. Nicholson, *Pore connectivity and hysteresis in gas adsorption: A simple three-pore model.* Colloids and Surfaces A: Physicochemical and Engineering Aspects, 2013. **437**: p. 56-68.
158. Cohan, L.H., *Sorption hysteresis and the vapor pressure of concave surfaces.* Journal of the American Chemical Society, 1938. **60**: p. 433-435.
159. McBain, J.W., *An explanation of hysteresis in the hydration and dehydration of gels.* Journal of the American Chemical Society, 1935. **57**(1): p. 699-700.
160. De Boer, J.H., *The structure and texture of a physical adsorbent.* Colloques Internationaus du CNRS, 1972. **201**: p. 407-434.
161. Horikawa, T., D.D. Do, and D. Nicholson, *Capillary condensation of adsorbates in porous materials.* Advances in Colloid and Interface Science, 2011. **169**(1): p. 40-58.
162. Neimark, A.V. and A. Vishnyakov, *Gauge cell method for simulation studies of phase transitions in confined systems.* Physical Review E, 2000. **62**(4): p. 4611-4622.
163. Liu, Z., D.D. Do, and D. Nicholson, *A thermodynamic study of the mid-density scheme to determine the equilibrium phase transition in cylindrical pores.* Molecular Simulation, 2011: p. 1-11.
164. Liu, Z., et al., *A Monte Carlo scheme based on mid-density in a hysteresis loop to determine equilibrium phase transition.* Molecular Simulation, 2011. **37**(11): p. 932-939.
165. Fomkin, A.A., N.I. Regent, and V.A. Sinitsyn, *Adsorption deformation in the microporous carbon adsorbent-benzene system and porous structure of adsorbents.* Russian Chemical Bulletin, 2000. **49**(6): p. 1012-1016.

166. Pulin, A.L., et al., *Adsorption and adsorption-induced deformation of NaX zeolite under high pressures of carbon dioxide.* Russian Chemical Bulletin, 2001. **50**(1): p. 60-62.
167. Yakovlev, V.Y., et al., *Adsorption-stimulated deformation of microporous carbon adsorbent.* Russian Chemical Bulletin, 2003. **52**(2): p. 354-358.
168. Yakovlev, V.Y., A.A. Fomkin, and A.V. Tvardovski, *Adsorption and deformation phenomena at the interaction of CO2 and a microporous carbon adsorbent.* Journal of Colloid and Interface Science, 2003. **268**(1): p. 33-36.
169. Yakovlev, V.Y., A.A. Fomkin, and A.V. Tvardovski, *Adsorption and deformation phenomena at interaction of N2 and microporous carbon adsorbent.* Journal of Colloid and Interface Science, 2004. **280**(2): p. 305-308.
170. Fomkin, A.A., *Adsorption of gases, vapors and liquids by microporous adsorbents.* Adsorption, 2005. **11**(3): p. 425-436.
171. Shkolin, A.V. and A.A. Fomkin, *Deformation of AUK microporous carbon adsorbent induced by methane adsorption.* Colloid Journal, 2009. **71**(1): p. 119-124.
172. Mushrif, S.H. and A.D. Rey, *An integrated model for adsorption-induced strain in microporous solids.* Chemical Engineering Science, 2009. **64**(22): p. 4744-4753.
173. Zalivin, S.N., et al., *Calculation of the adsorption deformation of a microporous adsorbent.* Journal of Engineering Physics and Thermophysics, 2009. **82**(3): p. 533-536.
174. Shkolin, A.V., A.A. Fomkin, and V.A. Sinitsyn, *Adsorption-induced deformation of AUK microporous carbon adsorbent in adsorption of n-pentane.* Protection of Metals and Physical Chemistry of Surfaces, 2011. **47**(5): p. 555-561.
175. Shkolin, A.V., et al., *A technique for measuring an adsorption-induced deformation.* Instruments and Experimental Techniques, 2011. **51**(1): p. 150-155.
176. Nabiulin, V.V., A.A. Fomkin, and A.V. Tvardovskiy, *Adsorption deformation of a microporous AR-V carbon adsorbent during the adsorption of n-hexane.* Russian Journal of Physical Chemistry A, 2011. **85**(11): p. 1960-1964.
177. Nabiulin, V.V., A.A. Fomkin, and A.V. Tvardovskii, *Adsorption deformation of a microporous AR-V carbon adsorbent during the adsorption of benzene.* Protection of Metals and Physical Chemistry of Surfaces, 2012. **48**(4): p. 398-401.
178. Shkolin, A.V. and A.A. Fomkin, *Adsorption deformation of AUK microporous carbon adsorbent at adsorption of n-heptane.* Protection of Metals and Physical Chemistry of Surfaces, 2013. **49**(4): p. 373-378.
179. Potapov, S.V., A.V. Shkolin, and A.A. Fomkin, *Deformation of AUK microporous carbon adsorbent induced by krypton adsorption.* Colloid Journal, 2014. **76**(3): p. 351-357.
180. Shkolin, A.V., S.V. Potapov, and A.A. Fomkin, *Deformation of AUK microporous carbon adsorbent induced by xenon adsorption.* Colloid Journal, 2015. **77**(6): p. 812-820.
181. Shkolin, A.V. and A.A. Fomkin, *Description of Adsorption-Stimulated Deformation of Microporous Adsorbents Based on Generalized Potential of Intermolecular Interactions (6, n).* Protection of Metals and Physical Chemistry of Surfaces, 2016. **52**(2): p. 193-198.

182. Dacey, J.R. and M.J.B. Evans, *Volume changes in saran charcoal caused by the adsorption of water, methanol and benzene vapours.* Carbon, 1971. **9**(5): p. 579-585.
183. Suzuki, T. and K. Kaneko, *Structural change of activated carbon fibers with desorption by in situ X-ray diffraction.* Carbon, 1988. **26**(5): p. 743-745.
184. Kaneko, K., Y. Fujiwara, and K. Nishikawa, *The micropore swelling of activated carbon fibers with water adsorption studied by use of in situ small angle x-ray scattering.* Journal of Colloid and Interface Science, 1989. **127**(1): p. 298-299.
185. Balzer, C., et al., *Deformation of Porous Carbons upon Adsorption.* Langmuir, 2011. **27**(6): p. 2553-2560.
186. Balzer, C., et al., *Deformation of microporous carbon during adsorption of nitrogen, argon, carbon dioxide, and water studied by in situ dilatometry.* Langmuir, 2015. **31**(45): p. 12512-12519.
187. Meehan, F.T., *The expansion of charcoal on sorption of carbon dioxide.* Proceedings of the Royal Society of London A: Mathematical, Physical and Engineering Sciences, 1927. **115**(770): p. 199-207.
188. Bangham, D.H. and N. Fakhoury, *The swelling of charcoal. Part I. Preliminary experiments with water vapour, carbon dioxide, ammonia, and sulphur dioxide.* Proceedings of the Royal Society of London A: Mathematical, Physical and Engineering Sciences, 1930. **130**(812): p. 81-89.
189. Bangham, D.H., N. Fakhoury, and A.F. Mohamed, *The swelling of charcoal. Part II. Some factors controlling the expansion caused by water, benzene and pyridine vapours.* Proceedings of the Royal Society of London A: Mathematical, Physical and Engineering Sciences, 1932. **138**(834): p. 162-183.
190. Bangham, D.H., N. Fakhoury, and A.F. Mohamed, *The swelling of charcoal. Part III. Experiments with the lower alcohols.* Proceedings of the Royal Society of London A: Mathematical, Physical and Engineering Sciences, 1934. **147**(860): p. 152-175.
191. Bangham, D.H., *The swelling of charcoal. Part IV. Stoichiometric relations for the films of the alcohols.* Proceedings of the Royal Society of London A: Mathematical, Physical and Engineering Sciences, 1934. **147**(860): p. 175-188.
192. Bangham, D.H. and R.I. Razouk, *The swelling of charcoal. Part V. The saturation and immersion expansions and the heat of wetting.* Proceedings of the Royal Society of London A: Mathematical, Physical and Engineering Sciences, 1938. **166**(927): p. 572-586.
193. Haines, R.S. and R. McIntosh, *Length changes of activated carbon rods caused by adsorption of vapors.* The Journal of Chemical Physics, 1947. **15**(1): p. 28-38.
194. Lakhanpal, M.L. and E.A. Flood, *Stresses and strains in adsorbate–adsorbent systems: IV. contractions of activated carbon on adsorption of gases and vapors at low initial pressures.* Canadian Journal of Chemistry, 1957. **35**(8): p. 887-899.
195. Flood, E.A. and F.M. Farhan, *Stresses and strains in adsorbent–adsorbate systems: V. thermodynamic theory of adsorption-extension phenomena.* Canadian Journal of Chemistry, 1963. **41**(7): p. 1703-1717.
196. Farhan, F.M., et al., *Stresses and strains in adsorbent–adsorbate systems. VI.* Canadian Journal of Chemistry, 1967. **45**(6): p. 589-593.

197. Scherer, G.W., *Dilatation of porous glass.* Journal of the American Ceramic Society, 1986. **69**(6): p. 473-480.
198. Smith, D.M., G.W. Scherer, and J.M. Anderson, *Shrinkage during drying of silica gel.* Journal of Non-Crystalline Solids, 1995. **188**(3): p. 191-206.
199. Dolino, G., D. Bellet, and C. Faivre, *Adsorption strains in porous silicon.* Physical Review B, 1996. **54**(24): p. 17919-17929.
200. Grosman, A. and C. Ortega, *Influence of elastic strains on the adsorption process in porous materials: an experimental approach.* Langmuir, 2009. **25**(14): p. 8083-8093.
201. Grosman, A. and C. Ortega, *Influence of elastic strains on the adsorption process in porous materials. Thermodynamics and experiment.* Applied Surface Science, 2010. **256**(17): p. 5210-5215.
202. Amberg, C.H. and R. McIntosh, *A study of adsorption hysteresis by means of length changes of a rod of porous glass.* Canadian Journal of Chemistry, 1952. **30**(12): p. 1012-1032.
203. Eriksson, J.C., *Thermodynamics of surface phase systems.* Surface Science, 1969. **14**(1): p. 221-246.
204. Ash, S.G., D.H. Everett, and C. Radke, *Thermodynamics of the effects of adsorption on interparticle forces.* Journal of the Chemical Society, Faraday Transactions 2: Molecular and Chemical Physics, 1973. **69**: p. 1256-1277.
205. Ravikovitch, P.I. and A.V. Neimark, *Density functional theory model of adsorption deformation.* Langmuir, 2006. **22**(26): p. 10864-10868.
206. Kowalczyk, P., A. Ciach, and A.V. Neimark, *Adsorption-induced deformation of microporous carbons: pore size distribution effect.* Langmuir, 2008. **24**(13): p. 6603-6608.
207. Gor, G.Y. and A.V. Neimark, *Adsorption-induced deformation of mesoporous solids.* Langmuir, 2010. **26**(16): p. 13021-13027.
208. Gor, G.Y. and A.V. Neimark, *Adsorption-induced deformation of mesoporous solids: macroscopic approach and density functional theory.* Langmuir, 2011. **27**(11): p. 6926-6931.
209. Gor, G.Y., et al., *Adsorption of n-Pentane on Mesoporous Silica and Adsorbent Deformation.* Langmuir, 2013. **29**(27): p. 8601-8608.
210. Balzer, C., et al., *Deformation of Microporous Carbons during N2, Ar, and CO2 Adsorption: Insight from the Density Functional Theory.* Langmuir, 2016. **32**(32): p. 8265-8274.
211. Gor, G.Y. and N. Bernstein, *Revisiting Bangham's law of adsorption-induced deformation: changes of surface energy and surface stress.* Physical Chemistry Chemical Physics, 2016. **18**(14): p. 9788-9798.
212. Grosman, A. and C. Ortega, *Influence of elastic deformation of porous materials in adsorption-desorption process: A thermodynamic approach.* Physical Review B: Condensed Matter and Materials Physics, 2008. **78**(8): p. 085433/1-085433/12.
213. Günther, G., et al., *Novel insights into nanopore deformation caused by capillary condensation.* Physical Review Letters, 2008. **101**(8): p. 086104/1-086104/4.
214. Gunther, G. and M. Schoen, *Sorption strain as a packing phenomenon.* Physical Chemistry Chemical Physics, 2009. **11**(40): p. 9082-9092.
215. Günther, G. and M. Schoen, *Sorption strains and their consequences for capillary condensation in nanoconfinement.* Molecular Simulation, 2009. **35**(1-2): p. 138-150.

216. Yang, K., et al., *Deformation of coal induced by methane adsorption at geological conditions.* Energy & Fuels, 2010. **24**(11): p. 5955-5964.
217. Yang, K., et al., *Effects of CO2 adsorption on coal deformation during geological sequestration.* Journal of Geophysical Research: Solid Earth, 2011. **116**(B8): p. 1-11.
218. Do, D.D., D. Nicholson, and H.D. Do, *Effects of adsorbent deformation on the adsorption of gases in slitlike graphitic pores: a computer simulation study.* J. Phys. Chem. C, 2008. **112**: p. 14075-14089.
219. Nguyen, V.T., D.D. Do, and D. Nicholson, *Solid deformation induced by the adsorption of methane and methanol under sub- and supercritical conditions.* Journal of Colloid and Interface Science, 2012. **388**(1): p. 209-218.
220. Metropolis, N. and S. Ulam, *The Monte Carlo method.* Journal of the American Statistical Association, 1949. **44**(247): p. 335-341.
221. Metropolis, N., et al., *Equation of state calculations by fast computing machines.* The Journal of Chemical Physics, 1953. **21**(6): p. 1087-1092.
222. Ustinov, E.A. and D.D. Do, *Application of kinetic Monte Carlo method to equilibrium systems: Vapour–liquid equilibria.* Journal of Colloid and Interface Science, 2012. **366**(1): p. 216-223.
223. Norman, G.E. and Filinov, *Investigation of phase transitions by a Monte Carlo method.* High Temp., 1969. **7**: p. 216-222.
224. Steele, W.A., *The physical interaction of gases with crystalline solids: I. Gas-solid energies and properties of isolated adsorbed atoms.* Surface Science, 1973. **36**(1): p. 317-352.
225. Bojan, M.J. and W.A. Steele, *Computer simulation of physisorption on a heterogeneous surface.* Surface Science, 1988. **199**(3): p. L395-L402.
226. Bojan, M.J. and W.A. Steele, *Computer simulation of physisorbed Kr on a heterogeneous surface.* Langmuir, 1989. **5**: p. 625-633.
227. Bojan, M.J. and W.A. Steele, *Computer simulation of physical adsorption on stepped surfaces.* Langmuir, 1993. **9**(10): p. 2569-2575.
228. Bojan, M.J. and W.A. Steele, *Computer simulations of the adsorption of xenon on stepped surfaces.* Molecular Physics, 1998. **95**(3): p. 431-437.
229. Widom, B., *Some topics in the theory of fluids.* Journal of Chemical Physics, 1963. **39**(11): p. 2808-2812.
230. Widom, B., *Potential-distribution theory and the statistical mechanics of fluids.* The Journal of Physical Chemistry, 1982. **86**(6): p. 869-872.
231. Johnson, J.K., J.A. Zollweg, and K.E. Gubbins, *The Lennard-Jones equation of state revisited.* Molecular Physics, 1993. **78**(3): p. 591-618.
232. Do, D.D. and H.D. Do, *Appropriate volumes for adsorption isotherm studies: The absolute void volume, accessible pore volume and enclosing particle volume* Journal of Colloid and Interface Science, 2007. **316**(2): p. 317-330.
233. Do, D.D., H.D. Do, and D. Nicholson, *Molecular Simulation of Excess Isotherm and Excess Enthalpy Change in Gas-Phase Adsorption.* The Journal of Physical Chemistry B, 2009. **113**(4): p. 1030-1040.
234. Beebe, R.A., J.B. Beckwith, and J.M. Honig, *The Determination of Small Surface Areas by Krypton Adsorption at Low Temperatures.* Journal of the American Chemical Society, 1945. **67**(9): p. 1554-1558.
235. Larher, Y., *Triple point of first monomolecular layer of krypton adsorbed on the cleavage face of graphite.* Journal of the Chemical Society-Faraday Transactions I, 1974. **70**(2): p. 320-329.

236. Larher, Y. and A. Terlain, *Transition from fluid to registered solid of the krypton monolayer adsorbed on the basal face of graphite.* The Journal of Chemical Physics, 1980. **72**(2): p. 1052-1054.
237. Stephens, P.W., et al., *X-Ray Scattering Study of the Commensurate-Incommensurate Transition of Monolayer Krypton on Graphite.* Physical Review Letters, 1979. **43**(1): p. 47-51.
238. Butler, D.M., et al., *Heat Capacity of Krypton Physisorbed on Graphite.* Physical Review Letters, 1979. **42**(19): p. 1289-1292.
239. Butler, D.M., J.A. Litzinger, and G.A. Stewart, *Completion of the Phase Diagram for the Monolayer Regime of the Krypton-Graphite Adsorption System.* Physical Review Letters, 1980. **44**(7): p. 466-468.
240. Clark, H., *Vertical Discontinuities in the Adsorption Isotherm of Krypton on Graphitized Carbon Black.* The Journal of Physical Chemistry, 1955. **59**(10): p. 1068-1069.
241. Nguyen, V.T., D.D. Do, and D. Nicholson, *On the heat of adsorption at layering transitions in adsorption of noble gases and nitrogen on graphite.* J. Phys. Chem. C, 2010. **114**(50): p. 22171-22180.
242. Wang, Y., et al., *A computer simulation and experimental study of the difference between krypton adsorption on a graphite surface and in a graphitic hexagonal pore.* Carbon, 2012. **50**(8): p. 2908-2917.
243. Birkett, G.R. and D.D. Do, *Aspects of physical adsorption on carbon black from molecular simulation*, in *Carbon Materials - Theory and Practice. Research Signpost*, A.P. Terzyk, P.A. Gauden, and P. Kowalczyk, Editors. 2008: Kerala, India. p. 351-422.
244. Houlrik, J.M., D.P. Landau, and S.J.K. Jensen, *Krypton clusters adsorbed on graphite: A low-temperature commensurate-incommensurate transition.* Physical Review E, 1994. **50**(3): p. 2007-2013.
245. Charles., K., *Introduction to solid state physics*. 8th ed. ed. 2005: Hoboken, N.J. : J. Wiley
246. Vishnyakov, A. and A.V. Neimark, *Studies of liquid-vapor equilibria, criticality, and spinodal transitions in nanopores by the gauge cell Monte Carlo simulation method.* Journal of Physical Chemistry B, 2001. **105**(29): p. 7009-7020.
247. Fan, C., D.D. Do, and D. Nicholson, *A new and effective Bin–Monte Carlo scheme to study vapour–liquid equilibria and vapour–solid equilibria.* Fluid Phase Equilibria, 2012. **325**: p. 53-65.
248. Wang, Y., D.D. Do, and D. Nicholson, *Study of heat of adsorption across the capillary condensation in cylindrical pores.* Colloids Surf., A, 2011. **380**: p. 66-78.
249. Heffelfinger, G.S., F. van Swol, and K.E. Gubbins, *Liquid-vapour coexistence in a cylindrical pore.* Molecular Physics, 1987. **61**(6): p. 1381-1390.
250. Peterson, B.K. and K.E. Gubbins, *Phase transitions in a cylindrical pore -- Grand canonical Monte Carlo, mean field theory and the Kelvin equation.* Molecular Physics, 1987. **62**(1): p. 215-226.
251. Diao, R., et al., *Monte Carlo Simulation of Adsorption-Induced Deformation in Finite Graphitic Slit Pores.* The Journal of Physical Chemistry C, 2016. **120**(51): p. 29272-29282.

252. Zeng, Y., et al., *Condensation and Evaporation in Slit-Shaped Pores: Effects of Adsorbate Layer Structure and Temperature.* The Journal of Physical Chemistry C, 2014. **118**(6): p. 3172-3180.

Appendices

Appendix 1

We plot in Figure A1b the instant number of particles as a function of number of cycles for points A-F, C' and D' as marked on the isotherm of krypton at 77 K shown in Figure A1a. The system reaches equilibrium quickly in the equilibrium stage, and no indication of any deviation from the ensemble averages in the sampling stage during the 2D-condensation of the first and third layers from A to B, E to F, respectively, and for points C and C', D and D' which are at the same pressure in the adsorption and desorption branches, respectively. This suggests that the run lengths are sufficient to reach stable convergence for both adsorption and desorption branches, supporting the observed hysteresis in our study.

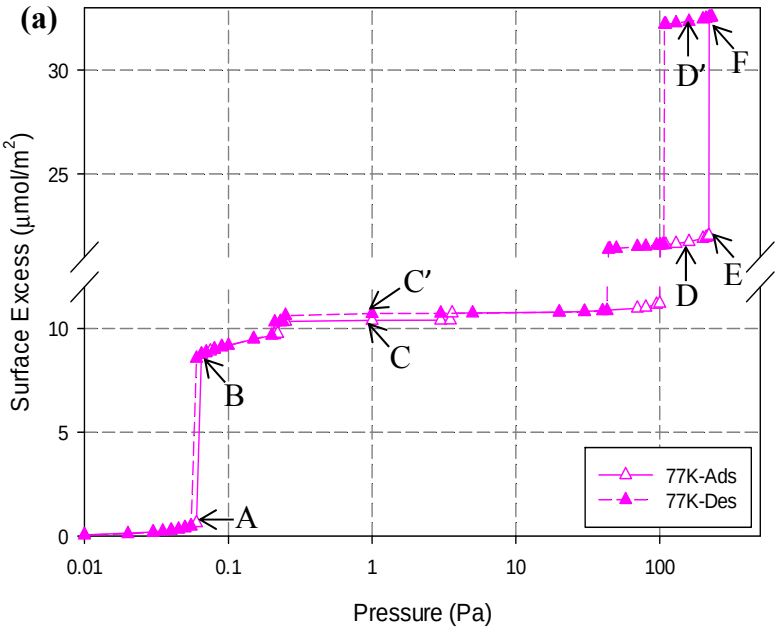

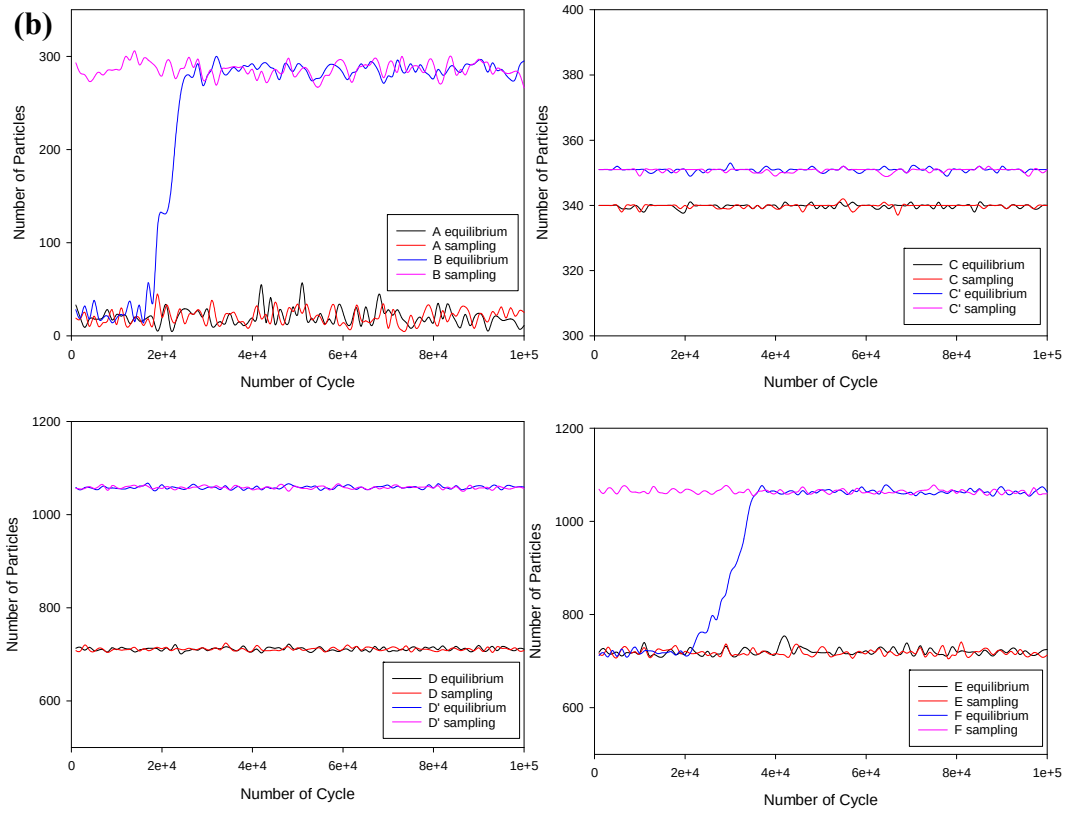

Figure A1. (a) *GCMC* adsorption isotherm for Kr on a graphite surface at 77 K; (b) Control charts in the equilibrium and sampling stages for points A-F, C', D' as marked in Figure A1a; A and B, E and F correspond to the *2D*-condensation of the first and third layer, respectively; C and C', D and D' are at the same pressure in the adsorption and desorption branches, respectively.

Appendix 2

Figure A2 shows the adsorption isotherms of argon in finite length pores with pore widths from 1.9 to 2.5 nm. Five, six and seven adsorbate layers can be formed in 1.9-2.1 nm, 2.2-2.4 nm and 2.5 nm pores, respectively. In pores with widths of 1.9 nm, 2.0 nm, 2.2 nm, 2.3 nm and 2.5 nm, where the packing is commensurate, there is a fused hysteresis loop, but in the pores with widths of 2.1 nm and 2.4 nm there is only a capillary condensation/evaporation loop.

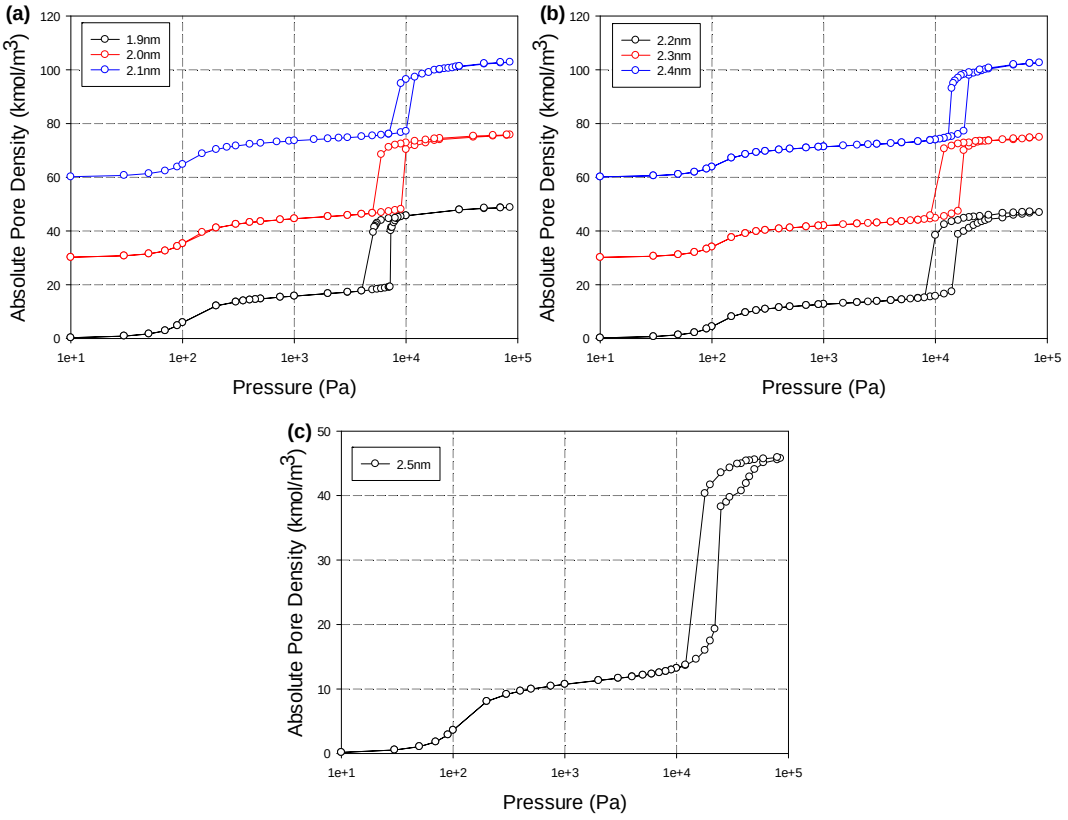

Figure A2. The adsorption isotherms of argon in finite length pores as a function of pore width; the pore lengths are 20 nm and the temperature is 87 K; (a) 1.9-2.1 nm; (b) 2.2-2.4 nm; (c) 2.5 nm. Isotherms for 2.0, 2.1, 2.3, 2.4 nm are shifted up by 30, 60, 30, 60 kmol/m^3, respectively.

Figure A3 shows the effects of pore length (10 nm, 20 nm and 30 nm) for argon adsorption in finite length pores of 1.5 nm width. The features of the isotherm and the hysteresis do not change with pore length.

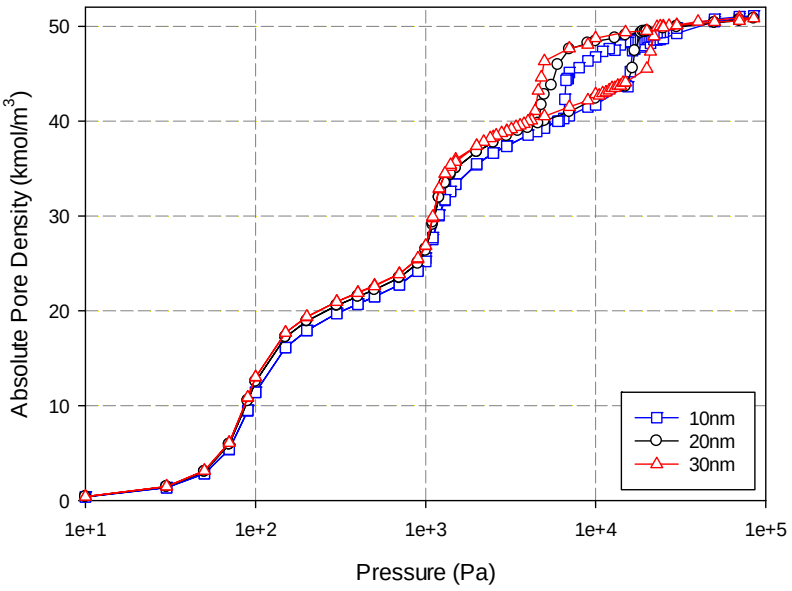

Figure A3. The adsorption isotherms of argon at 87 K in finite length pores of width 1.5 nm as a function of pore length.

Appendix 3

To prove that the distance between the 1st adsorbate layer and the 1st movable layer ΔZ_1 increases slightly in the sub-monolayer region of argon adsorption on a deformable finite graphite surface at 87 K, we show in Figure A4 the isosteric heat as a function of the bulk pressure. It can be seen that the solid-fluid isosteric heat decreases during the formation of the 1st adsorbed layer, which indicates that the adsorbed molecules in the 1st layer are a little further away from the graphite surface with the increase of pressure.

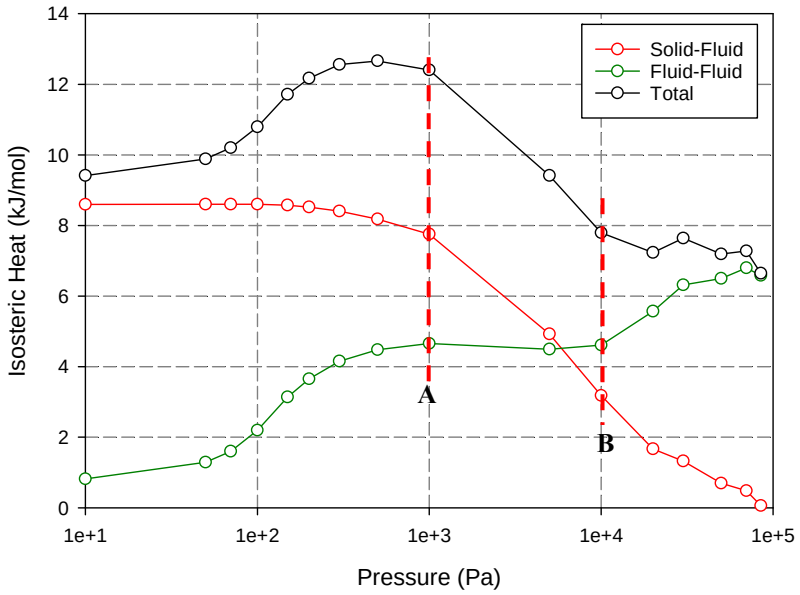

Figure A4. The isosteric heat as a function of the bulk pressure for argon adsorption on a deformable finite graphite surface at 87 K.

We further conducted simulations for argon adsorption at 87 K on a rigid finite graphite surface having the same structures as the deformable graphite surface with the interlayer spacing between graphene layers of 0.3354 nm. Figure A5a shows the distances between the 1st adsorbate layer and the 1st graphene layer (ΔZ_1), the 2nd graphene layer (ΔZ_2), and the outermost layer (ΔZ_3) as a function of the bulk pressure. Interestingly, ΔZ_1 increases slightly in the sub-monolayer region and we could also see this phenomenon at temperatures as low as 40 K, as shown in Figure A5b, which indicates that the increase of ΔZ_1 in the sub-monolayer region is not a result from the deformation of the graphite surface. Correspondingly, the solid-fluid isosteric heat decreases in the sub-monolayer region with the results at 40 K shown in Figure A5c.

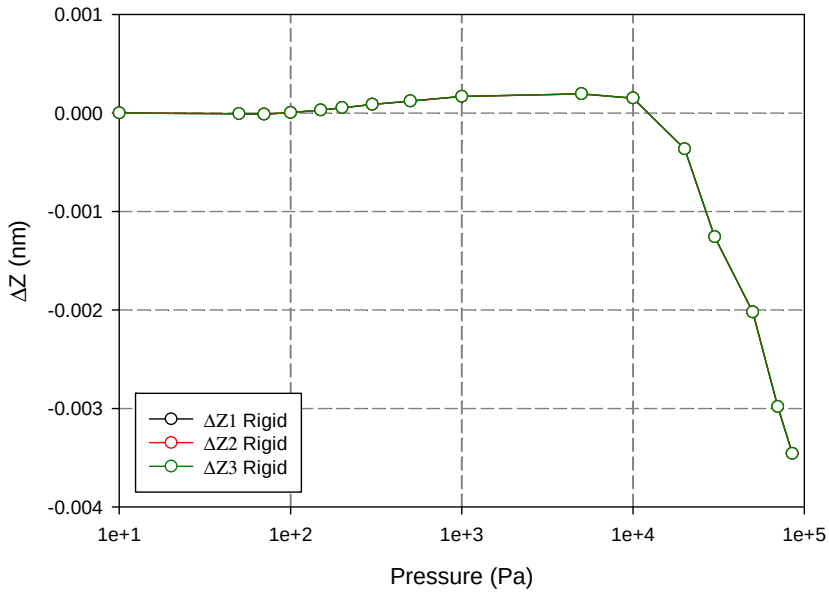
0.001
0.000
-0.001
-0.002
-0.003
-0.004
ΔZ (nm)
ΔZ1 Rigid
ΔZ2 Rigid
ΔZ3 Rigid
1e+1
1e+2
1e+3
1e+4
1e+5
Pressure (Pa)

(a)

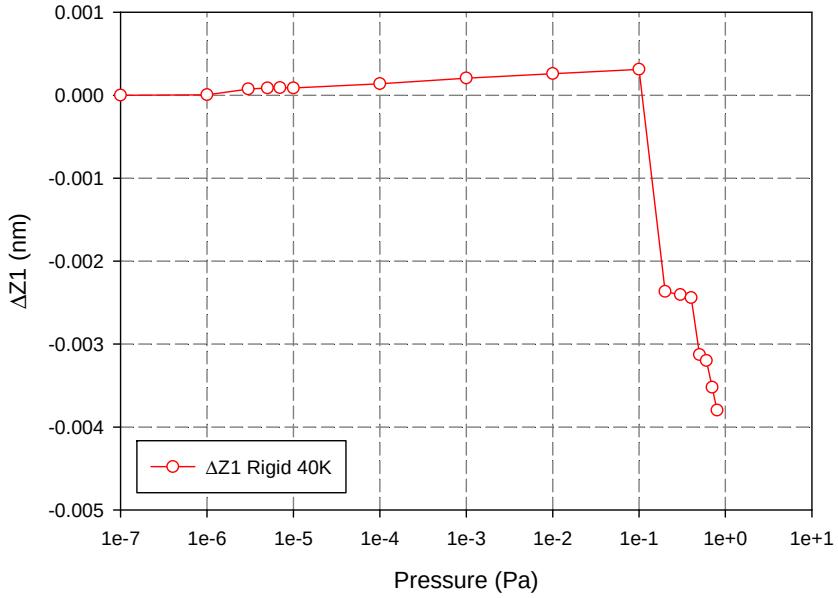
0.001
0.000
-0.001
-0.002
-0.003
-0.004
-0.005
ΔZ1 (nm)
ΔZ1 Rigid 40K
1e-7
1e-6
1e-5
1e-4
1e-3
1e-2
1e-1
1e+0
1e+1
Pressure (Pa)

(b)

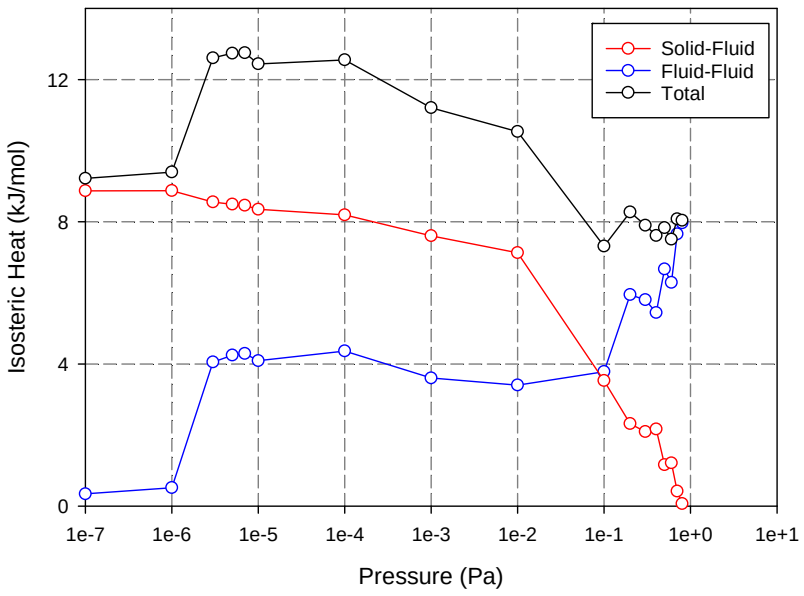

(c)

Figure A5. (a) The distances between the 1st adsorbate layer and the 1st graphene layer (ΔZ_1), the 2nd graphene layer (ΔZ_2), and the outermost layer (ΔZ_3) as a function of the bulk pressure for argon adsorption on a rigid finite graphite surface at 87 K; (b) ΔZ_1 as a function of the bulk pressure for argon adsorption on a rigid finite graphite surface at 40 K and (c) the corresponding isosteric heat with bulk pressure.

To test if the increase of ΔZ_1 in the sub-monolayer region is induced by the finite surface, simulations for argon adsorption at 40 and 77 K (87 K not available now, if needed, the results could be added later) on a rigid infinite graphite surface were conducted and the results of ΔZ_1 as a function of the bulk pressure are shown in Figures A6a and b. At 40 K, ΔZ_1 stays constant during the formation of the 1st layer and begins to decrease at the formation of the 2nd layer. However, ΔZ_1 increases slightly in the sub-monolayer region when the temperature is increased to 77 K, which may be caused by the greater thermal motion of the adsorbed molecules at higher temperatures. The difference between the results of the finite and the infinite surfaces at 40 K may indicate the increase of ΔZ_1 in the sub-monolayer region in the first case is induced by the finite surface. The solid-fluid isosteric heat as a function of the bulk pressure at 40 and 77 K, as shown in Figures A6c and d, respectively, could lend support to the variation of ΔZ_1.

The variation of ΔZ_1 in the sub-monolayer region in the case of argon adsorption at 40 and 77 K on a deformable infinite graphite surface is similar to the corresponding situation on a rigid infinite surface.

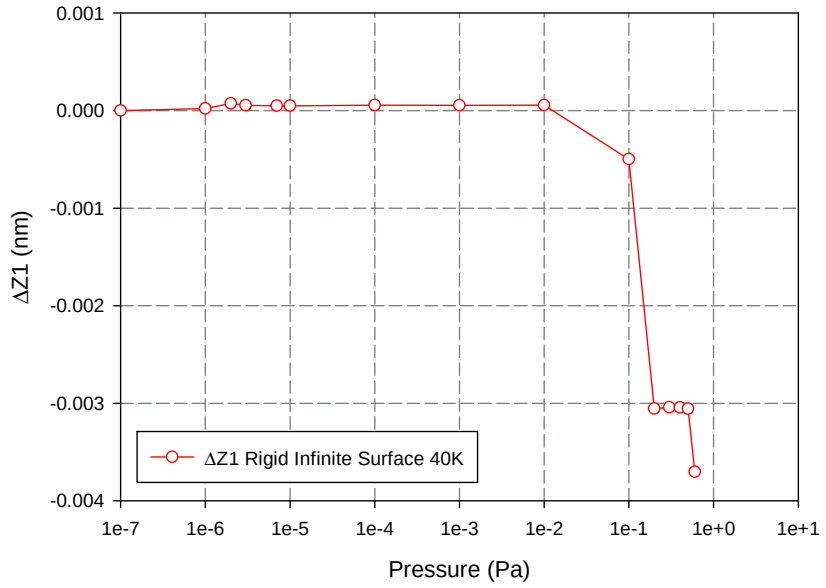

(a)

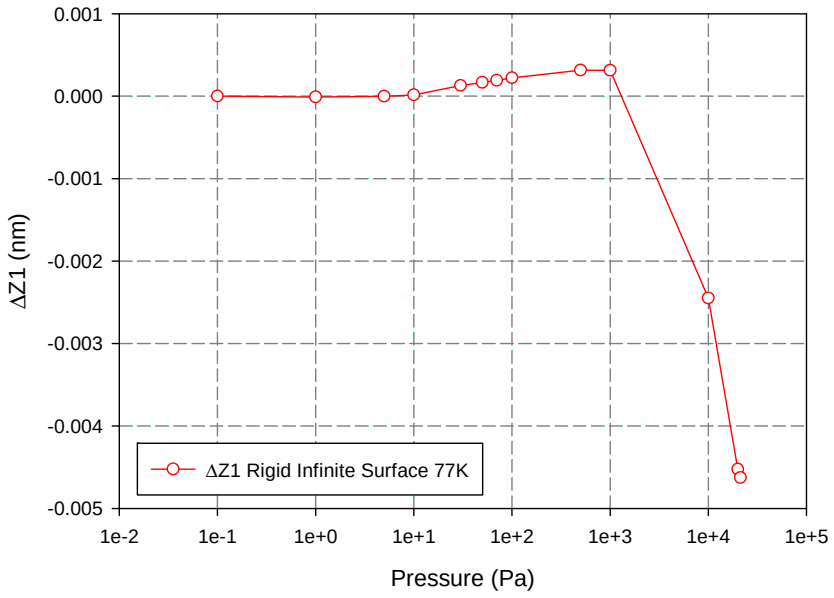

(b)

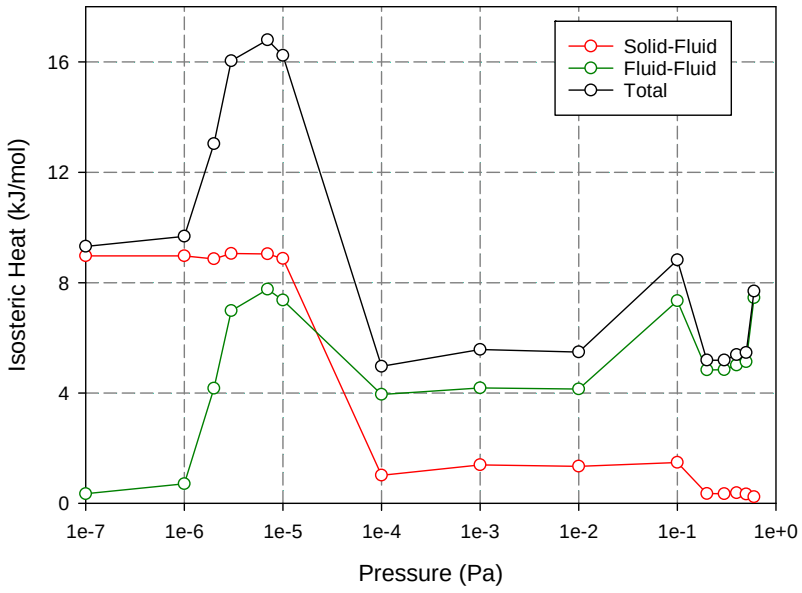

(c)

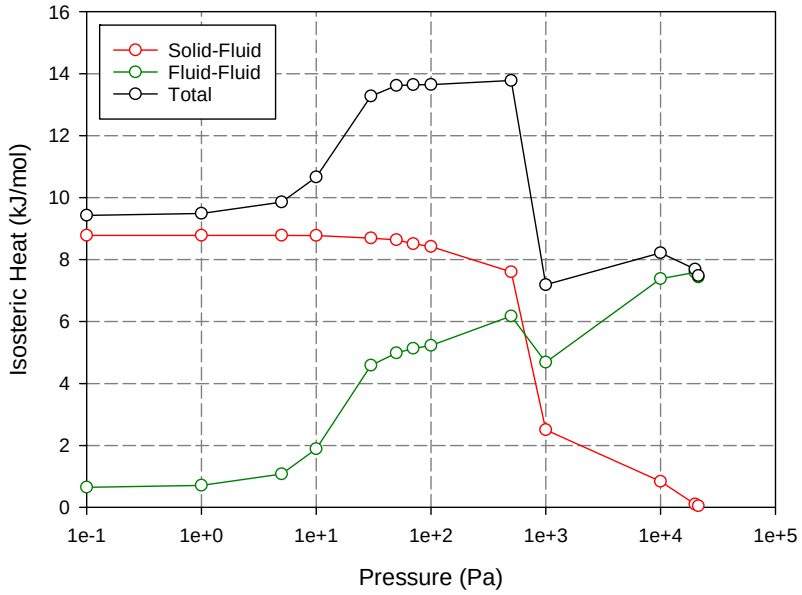

(d)

Figure A6. (a) The distances between the 1st adsorbate layer and the 1st graphene layer (ΔZ_1), the 2nd graphene layer (ΔZ_2), and the outermost layer (ΔZ_3) as a function of the bulk pressure for argon adsorption on a rigid infinite graphite surface at (a) 40 K and (b) 77 K and the corresponding isosteric heat with bulk pressure at (c) 40 K and (d) 77 K.

Appendix 4

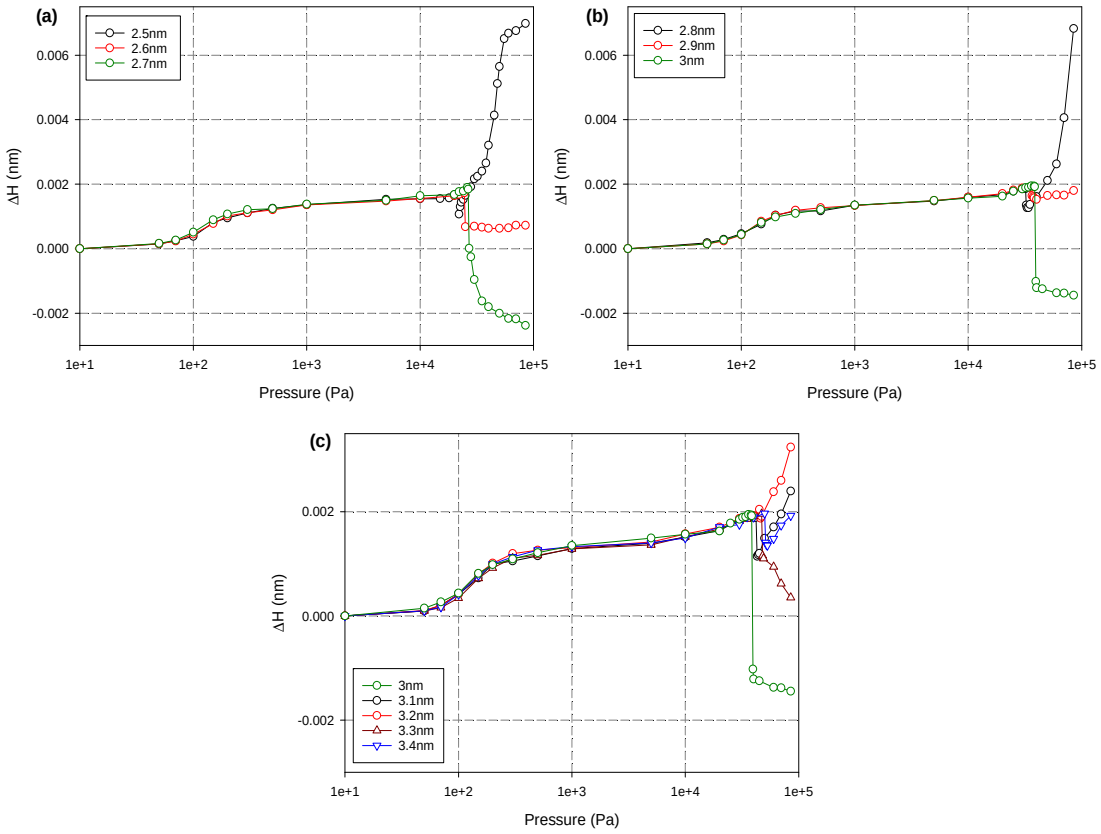

Figure A7. The strain isotherm in semi-logarithmic scale for argon adsorption at 87 K in pores of different initial widths, (a) 2.5-2.7 nm, (b) 2.8-3 nm, (c) 3-3.4 nm; the pore length is 20 nm with four movable layers and two fixed outermost layers.

Appendix 5: Permission of Reproduction from the Copyright Owner

ELSEVIER LICENSE
TERMS AND CONDITIONS

Apr 07, 2017

This Agreement between RUI DIAO ("You") and Elsevier ("Elsevier") consists of your license details and the terms and conditions provided by Elsevier and Copyright Clearance Center.

License Number	4083461095513
License date	
Licensed Content Publisher	Elsevier
Licensed Content Publication	Journal of Colloid and Interface Science
Licensed Content Title	On the 2D-transition, hysteresis and thermodynamic equilibrium of Kr adsorption on a graphite surface
Licensed Content Author	Rui Diao,Chunyan Fan,D.D. Do,D. Nicholson
Licensed Content Date	15 December 2015
Licensed Content Volume	460
Licensed Content Issue	n/a
Licensed Content Pages	9
Start Page	281
End Page	289
Type of Use	reuse in a thesis/dissertation
Portion	full article
Format	both print and electronic
Are you the author of this Elsevier article?	Yes
Will you be translating?	No
Order reference number	
Title of your thesis/dissertation	Fundamental Study of Simple Gas Adsorption and Adsorption-Induced Deformation in Carbonaceous Materials
Expected completion date	Dec 2017
Estimated size (number of pages)	145
Elsevier VAT number	GB 494 6272 12

ELSEVIER LICENSE
TERMS AND CONDITIONS

Apr 07, 2017

This Agreement between RUI DIAO ("You") and Elsevier ("Elsevier") consists of your license details and the terms and conditions provided by Elsevier and Copyright Clearance Center.

License Number	4083490379069
License date	
Licensed Content Publisher	Elsevier
Licensed Content Publication	Chemical Engineering Journal
Licensed Content Title	On the adsorbate restructuring induced hysteresis of simple gas adsorption in slit micropores
Licensed Content Author	Rui Diao,Chunyan Fan,D.D. Do,D. Nicholson
Licensed Content Date	15 April 2016
Licensed Content Volume	290
Licensed Content Issue	n/a
Licensed Content Pages	10
Start Page	381
End Page	390
Type of Use	reuse in a thesis/dissertation
Intended publisher of new work	other
Portion	full article
Format	both print and electronic
Are you the author of this Elsevier article?	Yes
Will you be translating?	No
Order reference number	
Title of your thesis/dissertation	Fundamental Study of Simple Gas Adsorption and Adsorption-Induced Deformation in Carbonaceous Materials
Expected completion date	Dec 2017
Estimated size (number of pages)	145
Elsevier VAT number	GB 494 6272 12

Copyright Clearance Center RightsLink®

Home | Account Info | Help

ACS Publications
Most Trusted. Most Cited. Most Read.

Logged in as:
RUI DIAO
LOGOUT

Title:	Monte Carlo Simulation of Adsorption-Induced Deformation in Finite Graphitic Slit Pores
Author:	Rui Diao, Chunyan Fan, D. D. Do, et al
Publication:	The Journal of Physical Chemistry C
Publisher:	American Chemical Society
Date:	Dec 1, 2016

Copyright © 2016, American Chemical Society

PERMISSION/LICENSE IS GRANTED FOR YOUR ORDER AT NO CHARGE

This type of permission/license, instead of the standard Terms & Conditions, is sent to you because no fee is being charged for your order. Please note the following:

- Permission is granted for your request in both print and electronic formats, and translations.
- If figures and/or tables were requested, they may be adapted or used in part.
- Please print this page for your records and send a copy of it to your publisher/graduate school.
- Appropriate credit for the requested material should be given as follows: "Reprinted (adapted) with permission from (COMPLETE REFERENCE CITATION). Copyright (YEAR) American Chemical Society." Insert appropriate information in place of the capitalized words.
- One-time permission is granted only for the use specified in your request. No additional uses are granted (such as derivative works or other editions). For any other uses, please submit a new request.

BACK | CLOSE WINDOW

ELSEVIER LICENSE
TERMS AND CONDITIONS

Aug 14, 2017

This Agreement between Ms. Rui Diao ("You") and Elsevier ("Elsevier") consists of your license details and the terms and conditions provided by Elsevier and Copyright Clearance Center.

License Number	4167460059581
License date	Aug 14, 2017
Licensed Content Publisher	Elsevier
Licensed Content Publication	Chemical Engineering Journal
Licensed Content Title	Adsorption induced deformation in graphitic slit mesopores: A Monte Carlo simulation study
Licensed Content Author	Rui Diao,Chunyan Fan,D.D. Do,D. Nicholson
Licensed Content Date	Nov 15, 2017
Licensed Content Volume	328
Licensed Content Issue	n/a
Licensed Content Pages	13
Start Page	280
End Page	292
Type of Use	reuse in a thesis/dissertation
Intended publisher of new work	other
Portion	full article
Format	both print and electronic
Are you the author of this Elsevier article?	Yes
Will you be translating?	No